

1996

Computational investigation of the low speed S1223 airfoil with and without a gurney flap

Edward Tejnil
San Jose State University

Follow this and additional works at: https://scholarworks.sjsu.edu/etd_theses

Recommended Citation

Tejnil, Edward, "Computational investigation of the low speed S1223 airfoil with and without a gurney flap" (1996). *Master's Theses*. 1406.

DOI: <https://doi.org/10.31979/etd.s9e5-eug4>

https://scholarworks.sjsu.edu/etd_theses/1406

This Thesis is brought to you for free and open access by the Master's Theses and Graduate Research at SJSU ScholarWorks. It has been accepted for inclusion in Master's Theses by an authorized administrator of SJSU ScholarWorks. For more information, please contact scholarworks@sjsu.edu.

INFORMATION TO USERS

This manuscript has been reproduced from the microfilm master. UMI films the text directly from the original or copy submitted. Thus, some thesis and dissertation copies are in typewriter face, while others may be from any type of computer printer.

The quality of this reproduction is dependent upon the quality of the copy submitted. Broken or indistinct print, colored or poor quality illustrations and photographs, print bleedthrough, substandard margins, and improper alignment can adversely affect reproduction.

In the unlikely event that the author did not send UMI a complete manuscript and there are missing pages, these will be noted. Also, if unauthorized copyright material had to be removed, a note will indicate the deletion.

Oversize materials (e.g., maps, drawings, charts) are reproduced by sectioning the original, beginning at the upper left-hand corner and continuing from left to right in equal sections with small overlaps. Each original is also photographed in one exposure and is included in reduced form at the back of the book.

Photographs included in the original manuscript have been reproduced xerographically in this copy. Higher quality 6" x 9" black and white photographic prints are available for any photographs or illustrations appearing in this copy for an additional charge. Contact UMI directly to order.

UMI

**A Bell & Howell Information Company
300 North Zeeb Road, Ann Arbor MI 48106-1346 USA
313/761-4700 800/521-0600**

**COMPUTATIONAL INVESTIGATION OF THE LOW SPEED S1223
AIRFOIL WITH AND WITHOUT A GURNEY FLAP**

A Thesis

Presented to

The Faculty of the Aerospace Engineering Department

San Jose State University

In Partial Fulfillment

of the Requirements for the Degree of

Master of Science

by

Edward Tejnil

December 1996

UMI Number: 1382610

UMI Microform 1382610
Copyright 1997, by UMI Company. All rights reserved.

**This microform edition is protected against unauthorized
copying under Title 17, United States Code.**

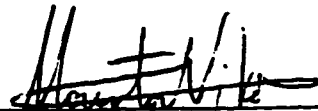
UMI
300 North Zeeb Road
Ann Arbor, MI 48103

© 1996

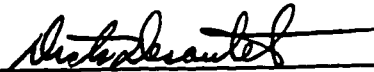
Edward Tejnil

ALL RIGHTS RESERVED

APPROVED FOR THE DEPARTMENT OF
AEROSPACE ENGINEERING



Dr. Nikos Mourtos

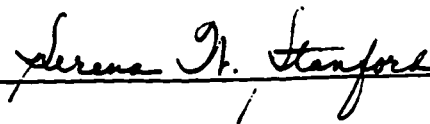


Dr. Dick Desautel



Dr. Thomas Pulliam

APPROVED FOR THE UNIVERSITY



ABSTRACT

COMPUTATIONAL INVESTIGATION OF THE LOW SPEED S1223 AIRFOIL WITH AND WITHOUT A GURNEY FLAP

by Edward Tejnil

A numerical investigation was performed to evaluate the high-lift performance of the S1223 low-speed airfoil. The effects of adding a 1% of chord Gurney flap to this airfoil was also examined. The low-speed, viscous, turbulent flow calculations were carried out by solving the incompressible Navier-Stokes equations with the INS2D code. Three turbulence models were used: a) the *Baldwin and Barth* (BB), b) the one-equation *Spalart-Allmaras* (SA) and c) the two-equation $k-\omega$ (SST) model. The solution presented includes lift, drag, moment, pressure, skin friction coefficients, sample velocity profiles and detailed flow structures with comparison made to experimental (wind-tunnel) data wherever possible. Good convergence was obtained only for the BB and SA turbulence models, with good agreement with experimental data in a limited range of angle of attack. Furthermore, the addition of the Gurney flap produced a significant lift increase with only a moderate drag penalty.

ACKNOWLEDGMENTS

The author would like to thank Dr. Stuart E. Rogers and William M. Chan of NASA Ames Research Center for their help in the use of the INS2D and grid generator HYPGEN computer codes.

TABLE OF CONTENTS

| | |
|--|------------|
| Title Page | i |
| Copyright page | ii |
| Signature page | iii |
| ABSTRACT | iv |
| Acknowledgments | v |
| TABLE OF CONTENTS | vi |
| TABLE OF FIGURES | x |
| NOMENCLATURE..... | xiv |
| 1. INTRODUCTION | 1 |
| 2. THEORETICAL BACKGROUND & METHOD OF SOLUTION OVERVIEW | 5 |
| 2.1 Governing Equations/Numerical Algorithm..... | 5 |
| 3. GOVERNING EQUATIONS AND ARTIFICIAL COMPRESSIBILITY | 8 |
| 3.1 Incompressible Navier-Stokes Equations..... | 8 |
| 3.2 Curvilinear Coordinate Transformation | 10 |
| 3.3 Artificial Compressibility/Pseudocompressible Formulation | 12 |

| | |
|---|-----------|
| 4. SOLUTION OF THE INCOMPRESSIBLE NAVIER STOKES EQUATIONS..... | 14 |
| 4.1 Upwind Differencing..... | 19 |
| 4.2 Implicit Scheme | 23 |
| 4.2.1 <i>Implicit Scheme Selection in the Flow Solver INS2D</i> | 25 |
| 4.2.2 <i>Incomplete Lower-upper Factorization (ILU)</i> | 28 |
| 4.2.3 <i>Point Relaxation (PR)</i> | 29 |
| 4.2.4 <i>Line Relaxation (LR)</i> | 30 |
| 4.2.5 <i>Generalized Minimum Residual Method (GMRES)</i> | 32 |
| 4.3 Boundary Conditions | 36 |
| 4.3.1 <i>Inflow Boundary</i> | 38 |
| 4.3.2 <i>Outflow Boundary</i> | 39 |
| 5. TURBULENCE MODELS | 41 |
| 5.1 Baldwin Barth Model (BB) | 41 |
| 5.2 Spalart-Allmaras Model (SA)..... | 43 |
| 5.3 k- ω (SST) Model..... | 45 |
| 6. GEOMETRY MODELING AND GRID GENERATION..... | 48 |
| 6.1 Geometry Modeling (Airfoil Discussion)..... | 48 |
| 6.2 Grid Generation | 52 |

| | |
|--|-----------|
| 7. THE GURNEY FLAP | 56 |
| 7.1 Concept and Description of the Gurney Flap | 56 |
| 7.2 Gurney Flap as Applied and Tested | 59 |
| 8. EXPERIMENTAL DATA & CORRECTIONS..... | 62 |
| 8.1 Experimental Data, Measurement Techniques | 62 |
| <i>8.1.1 Lift & Drag Measurements</i> | <i>65</i> |
| 8.2 Experimental Data Corrections, Data Reduction | 67 |
| <i>8.2.1 Wind Tunnel Boundary Corrections.....</i> | <i>67</i> |
| <i>8.2.2 Corrections to Measured Quantities.....</i> | <i>68</i> |
| 8.3 Calibrations & Uncertainty of Experimental Data | 71 |
| <i>8.3.1 Comparison to Other Test Facilities</i> | <i>72</i> |
| 9. DISCUSSION & COMPUTED RESULTS..... | 73 |
| 9.1 Laminar to Turbulent Boundary-Layer Transition | 74 |
| 9.2 Lift, Drag, Moment of S1223 and 1% Gurney Flap Airfoils..... | 76 |
| 9.3 Pressure, Skin-Friction, Velocity-Profiles, Separation Locations | 84 |
| 9.4 Detailed Flow-Structures | 93 |
| 9.5 Calculation Convergence History..... | 102 |
| 9.6 True vs. Tested S1223 Performance Comparison | 107 |
| 9.7 Sources of Error in Computations..... | 110 |

| | |
|--|------------|
| 10. CONCLUSION | 112 |
| REFERENCES | 114 |
| APPENDIX A. VISCOUS FLUXES..... | 122 |
| APPENDIX B. TRUE AND TESTED S1223 AIRFOIL COORDINATES | 124 |

TABLE OF FIGURES

| | |
|--|----|
| Figure 6.0. Predator - Unmanned Aerial Vehicle (UAV) on a Simulated Navy | |
| Reconnaissance Flight | 50 |
| Figure 6.1. Plot of the True and Tested S1223 Airfoil Coordinates..... | 50 |
| Figure 6.2. Close-up of the True and Tested S1223 Airfoils near the Leading Edge..... | 51 |
| Figure 6.3. Close-up of the True and Tested S1223 Airfoils near the Trailing Edge | 51 |
| Figure 6.4. Plot of the Difference between True and Tested S1223 Airfoil Coords. | 52 |
| Figure 6.5. Grid No. I: C-mesh (248x61) | 55 |
| Figure 6.6. Close-up of Grid No. I: C-mesh (248x61) | 55 |
| Figure 7.1. Hypothesized Trailing Edge Flow Conditions of an Airfoil with a Gurney | |
| Flap | 59 |
| Figure 7.2. Close-up of the S1223 with a Gurney Flap ($h = 1/8''$, $t = 1/64''$, $c = 12''$) | 60 |
| Figure 7.3. Grid Used for the Gurney Flap, (Grid No. IV: C-mesh 317x61)..... | 61 |
| Figure 7.4. Close-up of Gurney Flap at the Trailing Edge (268 x 61) C-mesh | 61 |
| Figure 8.1. Schematic of the Low-Speed Wind Tunnel Used to Obtain Experimental | |
| Data..... | 63 |
| Figure 9.1. Plot of the Assumed Location of Laminar to Turbulent Transition Point.... | 76 |
| Figure 9.2. Lift Coefficient vs. Angle of Attack Plot..... | 82 |
| Figure 9.3. Drag Coefficient vs. Angle of Attack Plot..... | 82 |

| | |
|--|----|
| Figure 9.4. Computed L/D (Lift to Drag ratio) vs. C_l | 83 |
| Figure 9.5. Moment Coefficient vs. Angle of Attack Plot | 83 |
| Figure 9.6. Pressure Coefficient (C_p) vs. x/c Plot ($\text{Alpha} = -2^\circ$) | 88 |
| Figure 9.7. Pressure Coefficient (C_p) vs. x/c Plot ($\text{Alpha} = 4^\circ$) | 88 |
| Figure 9.8. Pressure Coefficient (C_p) vs. x/c Plot ($\text{Alpha} = 8^\circ$) | 89 |
| Figure 9.9. Pressure Coefficient (C_p) vs. x/c Plot ($\text{Alpha} = 14^\circ$) | 89 |
| Figure 9.10. Skin-friction Coefficient (C_f) vs. x/c Plot ($\text{Alpha} = -2^\circ$) | 90 |
| Figure 9.11. Skin-friction Coefficient (C_f) vs. x/c Plot ($\text{Alpha} = 4^\circ$) | 90 |
| Figure 9.12. Skin-friction Coefficient (C_f) vs. x/c Plot ($\text{Alpha} = 8^\circ$) | 91 |
| Figure 9.13. Skin-friction Coefficient (C_f) vs. x/c Plot ($\text{Alpha} = 14^\circ$) | 91 |
| Figure 9.14. Separation Location (x/c) vs. Angle of Attack (Alpha) | 92 |
| Figure 9.15. Velocity Profiles on Upper Surface of the S1223 Airfoil ($\alpha=14^\circ$) at Stations: $x/c = 0.082, 0.228, 0.438, 0.613, 0.715, 0.878, 0.940$ and 0.981 | 92 |
| Figure 9.16. Leading Edge Separation Bubble Predicted by the BB Model ($\text{Alpha}=-2^\circ$) | 96 |
| Figure 9.17. The Fully-attached Flow Predicted by the SA Model ($\text{Alpha}=-2^\circ$) | 96 |
| Figure 9.18. Plot of Stream Traces with Pres. Contours (plain S1223: $\text{Alpha}=2^\circ$) | 97 |
| Figure 9.19. Plot of Stream Traces with Pres. Contours (S1223 w. GF: $\text{Alpha}=2^\circ$) | 97 |
| Figure 9.20. Plot of Velocity Vectors with Pressure Contours (plain S1223: $\text{Alpha}=2^\circ$) | 98 |

| | |
|--|------------|
| Figure 9.21. Plot of Velocity Vectors with Pres. Contours (S1223 w. GF: Alpha=2°) .. | 98 |
| Figure 9.22. Plot of Stream Traces with Pres. Contours (plain S1223: Alpha=10°)..... | 99 |
| Figure 9.23. Plot of Stream Traces with Pres. Contours (S1223 w. GF: Alpha=10°) | 99 |
| Figure 9.24. Plot of Velocity Vectors with Pres. Contours (plain S1223: Alpha=10°). | 100 |
| Figure 9.25. Plot of Velocity Vectors with Pres. Contours | |
| (S1223 w. GF: Alpha=10°) | 100 |
| Figure 9.26. Close-up of Stream Traces with Pressure. Contours (S1223 w. GF: | |
| Alpha=10°) | 101 |
| Figure 9.27. Plot of Stream Traces with Pressure Contours at Max. Lift Conditions | |
| (C_{l_max}, Alpha=14°)..... | 101 |
| Figure 9.28. Convergence History (Alpha=10°) Showing Maximum-Residual vs. | |
| Iteration Number..... | 106 |
| Figure 9.29. Convergence History of the C_l vs. Iteration Number (Alpha=10°)..... | 106 |
| Figure 9.30. Convergence History of the C_d vs. Iteration Number (Alpha=10°) | 107 |
| Figure 9.31. C_l - Comparison between the True and Tested S1223 Airfoils | 107 |
| Figure 9.32. C_d - Comparison between the True and Tested S1223 Airfoils..... | 108 |
| Figure 9.33. C_m - Comparison between the True and Tested S1223 Airfoils | 108 |
| Figure 9.34. Comparison of L/D vs. C_l for the True and Tested S1223 Airfoils | 109 |

Nomenclature

- a_1 = constant, $a_1 = 0.31$ (SST)
 arg_1 = argument of blending function F_1 , used by turbulence model (SST)
 arg_2 = argument of function F_2 , used by turbulence model (SST)
 A = Jacobian matrix $\partial \mathcal{J} / \partial q$
 \hat{A}_i = Jacobian matrices
 A^+ = matrix used in the flux difference Δf^\pm
 A^+ = constant, $A^+ = 26$ (BB)
 A_2^+ = constant, $A_2^+ = 10$ (BB)
 A^- = matrix used in the flux difference Δf^\pm
 c = airfoil chord (c)
 c = scaled artificial speed of sound
 c_{b1} = constant, $c_{b1} = 0.1355$ (SA)
 c_{b2} = constant, $c_{b2} = 0.622$ (SA)
 c_{t1} = constant, $c_{t1} = 1.0$ (SA)
 c_{t2} = constant, $c_{t2} = 2.0$ (SA)
 c_{t3} = constant, $c_{t3} = 1.2$ (SA)
 c_{t4} = constant, $c_{t4} = 0.5$ (SA)
 c_{v1} = constant, $c_{v1} = 7.1$ (SA)
 c_{w1} = constant, $c_{w1} = c_{b1} / \kappa^2 + (1 + c_{b2}) / \sigma$ (SA)
 c_{w2} = constant, $c_{w2} = 0.3$ (SA)
 c_{w3} = constant, $c_{w3} = 2.0$ (SA)
 c_{ϵ_1} = constant, $c_{\epsilon_1} = 1.2$ (BB)
 $c_{\epsilon_{21}}$ = constant, $c_{\epsilon_{21}} = 2.0$ (BB)
 c_μ = constant, $c_\mu = 0.09$ (BB)
 C_d = airfoil drag coefficient (C_d), $D / (q_\infty c)$
 C_{du} = uncorrected airfoil drag coefficient
 C_D = wing drag coefficient, $D / (q_\infty S)$
 C_f = skin friction coefficient (C_f)
 C_l = airfoil lift coefficient (C_l), $l / (q_\infty c)$
 C_{lu} = uncorrected airfoil lift coefficient
 C_L = wing lift coefficient, $L / (q_\infty S)$

- C_m = airfoil moment coefficient (C_m), $M_{c/4}/(q_\infty S)$
 $C_{m,c/4}$ = airfoil pitching moment coefficient about the quarter chord point
 C_p = Pressure coefficient, $(P - P_\infty)/q_\infty$
 CD_{ω} = positive component of the cross-diffusion term (SST)
 ΔC_{lsc} = change in lift coefficient due to streamline curvature
 d = distance to the closest wall, ft. (SA)
 d_t = distance from the field point to the trip point (located on a wall), (SA)
 D = Wing drag, lbf or N
 D = Flow variable array
 e, f = Navier-Stokes eq. convective terms
 e_v, f_v = Navier-Stokes eq. viscous fluxes
 \hat{e}_v = viscous flux
 E, F = Navier-Stokes eq. and continuity convective terms
 E_v, F_v = Navier-Stokes eq. and continuity viscous fluxes
 \hat{E}_i = generalized flux vectors, $\hat{E}_i = \hat{E}, \hat{F}$ for $i = 1, 2$
 f = flux vector, (used in Upwind Differencing)
 \hat{f}_v = viscous flux
 f_{t1} = function involved in the transition terms (SA)
 f_{t2} = function involved in the transition terms (SA)
 f_{v1} = function (SA), $f_{v1} = \chi^3 / (\chi^3 + c_{v1}^3)$
 \tilde{f} = numerical flux, (used in Upwind Differencing)
 Δf^\pm = flux difference across positive or negative traveling waves
 F_1 = blending function used in turbulence model (SST)
 F_2 = function used by turbulence model (SST)
 f_w = function given in the destruction terms (SA)
 h_{ts} = test section height
 I = Identity matrix
 I_m = modified identity matrix
 $I_{i\tau}$ = diagonal matrix
 Im = modified identity matrix with a zero in the first diagonal entry
 J = Jacobian of the coordinate transformation
 k = Kinetic energy
 k_x = normalized metrics, $i = 1, 2$
 k_y = normalized metrics, $i = 1, 2$
 K_1 = wind-tunnel correction constant for solid blockage effects (0.74)
 K_{vel} = ratio of upstream velocity to velocity at model quarter chord point

| | | |
|---------------|---|--|
| L | = | diagonal selection matrix |
| L | = | wing lift |
| M_v | = | model airfoil volume |
| N | = | total number of grid points |
| p | = | pressure, psi |
| \hat{p} | = | vector defined as $\hat{p} = p/J$ |
| P | = | preconditioner used in GMRES |
| P | = | turbulence production term (BB) |
| P_k | = | function used in turbulence model, $P_k = \nu_t \Omega^2$ (SST) |
| P_ω | = | function used in turbulence model, $P_\omega = \Omega^2$ (SST) |
| q | = | dynamic pressure, $1/2\rho V_\infty^2$ |
| q | = | vector of dependent variables (used in Upwind Differencing) |
| q_∞ | = | free stream dynamic pressure, $1/2\rho V_\infty^2$ |
| Q | = | scaled contravariant velocity |
| Q | = | vector of dependent variables (of pressure $-p$, $-u$ and $-v$ velocity components) |
| \hat{r} | = | residual (right-hand side of the momentum equation) |
| R | = | residual (composed of the convective and viscous terms- in the implicit scheme) |
| \hat{R} | = | residual vector |
| \tilde{R}_T | = | turbulent Reynolds number |
| Re | = | Reynolds number |
| S | = | magnitude of vorticity (SA) |
| S | = | wing area |
| \tilde{S} | = | function used by (SA) |
| t | = | time, sec |
| u | = | matrix of velocities |
| u | = | Cartesian velocity component |
| u_i | = | Cartesian velocity components, $u_i = u, v$ |
| U | = | contravariant velocity component |
| U, V | = | contravariant velocities |
| U_t | = | friction velocity, $U_\infty \sqrt{(C_f/2)}$ |
| U_∞ | = | freestream velocity |
| ΔU | = | difference between the velocity at the field point and that at the trip (SA) |
| v | = | Cartesian velocity component |
| V | = | contravariant velocity component |
| V_c | = | corrected velocity |
| V_u | = | uncorrected velocity |
| x, y | = | Cartesian coordinates (distance along chord, distance normal to the surface) |
| x | = | Cartesian spatial coordinate |

- x_i = Cartesian spatial coordinates, $x_i = x, y$
 Δx_i = grid spacing along the wall at the trip (SA)
 X = matrix of right eigenvectors of A
 X^{-1} = inverse matrix of right eigenvectors of A
 X_i = matrix of the right eigenvectors
 X_i^{-1} = inverse matrix of the right eigenvectors
 y = Cartesian spatial coordinate, ft
 y^+ = wall coordinate (BB)
 y^+ = yU_i/ν
 y = distance to the closest no-slip surface (SST)
 Δy = distance to the next grid point away from the wall (SST)
- \sim = denotes nondimensionalized variables
 α = angle of attack
 α_u = uncorrected angle of attack
 $\Delta\alpha_{sc}$ = change in angle of attack due to streamline curvature
 β = artificial compressibility parameter
 β_1 = constant, $\beta_1 = 0.0828$ (SST)
 β^* = constant, $\beta^* = 0.09$ (SST)
 ε = coefficient used in the upwind differencing
 ε = Dissipation
 ε_b = total blockage correction factor (solid and wake)
 ε_{sb} = solid blockage correction factor
 ε_{wb} = wall blockage correction factor
 γ_1 = constant, $\gamma_1 = 0.41$ (SST)
 γ_2 = constant used by turbulence model (SST)
 ∇ = gradient operator (SA)
 ξ, η = Body fitted coordinates
 ξ = computational space direction coordinate
 Λ_i = diagonal matrix of eigenvalues, $\Lambda_i = \text{diag}(\lambda_1, \lambda_2, \lambda_3)$
 λ_i = eigenvalues, $i = 1, 2, 3$
 κ = constant, $\kappa = 0.41$ (BB, SA, SST)
 η = computational space direction coordinate
 ρ = density, lbm/ft^3
 ν = kinematic viscosity
 ν_t = turbulent eddy viscosity
 ω_i = vorticity at the trip (SA)
 τ = pseudo-time parameter, sec

- τ_{ij} = viscous stress tensor
- τ_w = shear stress
- $\Delta \tau$ = pseudo time-step size
- σ = wind-tunnel correction parameter, $(\pi^2/48)(c/h)^2$
- σ = constant, $\sigma = 2/3$ (SA)
- σ_{k1} = constant, $\sigma_{k1} = 0.85$ (SST)
- $\sigma_{\omega1}$ = constant, $\sigma_{\omega1} = 0.5$ (SST)
- ξ_x = metric of the curvilinear-coordinate transformation
- ξ_y = metric of the curvilinear-coordinate transformation
- Ω = vector of the variable to be held constant (boundary conditions)
- Ω = magnitude of the vorticity (SST)
- χ = non-dimensional eddy viscosity variable (SA)
- ϕ = constant (SST)
- ϕ_1 = constant from the Wilcox $k-\omega$ model (SST)

Subscripts

- m = psuedo-time level
- n = quantities at time $t = n \Delta t$
- ref* = reference quantities (free stream quantities)
- i, j = spatial indices
- ∞ = Denotes freestream conditions

Superscripts

- n = n^{th} time step
- $n+1$ = $(n+1)^{\text{th}}$ time step
- n = iteration number
- n = pseudo-time level

Shorthand Notation

- BB = Baldwin and Barth turbulence model
- CFD = computational fluid dynamics
- GF = Gurney flap
- GMRES = generalized minimum residual
- ILU = incomplete lower-upper factorization
- INS = Incompressible Navier Stokes equations
- INS2D = Incompressible Navier-Stokes 2D Code
- LR = Gauss-Seidel line-relaxation
- LE/TE = airfoil leading edge/trailing edge
- PR = Point Jacobi relaxation

SA = Spallart-Allmaras one-equation turbulence model
SST = two-equation k - ω turbulence model
TRX = laminar to turbulent transition

1. INTRODUCTION

Many challenges lie ahead in the design of effective high-lift/low-drag systems in low-speed aerodynamics. Payload, range and endurance of low speed civilian/military transports are dictated and often limited by the performance of their high lift systems.¹ To be efficient, a high lift system must allow large payload capacity (for a given wing section), long range/endurance for a given gross weight and at the same time be economically feasible. Generation of increased lift has other potential benefits, including steeper take-off ascent (to reduce noise in the area surrounding the airport), increase in the climb lift-to-drag ratio, L/D (to attain cruise altitude faster) and the desirable increase in fuel economy. These objectives are best achieved through the use of efficient high-lift low Reynolds number (LRN) wing systems.² Increased understanding of such systems will surely play an important role in designing the next generation of low-speed transport aircraft, whether for civilian or military applications.

To improve current designs of low-speed, high-lift wing sections, there is a strong need to have an increased knowledge of the flow physics involved. Further, understanding of the flow physics will without a doubt require both computational and experimental efforts. With the computer advances of recent years, computational fluid dynamics (CFD) is playing more than ever a large role in this effort. The motivation for this study is to use computational tools that are currently available to accurately predict the lift, drag and

moment coefficients at various angles of a high lift airfoil section, and to examine factors involved in boundary layer separation. To this day, the low-speed (low Reynolds number) regime is still not completely understood, making this task very formidable. In such situations the laminar boundary-layer first separates, then becomes unstable, transitions to turbulent flow and reattaches to the airfoil surface forming a bubble (usually on the suction side of the airfoil).² Principal cause of the high drag produced is the separation bubble at the low Reynold numbers. Among other problems, turbulent boundary layer separation, Reynolds number effects, boundary-layer transition for even single-element geometries all present a challenge to numerical investigators. Although some of these problems are inherently three-dimensional, much remains to be learned from examining two-dimensional models.

The choice of a wing section (or airfoil) is one of the most important considerations in the design of high lift transport aircraft, as is the choice of high-lift devices. Although the existing library of low Reynolds number airfoils is extensive, to this date only a few are suitable for low speed applications. Wind-tunnel tests have confirmed some 15% more lift on the "S1223" airfoil² (than other comparable high-lift LRN airfoils), which satisfies the design criteria by efficiently generating high-lift at a design Reynolds number of 2×10^5 . This very efficient high-lift LRN airfoil is especially suited for small unmanned-aerial-vehicles (UAVs) that need to carry heavy payloads for long periods of time. Unlike very complex and often cumbersome multi-element high-lift devices, one mechanically very simple device is the Gurney flap. On the order of 1% of the airfoil

chord length in size, the Gurney flap in this study is an elbow-like structure placed on the pressure side of the airfoil at the trailing edge. Simple, but yet very effective, this small flap has the potential to further enhance the lift capability with only a small increase in drag.

The objective of the present study is to provide qualitative/quantitative data on the performance of the “S1223”, high-lift, low Reynolds number airfoil (in free stream conditions, $Re=2 \times 10^5$) and to make a close examination of the flowfield. The computed lift, drag, moment, pressure, skin-friction coefficients and velocity profiles on the suction side of the airfoil are presented. In addition to the baseline S1223 airfoil, the effects of adding a 1% chord Gurney flap to the pressure side of the airfoil are investigated. The results are compared to experimental wind-tunnel data wherever possible. Experimental data² come from an open-return, 2.8 x 4 x 8 ft. low-turbulence wind tunnel. Furthermore, a comparison is made between the “true” S1223 as originally designed (with a sharp, cusp-like trailing edge, TE) and the slightly altered “tested” airfoil having a finite width TE (coordinates of both the true and tested airfoils are included in Appendix B).

A two-dimensional numerical investigation of the incompressible, viscous, turbulent flow is performed by solving the incompressible Navier-Stokes (INS) equations with the INS2D code. The solution algorithm employs the method of pseudocompressibility and utilizes an upwind differencing scheme for the convective fluxes and an implicit line relaxation. Three different turbulence models are used to calculate the high-lift, turbulent, airfoil flow. The turbulence models include the one-

equation *Baldwin and Barth*³ (BB), *Spalart-Allmaras*⁴ (SA) and the two-equation $k-\omega$ (SST) model.⁵ It is noted that, numerous investigators have studied airfoil flows using various turbulence models. For example, a computational multi and single element airfoil study was performed by Rogers.^{6,7} Also, the NACA4412 with a Gurney flap was studied by Cummings et al.⁸ The fully turbulent and laminar-to-turbulent boundary layer flows are compared. Employing a structured grid with a single zone in generalized curvilinear coordinates, the hyperbolic grid generator HYPGEN⁹ is used to generate the necessary computational meshes. The development, implementation, and the solution of the INS equations using pseudo-compressibility, upwind differencing and an implicit scheme in the solution algorithm are discussed in the following chapters.

2. THEORETICAL BACKGROUND & METHOD OF SOLUTION OVERVIEW

This section briefly discusses the governing equations of the high-lift, viscous, turbulent flow and the numerical algorithm employed in its solution.^{6,7} Detailed study/development of the method used in the solution is given in Sections 3 through 5.

2.1 Governing Equations/Numerical Algorithm

The flow physics of a low-speed, incompressible Newtonian fluid is governed by the incompressible Navier-Stokes equations, which result from applying the laws of conservation of mass and momentum to an infinitesimal, fixed control volume. When transformed to generalized (body-fitted) curvilinear coordinates, Reynold's averaged, and non-dimesionalized, the Navier Stokes¹⁰ equations can be expressed as follows:

$$\frac{\partial}{\partial \xi} \left(\frac{U}{J} \right) + \frac{\partial}{\partial \eta} \left(\frac{V}{J} \right) = 0 \quad (2.1)$$

$$\frac{\partial \hat{u}}{\partial t} = -\frac{\partial}{\partial \xi} (\hat{e} - \hat{e}_v) - \frac{\partial}{\partial \eta} (\hat{f} - \hat{f}_v) = -\hat{r} \quad (2.2)$$

where J is the Jacobian of the transformation (to body fitted coordinates ξ, η), U and V are the contravariant velocities, \hat{e} and \hat{f} are the convective terms; and \hat{e}_v and \hat{f}_v are the

viscous fluxes. The solution of these equations is accomplished by the method of artificial compressibility of Chorin.¹¹ In this method, a pseudo-time derivative of pressure is added to the continuity equation, forming a hyperbolic system of equations, that can be marched in pseudo-time to a steady state solution. The pseudo-time derivative of pressure has the form:

$$\frac{\partial p}{\partial \tau} = -\beta \nabla \cdot \hat{u} \quad (2.3)$$

where τ represents pseudo-time and β is the artificial compressibility parameter. With the added pseudo-time term, the Navier-Stokes equations take on the following form:

$$\frac{\partial \hat{D}}{\partial \tau} = -\frac{\partial}{\partial \xi} (\hat{E} - \hat{E}_v) - \frac{\partial}{\partial \eta} (\hat{F} - \hat{F}_v) \quad (2.4)$$

$$\hat{D} = \frac{1}{J} \begin{bmatrix} P \\ u \\ v \end{bmatrix} \quad \hat{E} = \frac{1}{J} \begin{bmatrix} \beta U \\ \xi_x P + uU + \xi_t u \\ \xi_y P + vU + \xi_t v \end{bmatrix} \quad (2.5)$$

$$\hat{F} = \frac{1}{J} \begin{bmatrix} \beta V \\ \eta_x P + uV + \eta_t u \\ \eta_y P + vV + \eta_t v \end{bmatrix} \quad \hat{E}_v = \frac{v}{J} \begin{bmatrix} 0 \\ \hat{e}_v \end{bmatrix} \quad \hat{F}_v = \frac{v}{J} \begin{bmatrix} 0 \\ \hat{f}_v \end{bmatrix} \quad (2.6)$$

Capable of solving both steady-state and time-dependent flow problems, the implicit numerical scheme used in this work is the INS2D code of Rogers.¹² The algorithm uses an upwind-biased flux-difference splitting technique for the convective terms and central differencing for the viscous terms. The upwind differencing gives a natural dissipation to the algorithm, with no further need for generating dissipation

artificially. Accuracy in the code is obtained in the numerical solution by subiterating the solution in pseudo-time for each physical time step. In the solution procedure, equations are solved using an implicit line relaxation scheme which allows the use of very large pseudo-time steps, leading to fast convergence for the steady state, as well as for the subiterations of time-dependent problems. In short, the scheme can be written in delta form as:

$$\left[\frac{I}{J\Delta\tau} + \frac{\partial \hat{R}}{\partial D} \right] (D^{n+1} - D^n) = -\hat{R}^n \quad (2.7)$$

where D is the array containing the flow variables, I is the identity matrix and R is the right hand side. The superscript n denotes the know quantities at the n -th time step and $n+1$ the unknowns at the $n+1$ pseudo-time step.

3. GOVERNING EQUATIONS AND ARTIFICIAL COMPRESSIBILITY

In this section, governing equations for flow of an incompressible (constant density), viscous, Newtonian fluid are presented (Rogers¹³). The artificial compressibility concept along with the generalized coordinate transformation is also introduced. Details of the formulation for the solution for both steady and unsteady (time-dependent) problems are given in two dimensions (2-D). The 2-D formulation is an obvious subset of the 3-D system, with differences in the viscous fluxes and the eigensystem of the Jacobian of the convective flux vectors.

3.1 Incompressible Navier-Stokes Equations

Based on the universal laws of conservation of mass and momentum, the fundamental equations of fluid dynamics are as follows. The time-dependent (unsteady), two-dimensional (2-D), viscous, incompressible (constant density) flow of a Newtonian fluid applied to an infinitesimal, fixed control volume is governed by the Navier-Stokes equations. The equations to be presented are first nondimensionalized using the following relations:

$$\begin{aligned} \tilde{u}_i &= \frac{u_i}{u_{ref}}, & \tilde{x}_i &= \frac{x_i}{x_{ref}}, & \tilde{t} &= \frac{t u_{ref}}{x_{ref}}, \\ \tilde{p} &= \frac{p - p_{ref}}{\rho u_{ref}^2}, & \tilde{\tau}_{ij} &= \frac{\tau_{ij}}{\rho u_{ref}^2}, & \tilde{\nu} &= \frac{\nu}{x_{ref} u_{ref}} = Re^{-1} \end{aligned} \quad (3.1)$$

where, for $i = 1$, and 2 respectively, $u_i = u, v$ are the two Cartesian velocity components, $x_i = x, y$ are the Cartesian spatial coordinates, p represents the pressure, ρ the density, t represents time, ν is the kinematic viscosity, Re is the Reynolds number, τ_{ij} represents the viscous stress tensor, and the subscript "ref" stands for the reference quantities. For external flows in general, reference quantities are chosen to be the free stream quantities. The 2-D Navier-Stokes equations which govern incompressible (constant density) flow, written in conservative form are (the tildes are dropped for convenience)

$$\frac{\partial u}{\partial x} + \frac{\partial v}{\partial y} = 0 \quad (3.2)$$

$$\frac{\partial \bar{u}}{\partial t} + \frac{\partial}{\partial x}(e - e_v) + \frac{\partial}{\partial y}(f - f_v) = 0 \quad (3.3)$$

where

$$\begin{aligned} \bar{u} &= \begin{bmatrix} u \\ v \end{bmatrix} & e &= \begin{bmatrix} u^2 + p \\ u v \end{bmatrix} \\ f &= \begin{bmatrix} v u \\ v^2 + p \end{bmatrix} & e_v &= \begin{bmatrix} \tau_{xx} \\ \tau_{xy} \end{bmatrix} & f_v &= \begin{bmatrix} \tau_{yx} \\ \tau_{yy} \end{bmatrix} \end{aligned} \quad (3.4)$$

When modeling turbulent flow, the above equations represent the Reynolds averaged quantities. Using the Boussinesq approximation for the Reynolds stress, the viscous stress tensor τ_{ij} can be written in the following form:

$$\tau_{ij} = (\nu + \nu_t) \left(\frac{\partial u_i}{\partial x_j} + \frac{\partial u_j}{\partial x_i} \right) \quad (3.5)$$

where ν_t is the turbulent eddy viscosity. Note, various turbulence models included in the INS2D code are to be discussed in the following sections.

3.2 Curvilinear Coordinate Transformation

For convenience in the numerical calculations and in order to facilitate the use of time-varying, body fitted coordinates for any particular type of geometry, the equations are transformed into generalized coordinates¹⁴ using:

$$\begin{aligned} \xi &= \xi(x, y, t) \\ \eta &= \eta(x, y, t) \end{aligned} \quad (3.6)$$

The curvilinear coordinate transformation when applied to the governing equations (3.2-3) results in the following set of equations:

$$\frac{\partial}{\partial \xi} \left(\frac{U}{J} \right) + \frac{\partial}{\partial \eta} \left(\frac{V}{J} \right) = 0 \quad (3.7)$$

$$\frac{\partial \hat{u}}{\partial t} = -\frac{\partial}{\partial \xi}(\hat{e} - \hat{e}_v) - \frac{\partial}{\partial \eta}(\hat{f} - \hat{f}_v) = -\hat{r} \quad (3.8)$$

where \hat{r} is the right-hand side of the momentum equation (eq. 3.8), J is the Jacobian of the transformation and all other parameters are defined as:

$$\begin{aligned} \hat{u} &= \frac{1}{J} \begin{bmatrix} u \\ v \end{bmatrix} \\ \hat{e} &= \frac{1}{J} \begin{bmatrix} \xi_x P + uU + \xi_t u \\ \xi_y P + vU + \xi_t v \end{bmatrix} \\ \hat{f} &= \frac{1}{J} \begin{bmatrix} \eta_x p + uV + \eta_t u \\ \eta_y p + vV + \eta_t v \end{bmatrix} \\ U &= \xi_x u + \xi_y v \\ V &= \eta_x u + \eta_y v \end{aligned} \quad (3.9)$$

The quantities \hat{e} and \hat{f} represent the convective terms, U and V are the contravariant velocity components and the metrics of the coordinate transformation are represented as

$$\xi_x = \frac{\partial \xi}{\partial x}, \quad \xi_y = \frac{\partial \xi}{\partial y}, \text{ etc.}$$

The degree of complexity of the differential form of the viscous fluxes varies depending on two assumptions: 1) whether the flow computations are taking place on an orthogonal mesh; and 2) whether the viscosity is spatially constant (Newtonian fluid in laminar flow).

The form of the viscous fluxes in generalized coordinates, \hat{e}_v and \hat{f}_v for the four possibilities (nonconstant viscosity on a nonorthogonal mesh, nonconstant viscosity on an orthogonal mesh, constant viscosity on a nonorthogonal mesh, and constant viscosity on an orthogonal mesh) are given in Appendix A.

3.3 Artificial Compressibility/Pseudocompressible Formulation

There are a number of approaches to solving the INS equations some of which include the velocity-vorticity method (non-primitive variable formulation) of Fasel¹⁵, the vector potential-vorticity method (VPVM) of Aziz and Hellums¹⁶ and the VPVM with a direct solver implementation by Hafez.¹⁷ Methods formulated in “primitive variables” fall into three groups. First of these is the pressure Poisson method (first introduced by Harlow and Welch¹⁸), second group is the fractional-step method (initially introduced by Chorin¹¹ and used by Kim & Moin¹⁹ and Rosenfeld et al.²⁰). For a complete description/discussion of all the mentioned methods, ref. 13 may be consulted. The third, primitive variable method is known as the artificial compressibility method. It was first introduced/implemented in obtaining steady-state solutions to the incompressible Navier-Stokes equations by Chorin²¹ and successfully used by Kwak et al.,²² for solving complex incompressible flow in generalized coordinates. Also, this method was recently used by several authors in computing time-accurate problems. The artificial compressibility method to be presented here for the solution of the incompressible Navier-Stokes equations in generalized coordinates was presented and used by Rogers.¹⁰ In this artificial compressibility formulation, a pseudo-time derivative of pressure is added to the continuity equation (eq. 3.7), directly coupling the pressure and velocity. When combined with the momentum equations (eq. 3.8), this forms a hyperbolic system of equations which

can be marched in pseudo-time to a steady state solution. The equations are advanced in physical time by iterating until a divergent-free velocity is obtained at the new physical time level. Not limited to steady state, the method can also be extended to solve time-dependent problems, by using subiterations in pseudo-time at every physical time step.²³ As mentioned by Rogers, if only the steady-state solution is desired, the artificial compressibility method can be very efficient, because it does not require the divergence-free velocity field to be obtained at each iteration.¹³ The artificial mechanism by which this corrects the flow field to satisfy the momentum equation is quite simple. If in a computational cell the net flux of mass becomes greater than zero (thus making the divergence of velocity positive), the pressure in that cell is decreased and through the action of the pressure gradient increases the force drawing the fluid toward the cell. On the other hand, if the divergence of the velocity is negative, the pressure increases also increasing the pressure force pushing the fluid away. In this way, the pressure and velocity fields are directly coupled and the addition of the time derivative of pressure to the continuity creates a hyperbolic system of equations complete with artificial pressure waves of finite speed.

4. SOLUTION OF THE INCOMPRESSIBLE NAVIER STOKES EQUATIONS

In the flow solver INS2D,¹⁰ the time derivatives in the momentum equation are differenced using a second-order three-point implicit formula

$$\frac{1.5\hat{u}^{n+1} - 2\hat{u}^n + 0.5\hat{u}^{n-1}}{\Delta t} = -\hat{r}^{n+1} \quad (4.1)$$

where the superscript n denotes the quantities at time $t = n\Delta t$ and \hat{r} is the residual given in eq. (3.8). To solve eq. (4.1) for a divergence free velocity at the $n+1$ time level, a pseudo-time level is introduced and is denoted by a superscript m . The implicit nature of the equations requires an iterative solution such that $\hat{u}^{n+1,m+1}$ approaches the new velocity \hat{u}^{n+1} , as the divergence of $\hat{u}^{n+1,m+1}$ approaches zero. To drive the divergence of this velocity to zero, the following artificial compressibility relation is introduced:

$$\frac{\partial p}{\partial \tau} = -\beta \nabla \cdot \hat{u}^{n+1,m+1} \quad (4.2)$$

where τ represents the pseudo-time and where β is the artificial compressibility parameter. Applying implicit Euler time differencing to eq. (4.2) and rewriting eq. (4.1) with the pseudo-time subscripts yields

$$\frac{\hat{p}^{n+1,m+1} - \hat{p}^{n+1,m}}{\Delta \tau} = -\beta \left[\frac{\partial}{\partial \xi} \left(\frac{U}{J} \right) + \frac{\partial}{\partial \eta} \left(\frac{V}{J} \right) \right]^{n+1,m+1} \quad (4.3)$$

$$\frac{1.5\hat{u}^{n+1,m+1} - 1.5\hat{u}^{n+1,m}}{\Delta t} = -\hat{r}^{n+1,m+1} - \frac{1.5\hat{u}^{n+1,m} - 2\hat{u}^n + 0.5\hat{u}^{n-1}}{\Delta t} \quad (4.4)$$

where $\hat{p} = p/J$. In this partially discretized form of the first equation, β and $\Delta\tau$ are not independent. However, both are kept separate at this point, because in the final discrete form, β will be independent of $\Delta\tau$ (due to a nonlinear coupling between the continuity equation and momentum equations due to the upwind differencing). The details of this will be discussed later in the upwind-differencing section. Note a pseudo-time derivative of pressure was added to the continuity equation (eq. 3.7), which directly coupled the pressure and velocity. When combined with the momentum equation (eq. 3.8), this formed a hyperbolic system of equations which can be marched in pseudo-time to a steady state solution.

Combining the two previous equations (eqs. 4.3 and 4.4) into one system of equations in delta form gives

$$I_{t\tau} \left(\hat{D}^{n+1,m+1} - \hat{D}^{n+1,m} \right) = -\hat{R}^{n+1,m+1} - \frac{I_m}{\Delta t} \left(1.5 \hat{D}^{n+1,m} - 2\hat{D}^n + 0.5\hat{D}^{n-1} \right) \quad (4.5)$$

where

$$\hat{D} = \frac{1}{J} \begin{bmatrix} p \\ u \\ v \end{bmatrix}; \quad D = J\hat{D}$$

$$\hat{R} = \frac{\partial}{\partial \xi} \left(\hat{E} - \hat{E}_v \right) + \left(\hat{F} - \hat{F}_v \right)$$

$$\hat{E} = \frac{1}{J} \begin{bmatrix} \beta U \\ \xi_x P + uU + \xi_t u \\ \xi_y P + vU + \xi_t v \end{bmatrix}$$

$$\hat{F} = \frac{1}{J} \begin{bmatrix} \beta V \\ \eta_x P + uV + \eta_t u \\ \eta_y P + vV + \eta_t v \end{bmatrix}$$

$$\hat{E}_v = \frac{v}{J} \begin{bmatrix} 0 \\ \hat{e}_v \end{bmatrix}$$

$$\hat{F}_v = \frac{v}{J} \begin{bmatrix} 0 \\ \hat{f}_v \end{bmatrix}$$

and where $I_{t\tau}$ is a diagonal matrix, and I_m is a modified identity matrix given as

$$I_{t\tau} = \text{diag} \left[\frac{1}{\Delta\tau}, \frac{1.5}{\Delta t}, \frac{1.5}{\Delta t} \right]$$

$$I_m = \text{diag}[0, 1, 1]$$

Finally, the residual term at the $m+1$ pseudo-time level is linearized giving the following equation in delta form

$$\begin{aligned} & \left[\frac{I_t}{J^{n+1}} + \left(\frac{\partial \hat{R}}{\partial \mathcal{D}} \right)^{n+1,m} \right] (D^{n+1,m+1} - D^{n+1,m}) = \\ & -\hat{R}^{n+1,m} - \frac{I_m}{\Delta t} (1.5\hat{D}^{n+1,m} - 2\hat{D}^n + 0.5\hat{D}^{n-1}) \end{aligned} \quad (4.6)$$

Note that the flux vectors \hat{E}_i are identical to what would be obtained from a steady-formulation of the artificial compressibility method, except for the presence of the time-varying metric terms, which will be non-zero only for a mesh which changes with time. Consequently, any differencing method which works well for the steady-state

formulation will be suitable for the current application. Although the use of upwind schemes based on flux-difference splitting is more costly than the use of central differencing, the upwind schemes have the advantage of adding dissipation to the system naturally, whereas the central differencing requires the use of artificial dissipation. It is for this reason the current work uses a flux-difference splitting scheme for the spatial discretization of the convective terms in eq. (4.6).

The Eigensystem of the Jacobian matrix of the flux vectors is required for the formation of the upwind differencing numerical fluxes. The 2-D eigensystem is presented here for the current formulation (for the 3-D formulation of the equations, consult Rogers²⁴ et al., or Hartwich and Hsu²⁵). It should be noted that the transformation given by the latter can become singular for certain values of the metrics.

The generalized flux vector for the 2-D system of equations is given by:

$$\hat{E}_i = \begin{bmatrix} \beta Q \\ k_x p + uQ + k_i u \\ k_y p + vQ + k_i v \end{bmatrix} \quad (4.7)$$

where $\hat{E}_i = \hat{E}, \hat{F}$ for $i = 1, 2$ respectively, and the normalized metrics are represented with

$$k_x = \frac{1}{J} \frac{\partial \xi_i}{\partial x}, i = 1, 2 \quad (4.8)$$

$$k_y = \frac{1}{J} \frac{\partial \xi_i}{\partial y}, i = 1, 2 \quad (4.9)$$

and the scaled contravariant velocity is

$$Q = k_x u + k_y v$$

The Jacobian matrices for this system are given by

$$\hat{A}_i = \frac{\hat{\mathcal{E}}_i}{\mathcal{D}} = \begin{bmatrix} 0 & \beta k_x & \beta k_y \\ k_x & k_x u + Q + k_t & k_y u \\ k_y & k_x v & k_y v + Q + k_t \end{bmatrix} \quad (4.10)$$

A similarity transformation for the Jacobian matrix is introduced

$$\hat{A}_i = X_i \Lambda_i X_i^{-1} \quad (4.11)$$

where

$$\begin{aligned} \Lambda_i &= \text{diag}(\lambda_1, \lambda_2, \lambda_3) \\ \lambda_1 &= Q + k_t \\ \lambda_2 &= Q + c + \frac{1}{2}k_t \\ \lambda_3 &= Q - c + \frac{1}{2}k_t \end{aligned} \quad (4.12)$$

in addition, c is the scaled artificial speed of sound given by the following

$$c = \sqrt{\left(Q + \frac{1}{2}k_t\right)^2 + \beta(k_x^2 + k_y^2)} \quad (4.13)$$

The matrix of the right eigenvectors is given by

$$X_i = \frac{1}{2\beta c \left(c^2 - \frac{1}{4}k_t^2\right)} \begin{bmatrix} 0 & \beta \left(c^2 - \frac{1}{4}k_t^2\right) & -\beta \left(c^2 - \frac{1}{4}k_t^2\right) \\ -2\beta c k_y & (u\lambda_2 + \beta k_x) \left(c + \frac{1}{2}k_t\right) & (u\lambda_3 + \beta k_x) \left(c - \frac{1}{2}k_t\right) \\ 2\beta c k_x & (v\lambda_2 + \beta k_y) \left(c + \frac{1}{2}k_t\right) & (v\lambda_3 + \beta k_y) \left(c - \frac{1}{2}k_t\right) \end{bmatrix} \quad (4.14)$$

and its inverse is given by

$$X_i^{-1} = \begin{bmatrix} k_y u - k_x v & -v \lambda_1 - \beta k_y & u \lambda_1 - \beta k_x \\ -\lambda_3 & \beta k_x & \beta k_y \\ -\lambda_2 & \beta k_x & \beta k_y \end{bmatrix} \quad (4.15)$$

4.1 Upwind Differencing

Upwind differencing is used in the INS2D solution scheme as a means of following the propagation of the artificial waves introduced by the artificial compressibility. The upwind differencing thus provides a dissipative scheme, which automatically suppresses any oscillations caused by the nonlinear main diagonal of the Jacobian of the residual, whereas a central-differenced flux vector would not. This helps to make the implicit scheme nearly diagonally dominant and contributes greatly to the robustness of the INS2D code. Even though the upwind flux differences are more costly to form, the speed-up in convergence can result in a significant savings in the required computing-time.

The flux-difference split form of upwind differencing used is represented for a one-dimensional (1-D) system. In its application to multi-dimensional problems, it is applied to each coordinate direction separately. The 1-D representation of a hyperbolic system of equations in conservation law form is given by

$$\frac{\partial q}{\partial t} + \frac{\partial f}{\partial x} = 0 \quad (4.16)$$

where q is the vector of dependent variables and f is the flux vector. A semi-discrete approximation to this equation is given by

$$\left(\frac{\partial q}{\partial t} \right)_j + \frac{[\tilde{f}_{j+1/2} - \tilde{f}_{j-1/2}]}{\Delta x} = 0 \quad (4.17)$$

where \tilde{f} is a numerical flux and j is a spatial index.

A flux resulting in a first-order scheme is defined by

$$\tilde{f}_{j+1/2} = \frac{1}{2} [f(q_{j+1}) + f(q_j)] - \frac{1}{2} [\Delta f^+_{j+1/2} - \Delta f^-_{j+1/2}] \quad (4.18)$$

where Δf^\pm is the flux difference across positive or negative traveling waves. The flux difference is taken as

$$\Delta f^\pm_{j+1/2} = A^\pm(\bar{q}) \Delta q_{j+1/2} \quad (4.19)$$

where A represents the Jacobian matrix $\partial f / \partial q$. The A^+ and A^- matrices are computed first by forming a diagonal matrix of the positive eigenvalues, and multiplying through by the similarity transform. Since the A^+ matrix plus the A^- matrix equals the original Jacobian matrix, we have

$$\begin{aligned} A^+ &= X \Lambda^+ X^{-1} \\ A^- &= A - A^+ \end{aligned} \quad (4.20)$$

where X is the matrix of right eigenvectors of A , and X^{-1} is its inverse. The flux difference is evaluated at the mid-point by using the average of q :

$$\bar{q} = \frac{1}{2}(q_{j+1} + q_j)$$

The Δq term is given by

$$\Delta q_{j+1/2} = \Delta q_{j+1} - q_j$$

A scheme of arbitrary order may be derived using these flux differences. Implementation of higher-order accurate schemes on the right-hand side of the equations does not require significantly more computational time if the flux differences Δf^\pm are all computed at once for a single line. A third-order upwind flux is defined by

$$\tilde{f}_{j+1/2} = \frac{1}{2}[f(q_{j+1}) + f(q_j)] + \frac{1}{6}[\Delta f^+_{j-1/2} - \Delta f^+_{j+1/2} + \Delta f^-_{j+1/2} - \Delta f^-_{j+3/2}] \quad (4.21)$$

where the flux differences are the same as in the first-order difference given by eq. (4.19). The primary problem with using schemes of accuracy greater than second-order occurs at the boundaries. Large stencils require special treatment at the boundaries, and a reduction of order is necessary. Therefore, when going to a higher-order accurate scheme, compactness is desirable. Such a compact scheme was used by Ra²⁶ using a fifth-order accurate upwind-biased stencil. A fifth-order fully upwind difference would require 11 points, but this upwind-biased scheme requires only 7 points. The form of this scheme is

$$\begin{aligned}
\tilde{f}_{j+1/2} &= \frac{1}{2} [f(q_{j+1}) + f(q_j)] \\
&+ \frac{1}{60} [-2\Delta f^+_{j-3/2} + 11f^+_{j-1/2} - 6f^+_{j+1/2} - 3f^+_{j+3/2}] \\
&+ \frac{1}{60} [2\Delta f^-_{j+5/2} - 11f^-_{j+3/2} + 6f^-_{j+1/2} + 3f^-_{j-1/2}]
\end{aligned} \tag{4.22}$$

At points adjacent to the boundary, the high-order stencils cannot be maintained, and the order of the scheme must be reduced. However, it is not necessary to reduce the accuracy to first-order. The following flux is used at points next to the boundary

$$\tilde{f}_{j+1/2} = \frac{1}{2} [f(q_{j+1}) + f(q_j)] - \frac{\varepsilon}{2} [\Delta f^+_{j+1/2} - \Delta f^-_{j+1/2}] \tag{4.23}$$

For $\varepsilon = 0$, this flux leads to a second-order central difference. For $\varepsilon = 1$, this is the same as the first-order upwind difference given by eq. (4.18). By including the delta-flux terms with a small value for the coefficient ε , near second-order accuracy is maintained, and the added dissipation ensures that no oscillations occur at the boundary. This boundary treatment has been found to work well for very small values of ε .

The right and left matrices given by equations (4.14 and 4.15) clearly show that the artificial compressibility parameter β will affect not only the continuity equations, but the momentum equations as well. An analysis for the Cartesian coordinate case shows that the dissipation terms added to the momentum equations will grow as the square root of β . This indicates that the value of β should be chosen with care when using the upwind-differencing of the momentum equations.

4.2 Implicit Scheme

This section describes a method for numerically representing and solving eq. (4.6).

The first consideration is the formulation of the Jacobian matrix of the residual vector \hat{R} required for the implicit side of the equation. Applying the semi-discrete formula given in eq. (4.17) to the flux vectors and a second-order central difference formula to the viscous terms, the residual at a discrete point $x_{i,j}$, $y_{i,j}$ is given by

$$R_{i,j} = \frac{\hat{E}_{i+1/2,j} - \hat{E}_{i-1/2,j}}{\Delta\xi} + \frac{\hat{F}_{i+1/2,j} - \hat{F}_{i-1/2,j}}{\Delta\eta} - \frac{(\hat{E}_v)_{i+1,j} - (\hat{E}_v)_{i-1,j}}{2\Delta\xi} - \frac{(\hat{F}_v)_{i,j+1} - (\hat{F}_v)_{i,j-1}}{2\Delta\eta} \quad (4.24)$$

where i and j are indices for the ξ and η directions, respectively. The generalized coordinates are chosen so that $\Delta\xi$ and $\Delta\eta$ are equal to one. Applying the first-order upwind numerical flux in eq. (4.18) gives

$$R_{i,j} = \frac{1}{2} \left[\hat{E}_{i+1,j} - \hat{E}_{i-1,j} + \hat{F}_{i,j+1} - \hat{F}_{i,j-1} - \Delta E^+_{i+1/2,j} + \Delta E^-_{i+1/2,j} + \Delta E^+_{i-1/2,j} - \Delta E^-_{i-1/2,j} - \Delta F^+_{i,j+1/2} + \Delta F^-_{i,j+1/2} + \Delta F^+_{i,j-1/2} - \Delta F^-_{i,j-1/2} - (\hat{E}_v)_{i+1,j} + (\hat{E}_v)_{i-1,j} - (\hat{F}_v)_{i,j+1} + (\hat{F}_v)_{i,j-1} \right] \quad (4.25)$$

The Jacobian matrix of the residual vector will form a banded matrix of the form:

$$\frac{\partial R}{\partial D} = B \begin{bmatrix} \frac{\partial R_{i,j}}{\partial D_{i,j-1}}, 0, \dots, 0, \frac{\partial R_{i,j}}{\partial D_{i=1,j}}, \frac{\partial R_{i,j}}{\partial D_{i,j}} \\ \frac{\partial R_{i,j}}{\partial D_{i+1,j}}, 0, \dots, 0, \frac{\partial R_{i,j}}{\partial D_{i,j+1}} \end{bmatrix} \quad (4.26)$$

However, the exact Jacobians of the flux differences can be very costly to form. Instead, approximate Jacobians of the flux differences as derived and analyzed by Barth²⁷ and Yee²⁸ are used:

$$\begin{aligned} \frac{\partial R_{i,j}}{\partial D_{i,j-1}} &\approx \frac{1}{2} \left(-\hat{B}_{i,j-1} - B^+_{i,j-1/2} + B^-_{i,j-1/2} \right) + (\gamma_2)_{i,j-1} \\ \frac{\partial R_{i,j}}{\partial D_{i-1,j}} &\approx \frac{1}{2} \left(-\hat{A}_{i-1,j} - A^+_{i-1/2,j} + A^-_{i-1/2,j} \right) + (\gamma_1)_{i-1,j} \\ \frac{\partial R_{i,j}}{\partial D_{i,j}} &\approx \frac{1}{2} \left(A^+_{i+1/2,j} + A^+_{i-1/2,j} - A^-_{i+1/2,j} - A^-_{i-1/2,j} \right. \\ &\quad \left. B^+_{i,j+1/2} + B^+_{i,j-1/2} - B^-_{i,j+1/2} - B^-_{i,j-1/2} \right) \\ \frac{\partial R_{i,j}}{\partial D_{i+1,j}} &\approx \frac{1}{2} \left(\hat{A}_{i+1,j} - A^+_{i+1/2,j} + A^-_{i+1/2,j} \right) - (\gamma_1)_{i+1,j} \\ \frac{\partial R_{i,j}}{\partial D_{i,j+1}} &\approx \frac{1}{2} \left(\hat{B}_{i,j+1} - B^+_{i,j+1/2} + B^-_{i,j+1/2} \right) - (\gamma_2)_{i,j+1} \end{aligned} \quad (4.27)$$

where only the orthogonal mesh terms are retained for the implicit viscous terms giving

$$\begin{aligned} \gamma_1 &= \frac{\nu}{J} (\xi_x^2 + \xi_y^2) \text{Im} \frac{\partial}{\partial \xi} \\ \gamma_2 &= \frac{\nu}{J} (\eta_x^2 + \eta_y^2) \text{Im} \frac{\partial}{\partial \eta} \end{aligned} \quad (4.28)$$

where Im is a modified identity matrix with a zero in the first diagonal entry.

The matrix equation is solved using a line-relaxation method. The entire numerical matrix equation is formed from values at the previous time level. Then, the domain is swept in one or both of the two coordinate directions, once forward and once backward for each sweep. At each line perpendicular to the sweep direction, a tridiagonal matrix is formed. For the points not on this line, the implicit matrices are multiplied by the latest known ΔD vector, and the resulting vector is shifted to the right-hand side of the equations.

4.2.1 Implicit Scheme Selection in the Flow Solver INS2D

In this section, the choice and rationale for the choice of an implicit scheme used in the INS2D flow solver is given. A brief introduction/description is given for each of the algorithms. For a complete discussion/development, consult: “*A Comparison of Implicit Schemes for the Incompressible Navier-Stokes Equations with Artificial Compressibility*” by Rogers.²⁹ The schemes include Point-Jacobi relaxation (PR), Gauss-Seidel line-relaxation (LR), incomplete lower-upper decompositions (ILU), and the generalized minimum residual (GMRES) method, preconditioned with the PR, LR, and ILU schemes. As mentioned earlier, the INS2D flow solver uses a third-order, upwind-differencing scheme to discretize the convective terms, and the viscous terms are differenced using second-order central differences. The system of equations is integrated in pseudo-time

using an implicit Euler time discretization. The resulting discrete system of equations is of the following form

$$\frac{Q^{n+1} - Q^n}{\Delta\tau} = -R^{n+1} \quad (4.29)$$

where Q is the vector of dependent variables (of pressure $-p$, $-u$ and $-v$ velocity components), $\Delta\tau$ is the pseudo time-step size, superscript n is the iteration number and R is the residual (composed of the convective and viscous terms). This system is linearized about pseudo-time level n , resulting in

$$\left(\frac{1}{\Delta\tau} + \frac{\partial R^n}{\partial Q} \right) \Delta Q = -R^n \quad (4.30)$$

where $\Delta Q = Q^{n+1} - Q^n$. Eq. (4.30) is iterated until a steady-state solution is obtained at which time, $R^n \approx 0$. In the INS2D code, the Jacobian of R on the left-hand side (LHS) of eq. (4.30) is formed using a residual, based on first-order differencing of the convective terms, whereas third-order differencing is used on the right-hand side (RHS). Further, approximate Jacobians of flux differences from the upwind differencing scheme are used, because the exact Jacobians of these terms would require the formation of a tensor (more details can be found in ref. 30). The first order LHS matrix is used to reduce the bandwidth of the resulting LHS matrix, resulting in lower memory and computational requirements. However, as already mentioned, the use of approximate Jacobians can also slow down the convergence.

For turbulent flow calculations, the INS2D code employs a turbulence model of *Baldwin and Barth*³ (BB). Note, in different run scenarios, two other turbulence models are used, the one-equation *Spalart-Allmaras*⁴ (SA), and the two-equation $k-\omega$ ^{5,31,32} (SST) model. The BB requires the solution of a single convective-diffusive partial-differential equation. This equation is uncoupled from the mean flow equations during the solution process. The convective terms in the turbulence model are discretized using a first-order upwind-differencing scheme. The resulting equation for the turbulence model is discrete and of the form of eq. (4.30), with the exception that Q now represents a single variable at each grid point instead of three variables. The LHS of eq. (4.30) is a banded matrix composed of five diagonals, each containing scalar entries. In all cases being solved, the turbulent model equation is solved using the same implicit scheme as the mean-flow equations.

If the LHS of eq. (4.30) were composed of the exact Jacobians and solved exactly at each time step with an infinite time step, this would be a Newton iteration. In this case, quadratic convergence could be obtained if the Q^n was close to the exact solution. But the LHS is composed of an approximate Jacobian of the RHS and the turbulence model is uncoupled from the mean-flow equations, so the solution procedure is not a Newton iteration. Thus, the goal is to obtain an approximate solution to eq. (4.30) in an efficient manner, and attempts are made to accomplish this task using several different methods. The discrete form of the matrix from the LHS of eq. (4.30) is a pentadiagonal banded

matrix, where each entry on the diagonal consists of 3x3 blocks. Equation (4.30) can be written as

$$[D, 0, \dots, 0, A, B, C, 0, \dots, 0, E] \Delta Q = -R^n \quad (4.31)$$

where A , B , C , D and E are the block diagonals. In the implementation of all of the implicit schemes, the code first computes and stores all the terms in eq. (4.31), and then it proceeds with the solution procedure. The storage requires $48N$ words, where N is the total number of grid points. In the following, subscript i refers to a single grid-point index, when one can consider all of the grid points in a single vector of length N . The subscripts j and k are indices in the two computational-space directions ξ and η , respectively. Whenever the data is stored in a single index vector, it is done so that j is the fastest changing (inner) index.

4.2.2 Incomplete Lower-upper Factorization (ILU)

In the ILU formulation, the matrix on the LHS of eq. (4.31) is replaced with the following factors:

$$[D, 0, \dots, 0, A, B' [B']^{-1} [B', C, 0, \dots, 0, E]$$

$$B'_i = B_i - A_i C'_{i-1} - D_i E'_{i-j_{\max}}$$

$$C'_i = [B'_i]^{-1} C_i \quad (4.32)$$

$$E'_i = [B'_i]^{-1} E_i$$

Multiplying these factors together, one can observe that a matrix of the same structure as the original LHS is obtained, with the exception that there are additional diagonals of nonzero entries created just above the D diagonal and just below the E diagonal. These new entries are ignored in the approximation. This operation is known as ILU with the zero additional fill, or ILU(0) (for further details on implementing ILU schemes with additional fill consult ref. 33).

The ILU solver requires some significant initialization work; namely, the computation and storage of the B' diagonal. This requires $9N$ extra storage locations. When used as a preconditioner, this is done once at the beginning of the GMRES solution process, and then used repeatedly during the GMRES iteration cycle. The solution can be vectorized by setting up an inner loop operating on all points on a diagonal line defined by $j+k = \text{constant}$.

4.2.3 Point Relaxation (PR)

The PR algorithm iteratively solves a block diagonal system formed by multiplying all the non-main block diagonals by the current estimate for ΔQ and moving this to the RHS. This is done for each point, sweeping sequentially through the mesh. A forward sweep is composed of

$$[B]\Delta Q^{l+1} = -R^n - [D, 0, \dots, 0, A]\Delta Q^{l+1} - [C, 0, \dots, 0, E]\Delta Q^l, \quad (4.33)$$

and a backward sweep is performed by solving

$$[B]\Delta Q^{l+1} = -R^n - [D, 0, \dots, 0, A]\Delta Q^l - [C, 0, \dots, 0, E]\Delta Q^{l+1} \quad (4.34)$$

In the current computations, a forward sweep plus a backward sweep count as one sweep, denoted as PR(1). The solution process is initialized by setting ΔQ to zero. Then a lower-upper (LU) factorization of the B block is formed. Thus, the number of operations to solve this equation is minimized during the repeated sweeping process. This process can be vectorized by setting up an inner loop to compute ΔQ for all points on a diagonal line through the mesh given by $j+k = \text{constant}$.

4.2.4 Line Relaxation (LR)

The LR process is similar to the PR method, except that more terms are kept on the LHS and a block tridiagonal system of equations is solved for an entire grid line at once. The algorithm is implemented so that either computational direction can be selected to be the sweep direction. For solving lines of constant k , a forward sweep is composed of

$$[A, B, C]\Delta Q^{l+1} = -R^n - [D]\Delta Q^{l+1} - [E]\Delta Q^l, \quad (4.35)$$

and a backward sweep is performed by solving

$$[A, B, C]\Delta Q^{l+1} = -R^n - [D]\Delta Q^l - [E]\Delta Q^{l+1} \quad (4.36)$$

A forward-plus-backward sweep counts as two sweeps and is denoted by LR(2). This process is also initialized by setting ΔQ to zero. Then, an LU factorization of the tridiagonal system is formed to minimize the number of operations during the sweeping process. The sweeping process is recursive and can't be vectorized. It should be noted that the LR and PR schemes each require the same number of operations per point per sweep, because whereas the PR only has to solve a block diagonal system instead of a block tridiagonal system (it has additional block vector multiply operations for the RHS terms). The PR terms scheme will run faster on a vector computer because it can be vectorized. In practice, the PR routine runs about twice as fast as the LR routine (consult ref. 29 for further details).

In both the PR and LR algorithms, zonal boundary conditions are enforced during the sweeping process. Typically, multiple sweeps are performed during each iteration. When computing a multiple zone grid, all zones are swept once before moving onto a second sweep. After each zone is swept, this new ΔQ^{l+1} is passed to all other zones that use this zone for their boundary conditions. In this fashion, information is propagated across zonal boundaries implicitly.

4.2.5 Generalized Minimum Residual Method (GMRES)

The GMRES algorithm of Saad and Schultz³⁴ is an iterative procedure for solving the linear system of equations of the form

$$Mx - b = 0 \quad (4.37)$$

or, in the left preconditioned form

$$PMx - Pb = 0 \quad (4.38)$$

where P is the preconditioner which is an approximation to M^{-1} . The preconditioner matrix PM will have a smaller spectral radius than M , resulting in faster convergence for the GMRES procedure. This procedure performed in the k search directions, known as GMRES(k), forms an approximation to the solution vector x is given by

$$x_k = x_0 + y_1 v_1 + \dots + y_k v_k, \quad (4.39)$$

where x_0 is an initial guess to the solution x , and the v_i terms are orthonormal vectors formed from the process

$$r_0 = PMx_0 - Pb, \quad v_1 = \frac{r_0}{\|r_0\|} \quad (4.40)$$

Iterate: For $j = 1, 2, \dots, k$:

$$\begin{aligned}
h_{i,j} &= (PMv_j, v_i), \quad i = 1, 2, \dots, j \\
w_{j+1} &= PMv_j - h_{1,j}v_1 - h_{2,j}v_2 - \dots - h_{j,j}v_j \\
h_{j+1,j} &= \|w_{j+1}\| \\
v_{j+1} &= \frac{w_{j+1}}{\|w_{j+1}\|}
\end{aligned}$$

The y_i coefficients are computed so that the norm of the residual $\|Mx_k - b\|$ is minimized. An estimate for this norm is available during each iteration of the solution process as a function of the $h_{i,j}$ variables. The process requires approximately $(4 + k)3N$ words of memory to apply to the mean-flow equations (therefore it's not practical to use large values of k). Because of memory usage, the flow solver is limited to k being no more than ten ($k=10$). A restart capability of the GMRES algorithm allows the iteration process to continue beyond $k=10$ in this case. This is done simply by setting $x_0=k_{10}$, and restarting from the beginning. If a total of 30 GMRES search directions is specified to the code, then two restarts are used. This is designated as GMRES(30).

The GMRES algorithm is implemented here so that the iterations can be stopped based on either of two criteria. The first is simply to specify the maximum number of search directions to be used. The second is to specify a tolerance for the error. One advantage of the GMRES process is that an accurate estimate of the norm of the residual is computed as part of the solution process. Using numerical tests, it was found that it was generally more efficient (in terms of obtaining a converged steady-state flow solution)

to specify a set number of search directions for GMRES than it was to specify a tolerance for the norm of the residual. Because the preconditioner must be utilized once for each GMRES search direction, it needs to be relatively cheap. Thus, when the PR and LR schemes are used as a preconditioner for GMRES, only two sweep of the relaxation process are used.

The choice of the implicit scheme for the solution of the Incompressible Navier-Stokes equations with the artificial compressibility method is based on empirical/experimental data from Rogers.²⁹ When conducting computer experiments, the efficiency of the schemes was measured in terms of computing time required to obtain a steady-state solution. Furthermore, Rogers compared a number of different implicit schemes (including the LR, PR, ILU and GMRES method preconditioned with the PR, LR and ILU schemes) in solving several two-dimensional flow problems. Two such problem included the 2-D flow over a *NACA4412* airfoil and the flow over a three-element airfoil using overset grids. For each geometry/method, calculations were run to determine the optimal time-step size (hence the $\Delta\tau$), optimal value of β , and optimum number of relaxation sweeps or GMRES search directions. Most cases were found to run best using an infinite time step, which was implemented by setting $\Delta\tau = 10^{12}$, so that $1/\Delta\tau$ was on the order of machine zero. In some cases, this large step resulted in an instability, and the time step had to be reduced. In other cases, a large time step calculation remained stable, but a smaller time step run resulted in better efficiency. These calculations determined the best possible performance of each method for a particular case. In calculating the flow

over the *NACA4412* airfoil at a Reynolds number of 1.5 million and an angle of attack of 13.87 degrees, the resultant calculations were also compared to experimental data of Coles and Wadcock.³⁵ To see the effects of grid refinement and to find the convergence rates, different size grids 119x31, 237x61, 473x121 and 945x241 were compared. Using the same flow solver INS2D, results showed the GMRES method preconditioned with the ILU scheme outperformed all other method by at least a factor of two. Examining the convergence rate trends using the various grid sizes, all of the methods required a reduction in the time-step size, and an increase in the amplification factor and cost per point as the grid density increased. Based on these results, the GMRES method preconditioned with the ILU (GMRES(10)+ILU(0), $\beta = 1$, $dt = \Delta\tau = 0.1$) scheme was chosen for the current calculations, after performing a choice of parameters (β , dt and $\Delta\tau$) study. In addition, the GMRES+ILU method had an optimum convergence with the same value of β for all grid levels.

4.3 Boundary Conditions

Implicit boundary conditions are used for all boundaries, making it possible to use large time steps. At a no-slip surface, the velocity is specified to be zero, and the pressure at the boundary is obtained by specifying the pressure gradient normal to the wall to be zero. The boundary conditions used for inflow and outflow region are based on the method of characteristics. Although the implementation is slightly different, formulation of these boundary conditions is similar to that given by Merkle and Tsai.³⁶ The finite-speed waves which arise with the use of artificial compressibility are governed by the following relations

$$\frac{\partial \hat{D}}{\partial \tau} = \frac{\partial \hat{E}}{\partial \xi} = -\frac{\partial \hat{E}}{\partial D} \frac{\partial D}{\partial \xi} = -\hat{A} \frac{\partial D}{\partial \xi} = -X \Lambda X^{-1} \frac{\partial D}{\partial \xi}$$

then

$$X^{-1} \frac{\partial \hat{D}}{\partial \tau} = -\Lambda X^{-1} \frac{\partial D}{\partial \xi} \quad (4.41)$$

If one were to move the X^{-1} matrix inside the spatial and time derivative, then it can be noted that this would be a system of scalar equations (each of the form of a wave equation). The sign of the eigenvalue in the Λ matrix determines the direction of travel of the wave. For each positive (or negative) eigenvalue, there is a wave propagating information in the positive (or negative) ξ direction. The number of characteristic waves

propagating information from the interior of the computational domain to the boundary depends on the number of positive or negative eigenvalues. At the boundary, characteristics which bring information from the interior computational domain are used as part of the boundary conditions. The rest of the information should come from outside the computational domain, and consequently we're free to specify some variables.

There will either be one or two characteristics traveling toward the boundary from the interior, because there is always at least one positive eigenvalue and one negative eigenvalue. In order to select the proper characteristic waves, eq. (4.41) is multiplied by a diagonal selection matrix L one entry of which is the position of the eigenvalue we wish to select; L has zeros at all other locations. As a result

$$LX^{-1} \frac{\partial \hat{D}}{\partial \tau} = -L\Lambda X^{-1} \frac{\partial D}{\partial \xi} \quad (4.42)$$

Replacing the time derivative with an implicit Euler time step gives

$$\left(\frac{LX^{-1}}{J\Delta\tau} + L\Lambda X^{-1} \frac{\partial}{\partial \xi} \right) (D^{n+1} - D^n) = L\Lambda X^{-1} \frac{\partial D^n}{\partial \xi} \quad (4.43)$$

This gives either one or two relations, depending on the number of non-zero elements in L . To complete the set of equations, some variables must be specified to be constant. Defined here is a vector Ω of the variables to be held constant, such that

$$\frac{\partial \Omega}{\partial \tau} = 0 \rightarrow \frac{\partial \Omega}{\partial D} \frac{\partial D}{\partial \tau} = 0 \rightarrow \frac{\partial \Omega}{\partial D} (D^{n+1} - D^n) = 0 \quad (4.44)$$

Combining eqs. (4.43) and (4.44) gives

$$\left(\frac{LX^{-1}}{J\Delta\tau} + L\Lambda X^{-1} \frac{\partial}{\partial \xi} + \frac{\partial \Omega}{\partial D} \right) (D^{n+1} - D^n) = -L\Lambda X^{-1} \frac{\partial D^n}{\partial \xi} \quad (4.45)$$

eq. (4.45) can be used to update the variables implicitly at any of the inflow or outflow boundaries with the proper choice of L and Ω .

4.3.1 Inflow Boundary

At the inflow, there will be one characteristic wave traveling out of the computational domain since fluid is traveling into the domain. If the incoming fluid is traveling in the positive ξ direction, then

$$\begin{aligned} Q &> 0 \\ Q + c &> 0 \\ Q - c &< 0 \end{aligned} \quad (4.46)$$

This third eigenvalue will be the one we wish to select, and so L will have a one for the third diagonal entry. If the incoming fluid is traveling in the negative ξ direction, then

$$\begin{aligned} Q &< 0 \\ Q + c &> 0 \\ Q - c &< 0 \end{aligned} \quad (4.47)$$

and the second eigenvalue is the one corresponding to the wave propagation out of the computational domain. This requires a “1” in the second diagonal entry of L . Two different sets of specified variables have been used successfully for inflow boundaries. One set consists of the total pressure and the cross-flow velocity. This set is useful for problems in which the inflow velocity profile is not known. For this set, the Ω vector is

$$\Omega = \begin{bmatrix} p + \frac{1}{2}(u^2 + v^2) \\ 0 \\ v \end{bmatrix}; \quad \frac{\partial \Omega}{\partial D} = \begin{bmatrix} 1 & u & v \\ 0 & 0 & 0 \\ 0 & 0 & 1 \end{bmatrix} \quad (4.48)$$

The second possible set of specified variables consists of the velocity components. This is useful for problems in which a specific velocity profile is desired at the inflow. The Ω vector for this case is

$$\Omega = \begin{bmatrix} 0 \\ u \\ v \end{bmatrix}; \quad \frac{\partial \Omega}{\partial D} = \begin{bmatrix} 0 & 0 & 0 \\ 0 & 1 & 0 \\ 0 & 0 & 1 \end{bmatrix} \quad (4.49)$$

4.3.8 Outflow Boundary

At the outflow boundary there are two characteristic waves traveling out of the computational domain since fluid is also leaving the domain. If the fluid is traveling along the positive ξ direction then,

$$\begin{aligned}
 Q &> 0 \\
 Q + c &> 0 \\
 Q - c &< 0
 \end{aligned}
 \tag{4.50}$$

and ones are required in the first two diagonal entries of the L matrix. If the fluid is traveling in the negative ξ direction then,

$$\begin{aligned}
 Q &< 0 \\
 Q + c &> 0 \\
 Q - c &< 0
 \end{aligned}
 \tag{4.51}$$

and we require ones in the first and third diagonal entries of the L matrix. For all of the problems presented, the static pressure is specified at the outflow boundary, resulting in

$$\Omega = \begin{bmatrix} p \\ 0 \\ 0 \end{bmatrix}; \quad \frac{\partial \Omega}{\partial D} = \begin{bmatrix} 1 & 0 & 0 \\ 0 & 0 & 0 \\ 0 & 0 & 0 \end{bmatrix}
 \tag{4.52}$$

5. TURBULENCE MODELS

Three different turbulence models are used to calculate the high-lift, turbulent, airfoil flow. This section gives a short description/implementation of each of the models (for complete details see “*A comparison of Turbulence Models in Computing Multi-Element Airfoil Flows*”⁶). The turbulence models included are models of: 1) *Baldwin and Barth*³ (BB), 2) one-equation *Spalart-Allmaras*⁴ (SA) and 3) two-equation *k- ω* (SST) model. The last model was developed by Menter,^{5,31,32} based on the *k- ω* model of Wilcox³⁷ and the standard *k- ϵ* model. Models are implemented in the flow code in a modular, uncoupled fashion with the ability to handle multiple grid flows.

5.1 Baldwin Barth Model (BB)

Derived from a simplified form of the *k- ϵ* model equations, the BB model solves one transport equation for the turbulent Reynolds number \tilde{R}_τ , which is related to eddy viscosity ν_t . Transition from laminar to turbulent flow is introduced by multiplying the turbulence production term P in the equation, by a function whose range is from zero to one. In addition, the function is zero upstream of a user defined transition point, at which

the function is exponentially increased to a value of one, over two or three grid points.

The transport equation used by the BB model is given by

$$\begin{aligned} \frac{D(\tilde{\nu R}_T)}{Dt} = & (c_{\varepsilon_2} f_2 - c_{\varepsilon_1}) \sqrt{\tilde{\nu R}_T P} \\ & + \left(\nu + \frac{\nu_t}{\sigma_\varepsilon} \right) \nabla^2 (\tilde{\nu R}_T) - \frac{1}{\sigma_\varepsilon} (\nabla \nu_t) \cdot \nabla (\tilde{\nu R}_T) \end{aligned} \quad (5.1)$$

where ν is the kinematic viscosity, D/Dt is the substantial derivative, and the other parameters are defined by the following:

$$\begin{aligned} \frac{1}{\sigma_\varepsilon} = & (c_{\varepsilon_2} - c_{\varepsilon_1}) \frac{\sqrt{c_\mu}}{\kappa^2} \\ \nu_t = & c_\mu (\tilde{\nu R}_T) D_1 D_2 \\ D_1 = & 1 - \exp(-y^+ / A^+) \\ D_2 = & 1 - \exp(-y^+ / A_2^+) \end{aligned} \quad (5.2)$$

$$P = \nu_t \left(\frac{\partial U_i}{\partial x_j} + \frac{\partial U_j}{\partial x_i} \right) \frac{\partial U_i}{\partial x_j} \quad (5.3)$$

$$\begin{aligned} f_2(y^+) = & \frac{c_{\varepsilon_1}}{c_{\varepsilon_2}} + \left(1 - \frac{c_{\varepsilon_1}}{c_{\varepsilon_2}} \right) \left(\frac{1}{\kappa y^+} + D_1 D_2 \right) \left(\sqrt{D_1 D_2} \right. \\ & \left. + \frac{y^+}{\sqrt{D_1 D_2}} \left(\frac{1}{A^+} \exp(-y^+ / A^+) D_2 + \frac{1}{A_2^+} \exp(-y^+ / A_2^+) D_1 \right) \right) \end{aligned} \quad (5.4)$$

where $x_i = x, y$ and $U_i = u, v$ (the Cartesian velocity components) for $i = 1, 2$ respectively.

The y^+ wall coordinate is given by

$$y^+ = \frac{\sqrt{\tau_w / \rho}}{\nu} y \quad (5.5)$$

where τ_w is the shear stress at the nearest wall grid point and y is the distance from that same grid point. The constants used in the model are as follows

$$\begin{aligned} \kappa &= 0.41, \quad c_{\epsilon_1} = 1.2, \quad c_{\epsilon_2} = 2.0, \quad c_\mu = 0.09 \\ A^+ &= 26, \quad A_2^+ = 10 \end{aligned} \quad (5.6)$$

At a no-slip wall boundary, \tilde{R}_τ is set to zero. At an outflow boundary and at slip-wall boundaries, the normal derivative is set to zero.

5.2 Spalart-Allmaras Model (SA)

One transport equation for a non-dimensional eddy viscosity variable χ is solved by the SA model. Similar to the BB model, the SA equation is different by the addition of a non-viscous destruction term that depends on the distance to the wall. SA also includes a more sophisticated transition model which provides a smooth laminar to turbulent transition at points specified by the user. The eddy viscosity is given by

$$\nu_t = \nu \chi f_{\nu 1} \quad (5.7)$$

$$f_{\nu 1} = \frac{\chi^3}{\chi^3 + c_{\nu 1}^3} \quad (5.8)$$

The transport equation for χ is given by

$$\begin{aligned} \frac{D\chi}{Dt} = & c_{b1}[1-f_{t2}]\tilde{S}\chi + \frac{\nu}{\sigma}\left[\nabla\cdot((1+\chi)\nabla\chi) + c_{b2}(\nabla\chi)^2\right] \\ & - \left[c_{w1}f_w - \frac{c_{b1}}{\kappa^2}f_{t2}\right]\left(\frac{\chi}{d}\right)^2 + \frac{f_{t1}}{\nu}\Delta U^2 \end{aligned} \quad (5.9)$$

where ∇ is the gradient operator,

$$\begin{aligned} \tilde{S} & \equiv S + \frac{\nu\chi}{\kappa^2 d^2} f_{v2} \\ f_{v2} & = 1 - \frac{\chi}{1 + \chi f_{v1}} \end{aligned} \quad (5.10)$$

S is the magnitude of vorticity and d is the distance to the closest wall. The function f_w in the destruction terms is given by

$$\begin{aligned} f_w & = g \left[\frac{1 + c_{w3}^3}{g^6 + c_{w3}^6} \right]^{1/6} \\ g & = r + c_{w2}(r^6 - r) \\ r & \equiv \frac{\nu\chi}{\tilde{S}\kappa^2 d^2} \end{aligned} \quad (5.11)$$

The functions f_{t1} and f_{t2} involved in the transition terms are given by

$$\begin{aligned} f_{t1} & = c_{t1}g_t \exp\left(-c_{t2}\frac{\omega_t^2}{\Delta U^2}\left[d^2 + g_t^2 d_t^2\right]\right) \\ f_{t2} & = c_{t3} \exp(-c_{t4}\chi^2) \\ g_t & \equiv \min(0.1, \Delta U/\omega_t \Delta x_t) \end{aligned} \quad (5.12)$$

where d_t is the distance from the field point to the trip point (located on a wall); ω_t is the vorticity at the trip; ΔU is the difference between the velocity at the field point and that at

the trip and Δx_t is the grid spacing along the wall at the trip. The constants in this model are given by

$$\begin{aligned}
 \sigma &= 2/3, \quad \kappa = 0.41 \\
 c_{b1} &= 0.1355, \quad c_{b2} = 0.622 \\
 c_{w1} &= c_{b1}/\kappa^2 + (1 + c_{b2})/\sigma \\
 c_{w2} &= 0.3, \quad c_{w3} = 2.0 \\
 c_{v1} &= 7.1, \quad c_{t1} = 1.0 \\
 c_{t2} &= 2.0, \quad c_{t3} = 1.2 \\
 c_{t4} &= 0.5
 \end{aligned} \tag{5.13}$$

At a no-slip wall boundary, $\chi = 0$. At an outflow boundary and at slip wall boundaries, the normal derivative of χ is set to zero.

5.3 k - ω (SST) Model

The SST model is a two-equation k - ε model developed by Menter⁵; it is based on the earlier k - ω model of Wilcox.³⁷ The Wilcox model was found to perform quite well in a study of various adverse pressure gradient flows performed by Menter.³¹ However, Menter³² also showed that this model is very sensitive to the specification of freestream values for ω . The formulation of the model⁵ removes the freestream dependency with a zonal approach, which automatically switches from the Wilcox model in the mean wall region, to an equivalent of the k - ε model³⁸ away from the wall and in free shear layers. In order to improve the sensitivity of the model to adverse pressure gradients, Menter

introduced a modification to the definition of the eddy-viscosity that accounts for the transport of the principal turbulent shear stress.⁵ This modification is based on Bradshaw's assumption that the principal shear stress is proportional to the turbulent kinetic energy over most of the boundary layer. Transition is implemented in the same manner as the BB model.

The transport equations for k and ω are given by

$$\frac{Dk}{Dt} = P_k - \beta^* \omega k + \nabla \cdot [(1 + \sigma_k \nu_t) \nabla k] \quad (5.14)$$

$$\begin{aligned} \frac{D\omega}{Dt} = & \gamma P_\omega - \beta \omega^2 + 2(1 - F_1) \sigma_{\omega 2} \frac{\nu_t}{k} \nabla k \cdot \nabla \omega \\ & + \nabla \cdot [(1 + \sigma_\omega \nu_t) \nabla \omega] \end{aligned} \quad (5.15)$$

$$\begin{aligned} P_k &= \nu_t \Omega^2 \\ P_\omega &= \Omega^2 \end{aligned}$$

where Ω is the magnitude of the vorticity. The constants in the model are blended using the following, where ϕ represents one of the constants given by

$$\phi = F_1 \phi_1 + (1 - F_1) \phi_2 \quad (5.16)$$

where the ϕ_1 constants are from the Wilcox k - ω model, with an adjustment to $\sigma_{\omega 1}$:

$$\begin{aligned} \sigma_{k1} &= 0.85, \quad \sigma_{\omega 1} = 0.5 \\ \beta_1 &= 0.0828, \quad \beta^* = 0.09 \\ \kappa &= 0.41, \quad \gamma_1 = 0.41, \quad \gamma_2 = \beta_2 / \beta^* - \sigma_{\omega 1} \kappa^2 / \sqrt{\beta^*} \end{aligned}$$

The blending function is defined as

$$F_1 = \tanh(\arg_1^4)$$

$$\arg_1 = \min\left(\max\left(\frac{\sqrt{k}}{0.09\omega y}, \frac{500\nu}{\omega}\right), \frac{4\sigma_{\omega 2}k}{CD_{k\omega}y^2}\right) \quad (5.17)$$

where y is the distance to the closest no-slip surface and $CD_{k\omega}$ is the positive component of the cross-diffusion term in eq. (5.2):

$$CD_{k\omega} = \max\left(2\sigma_{\omega 2} \frac{1}{\omega} \nabla k \cdot \nabla \omega, 1 \times 10^{-20}\right)$$

The eddy-viscosity is defined as

$$\nu_t = \frac{\alpha_1 k}{\max(\alpha_1 \omega, \Omega F_2)} \quad (5.18)$$

where $\alpha_1 = 0.31$ and F_2 is given by

$$F_2 = \tanh(\arg_2^2)$$

$$\arg_2 = \max\left(2 \frac{\sqrt{k}}{0.09\omega y}, \frac{500\nu}{y^2 \omega}\right) \quad (5.19)$$

At a no-slip wall, the boundary conditions are $k = 0$ and

$$\omega = 10 \frac{6\nu}{\beta_1 (\Delta y)^2}$$

where Δy is the distance to the next grid point away from the wall. At outflow boundaries the gradient is equal to zero.

6. GEOMETRY MODELING AND GRID GENERATION

6.1 Geometry Modeling (Airfoil Discussion)

In this study, the geometry is a S1223 (11.93% thick, 8.67% camber, $C_{m,c/4} = -0.290$) airfoil² in free stream conditions. Especially designed for heavy lift cargo planes and unmanned aerial vehicles (UAV's), this airfoil has both civilian (e.g., scientific, meteorology and mapping) and military (e.g., electronic warfare and reconnaissance) applications. As mentioned by Folch,^{39,40} small UAV's are sometimes driven by the need to carry relatively heavy payloads for long periods of time. Typical mission of such aircraft may include a 24 hour endurance at an altitude of 100 ft. (mean sea level), with flight speeds ranging from 25-40 kts. and payload requirements varying from 10-25 lbs.⁴⁰ Example of a UAV currently being used by the US-Navy for reconnaissance is shown in fig. 6.0. Called the "Predator", this UAV provides "near real-time" infrared and color video to its mother-ship during flight and is capable of 50 hours of non-stop flight. Operated remotely by a detachment consisting of military pilots/technicians and with an average speed of approximately 70 knots, it has a wingspan of 48.4 feet, a length of 26.7 feet and weighs approximately 1500 lb., when fully fueled (cost around 3.2 million dollars). With potential to be used in many civilian/military applications, the S1223

satisfies the design criterion by efficiently generating high lift at low Reynolds number. The S1223 airfoil design philosophy⁴⁰ was to combine the favorable effects of concave pressure recovery and aft loading to achieve maximum lift at design Reynolds number of 2×10^5 . The original characteristics of this airfoil were achieved through the use of a suite of computational tools. In particular, several low-speed airfoil design and analysis codes were used, such as PROFOIL,⁴¹⁻⁴⁴ Eppler^{45,46} and either the ISES^{47,48} or XFOIL⁴⁹ codes. From a performance standpoint, the S1223 has a design C_l of about 2.11, which is one of the highest lift coefficients of any airfoil designed for Reynolds numbers of the order of 2×10^5 . Others of the same class include the CH10-48-13, FX63-137, FX74-CL5-140MOD, M06-13-128 and S1210 airfoils (for further details consult Selig²). Even though the existing “library” of low Reynolds number airfoils is extensive, to date only a few airfoils are suitable for high lift low Reynolds applications.

Included in this work is the true S1223 (true airfoil coordinates having a sharp, cusp-like trailing edge) as originally designed, and the wind tunnel tested S1223 (actual model coordinates). The average difference between these two airfoils is approximately .0099 inches (or .083% for a 12 in. chord). The plot of the true, the tested S1223 and the difference between the two airfoils is shown in figures 6.1 through 6.4. In addition, the effect of adding a Gurney flap to both the true and the tested airfoil section geometries was examined (see discussion on the Gurney flap).



Figure 6.0 *Predator* - Unmanned Aerial Vehicle (UAV) on a Simulated Navy Reconnaissance Flight (Photo by Navy Photographers Mate 3rd Class Jeffrey S. Viano)

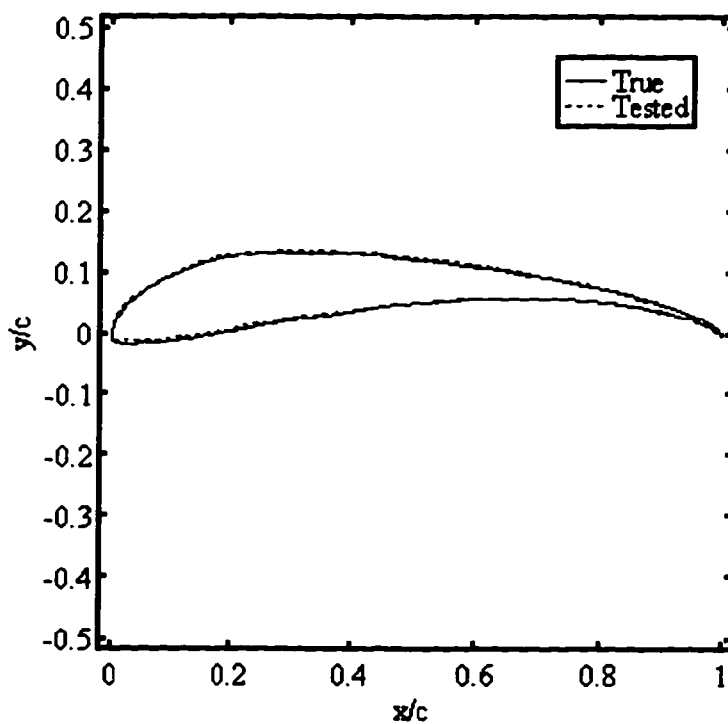


Figure 6.1. Plot of the True and Tested S1223 Airfoil Coordinates

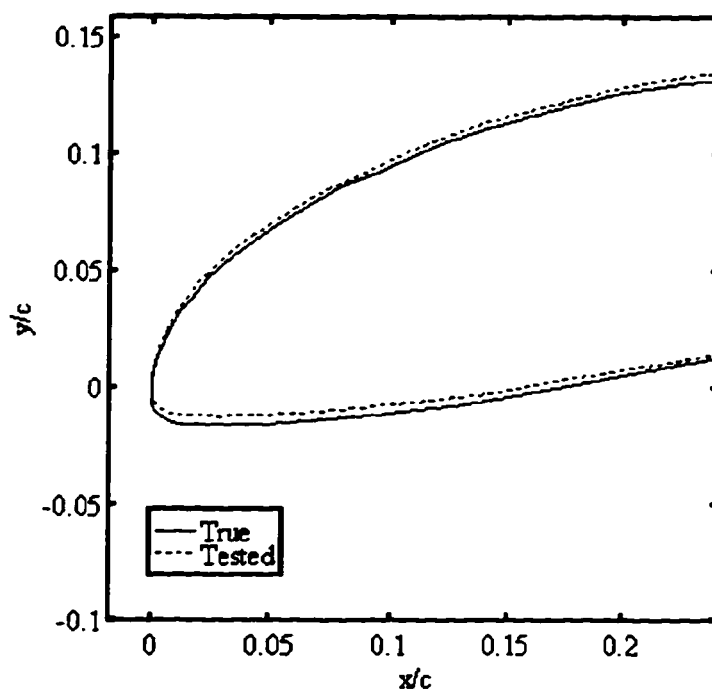


Figure 6.2. Close-up of the True and Tested S1223 Airfoils Near the Leading Edge

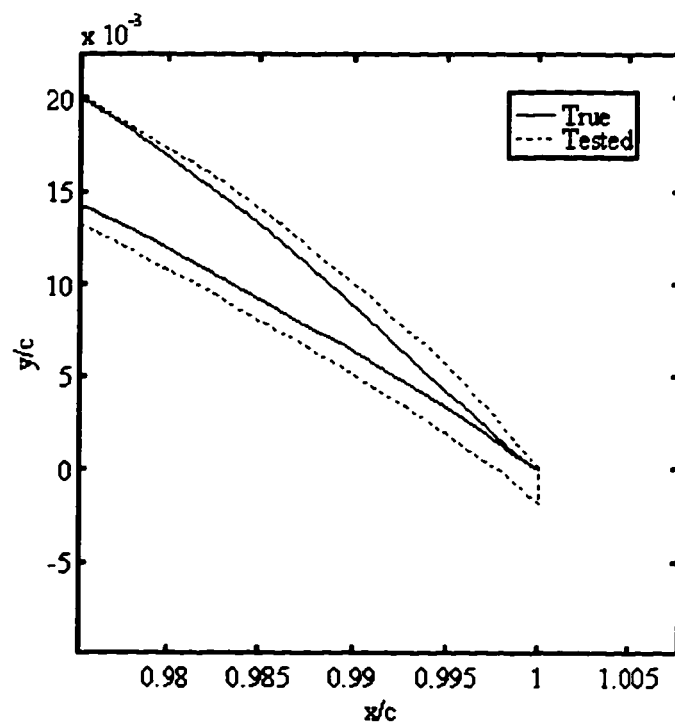


Figure 6.3. Close-up of the True and Tested S1223 Airfoils near the Trailing Edge

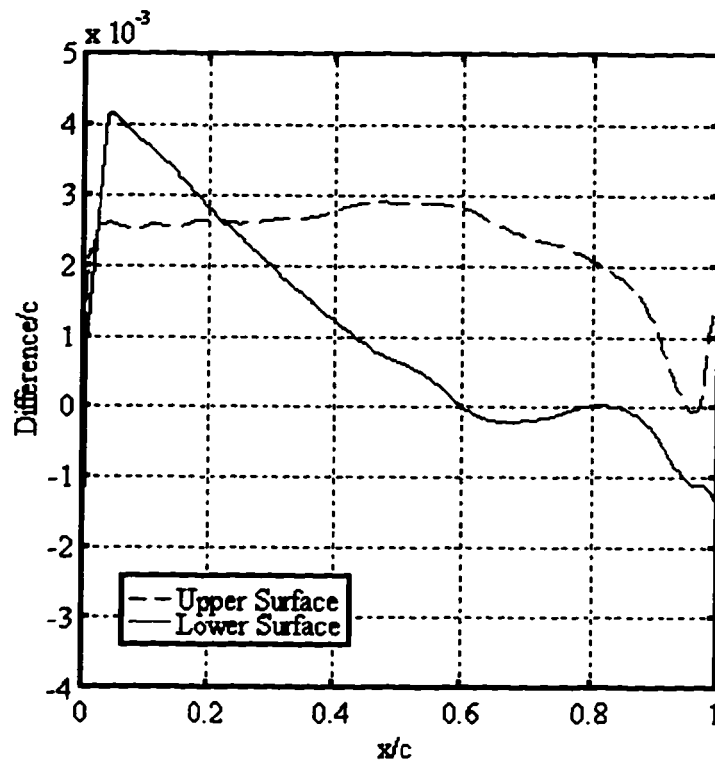


Figure 6.4. Plot of the Difference between True and Tested S1223 Airfoil Coordinates.

6.2 Grid Generation

The grid was constructed using the hyperbolic grid generation code HYPGEN, of Chan⁵⁰ et al. The Hypgen program is used to generate a 3-D volume grid over a user specified single block surface grid by marching away from the initial surface, with the step size given by a stretching function in the normal direction. The grid generation⁵⁰ is accomplished by solving the 3-D hyperbolic grid generation equations (two orthogonality

relations and one cell volume constraint). As an option, a 2-D grid can also be generated by specifying appropriate boundary conditions.

As an input file for HYPGEN, surface grids for both the S1223 and S1223 with a Gurney flap were generated (true and tested airfoil coordinates). These variable spacing surface grids included the coordinates of the airfoils, plus the upper and lower coordinates of the wake. Subsequently, all the grids generated with HYPGEN were C-meshes of different sizes. In addition, HYPGEN allowed to control the initial spacing (in the surface normal direction) and far field along the wake cut as well as having multiple L-regions (regions of specified initial and final spacing and distances to march out). The reason behind employing two separate L-regions was to reduce grid skewness. For all the grids, two L-regions were employed with a variable far field distance in the first L-region, to limit the growth of the grid in the normal direction. If this limit was absent the grid lines (especially at the trailing edge) would tend to bend too far forward resulting in an unsatisfactory skewed grid. Another advantage of employing two L-regions was the fact that both the far field distance and the initial normal grid spacing along the wake cut, in the region close to the body surface were made to increase linearly with distances downstream, resulting in fanning of the grid points in the wake. Note, to enhance the convergence/stability, elliptic smoothing was also performed across the wake region. The different C-mesh grids and their respective sizes used to model the true and the tested S1223 airfoil with and without the Gurney flap are summarized in Table 6.1 (grid No. I is shown in figures 6.5-6). Note the grids are numbered I, II, III and IV respectively and

will be referred to as such. Further, note that only the grids giving the best overall results were selected from two or three grids for each configuration, with the finer meshes generally yielding better results and accuracy at the expense of increased grid size. For all the grids, the far field distance (distance to the outer boundary of the C-mesh) was kept constant and only the number of points along the airfoil and its wake was varied. The initial spacing in the normal direction to capture the viscosity effects in the boundary layer was $0.20E-4$ or 0.002% of the chord.

| <i>Grid No.</i> | <i>I.</i> | <i>II.</i> | <i>III.</i> | <i>IV.</i> |
|----------------------------|------------------|---------------------------|--------------------|-----------------------------|
| C-mesh size | 248 x 61 | 268 x 61 | 301 x 61 | 317 x 61 |
| Type of Coordinates | True S1223 | True S1223 w. Gurney Flap | Tested S1223 | Tested S1223 w. Gurney Flap |

Table 6.1. Grid Size Summary of C-meshes and their Applications

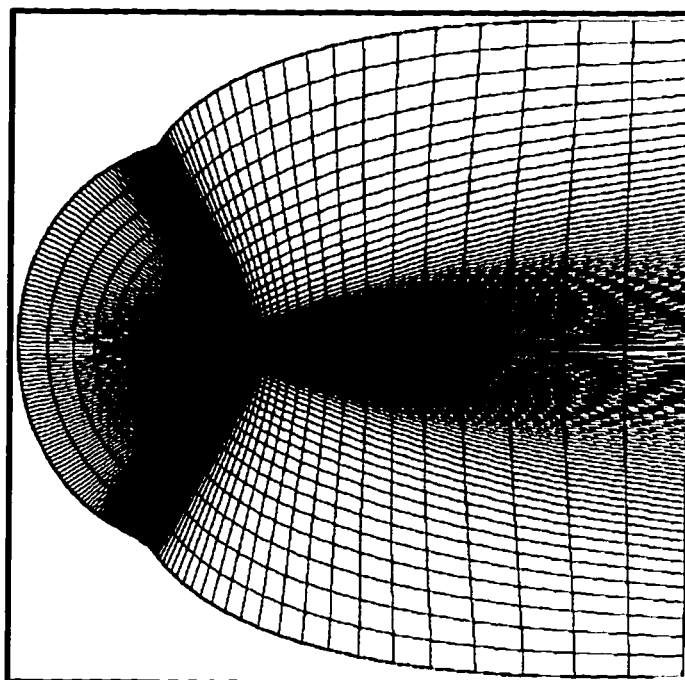


Figure 6.5. Grid No. I: C-mesh (248x61)

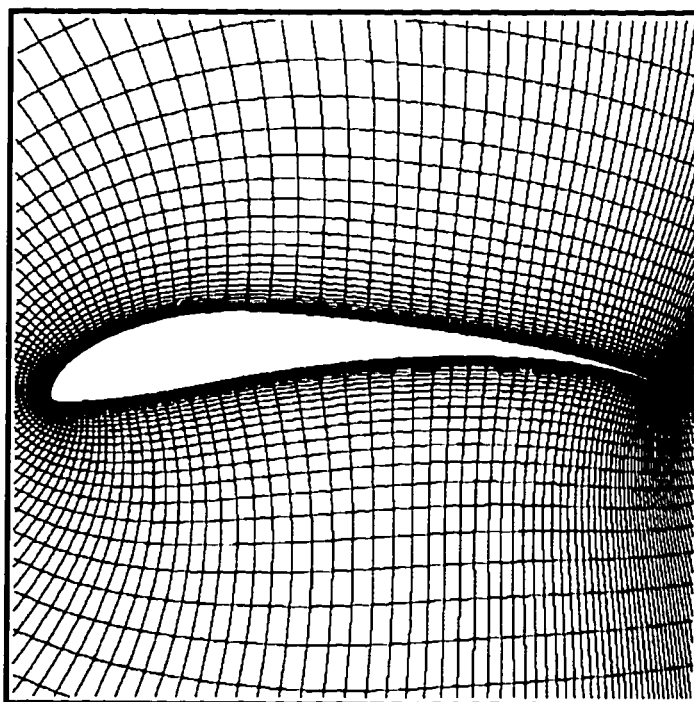


Figure 6.6. Close-up of Grid No. I: C-mesh (248x61)

7. THE GURNEY FLAP

7.1 Concept and Description of the Gurney Flap

One mechanically simple device for enhancing the lift (C_L) is the Gurney flap. From a geometry point of view, a Gurney flap is usually a small flat plate (the length of which is of the order of 1% of chord), located perpendicular to the pressure side of an airfoil at the trailing edge.⁵¹ Gurney flaps were first used on the inverted wings of race cars to provide a “down-force” to increase the adhesion of tires during acceleration, braking and cornering. Taking measurements by comparing corner and straightaway speeds with and without the flap, it was found that increasing the size of the flap (beyond approximately 2%) offered an increased down-force, but also increased the drag. Liebeck tested a 1.25% Gurney flap on a Newman airfoil, which is an airfoil defined by an elliptical nose on a straight line wedge. For this particular configuration, an increase in the lift coefficient and a small decrease in the drag coefficient was observed. Liebeck also hypothesized on the changes in the trailing edge flow-field due to the presence of a Gurney flap. Figure 7.1 shows the flow near the trailing edge of a conventional airfoil with a Gurney flap (at moderate lift coefficient) with an upstream separation bubble and two counter-rotating vortices. Basing his assumptions on the earlier explanation of the

flow mechanism by Khodadoust⁵² using a tufted probe, Liebeck observed a significant turning of the flow over the back side of the flap.

From results obtained thus far, one of the applications and virtues of the Gurney flap maybe that of lift enhancement, while reducing the drag on both the single and multi-element airfoil configurations. Other investigators have considered this concept experimentally (Duddy,⁵³ Jang⁵⁴) and computationally (Cummings⁸). An experimental wind tunnel investigation of the Gurney flap used on multi element race-car-wing was conducted by Largman and Katz⁵⁵ and Dykstra⁵⁶ on a four element car-wing. In the last two investigations, the Gurney flap was located on the trailing edge of the most aft wing. Largman and Katz reported that, using a 5% chord Gurney flap increased the lift coefficient of the wing by as much as 50% over that of the clean wing. However, as pointed out, the drag also increased to such an extent that the resulting L/D ratio was decreased at the design range of angle of attack (between 2 to 12 degrees). Similarly, Dykstra found that adding Gurney flap (on the order of 2% chord), increased the wing lift coefficient as well as the drag coefficient. Wing L/D with the Gurney flap was again slightly lower than the clean configuration.

Further studies of Roesch and Vuillet⁵⁷ from an Aerospatiale wind tunnel test, involved the use of the Gurney flap mounted on horizontal tails and vertical fins of helicopter models. Horizontal stabilizer (aspect ratio of 5, 0.375 m chord) was tested with Gurney flap size of 1.25% and 5% chord, which employed a NACA5414 airfoil section. Comparing the lift characteristics from tests showed the increase in lift coefficient as the

Gurney flap size increased. According to Roesch,⁵⁷ the 5% chord flap increased the lift coefficient by 40%, raised the lift curve slope by 6%, and shifted the angle of attack for zero lift by -6 degrees. Drag polars, on the other hand, seemed to indicate that large Gurney flap sizes caused a large increase in drag coefficient (C_D) at moderate and low C_L . In the case of the 5% chord flap at $C_L=0.5$, the drag coefficient was almost doubled. For the 1.25% chord flap considerable improvement was observed, the C_L doubled, while there was no significant drag penalty. Although the drag reduction stated by Liebeck was not seen in the Aerospatiale tests, Roesch reported general agreement between the two studies.

To closely examine the flowfield, a water tunnel study of various Gurney flap configurations was also undertaken on a NACA 0012 wing. Neuhart⁵⁸ and Pendergraft's dye flow results showed, that the Liebeck's hypothesized flowfield caused by the Gurney flap was generally correct. Neuhart, et al. stated that the effect of the Gurney flap was to increase the local camber of the trailing edge. This hypothesis was further strengthened by the results of a wind tunnel study by Sewal,⁵⁹ that looked at the effects of increasing the local trailing edge camber of a EA-6B wing. The C_L - α curve shifted upwards from the base-line, giving higher maximum lift and more negative zero lift angle of attack. Similar to the 1.25% Gurney flap, no significant drag penalty was attributed to the Gurney flap at low to moderate lift coefficients.

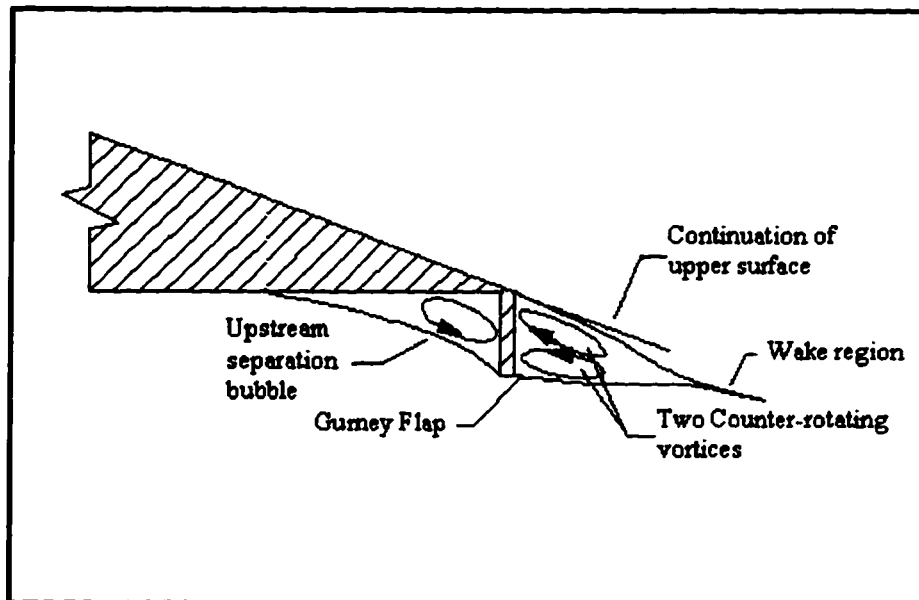


Figure 7.1. Hypothesized Trailing Edge Flow Conditions of an Airfoil with a Gurney Flap

7.2 Gurney Flap as Applied and Tested

The Gurney flap used on the S1223 in this study is shown in figure 7.2. Instead of being a simple flat plate perpendicular to the chord line, this Gurney flap is an elbow like structure positioned on the pressure side of the airfoil at the trailing edge. The dimensions of this flap are 1/8" in length and 1/64" in thickness respectively (for a 12 in. chord), making this a 1.04% chord Gurney flap. Easy to build and attach, the S1223 was wind-tunnel tested in this configuration (tested coordinates), with the results of this study compared to those experimental results (see Section 8). To capture changes in the trailing edge flow-field, due to the presence of the Gurney flap, the C-mesh shown in figs. 7.3

through 7.4 was used. Other investigators have computationally studied the NACA 4412 airfoil with a flat-plate Gurney flap, but used a coarse mesh insufficient to correctly capture the flow physics generated by the Gurney flap.⁸

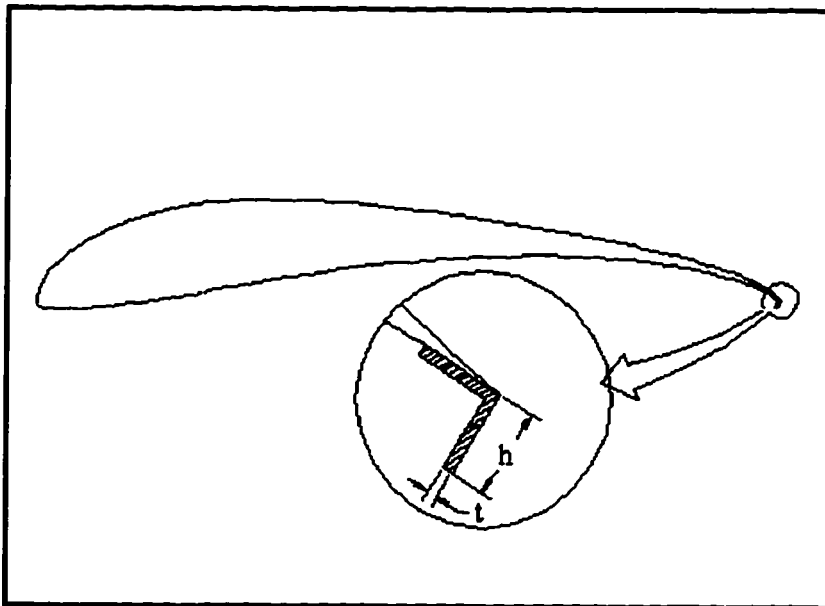


Figure 7.2. Close-up of the S1223 with a Gurney Flap ($h = 1/8''$, $t = 1/64''$, $c = 12''$)

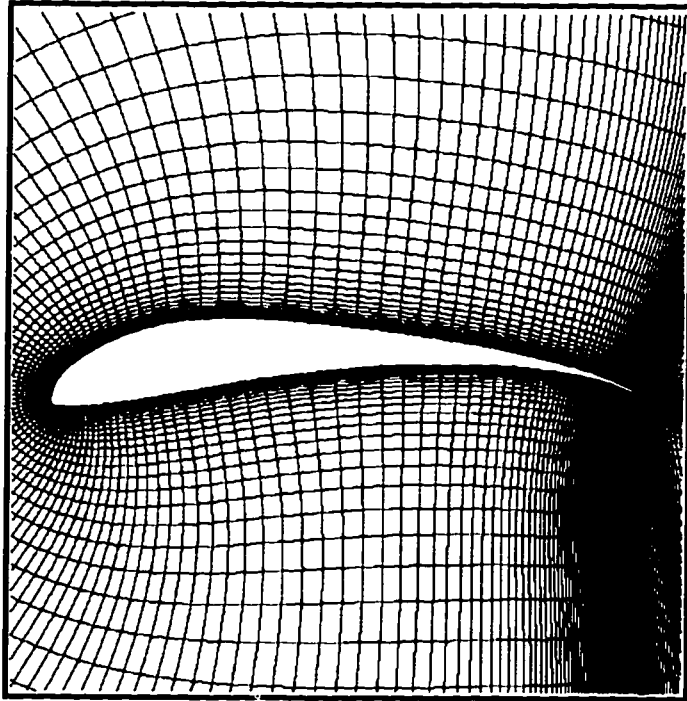


Figure 7.3. Grid Used for the Gurney Flap, (Grid No. IV: C-mesh 317x61)

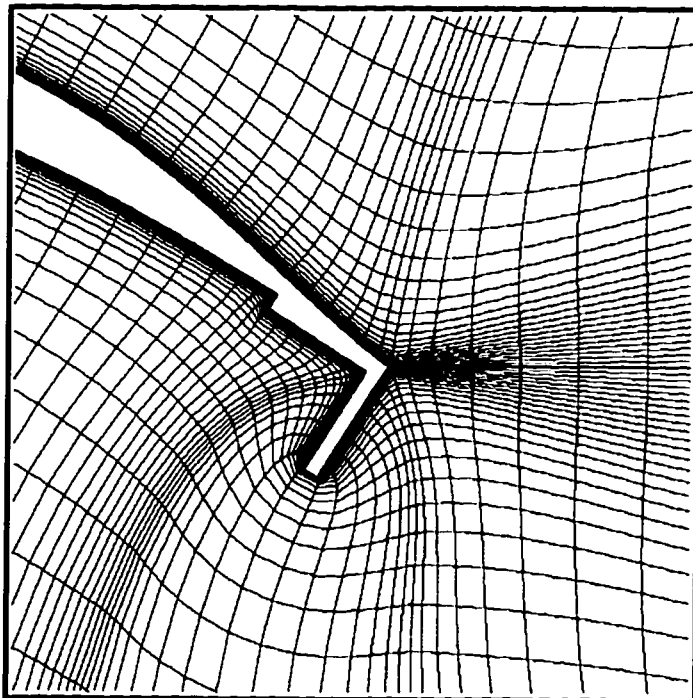


Figure 7.4. Close-up of Gurney Flap at the Trailing Edge (268 x 61) C-mesh

8. EXPERIMENTAL DATA & CORRECTIONS

This section discusses the experimental data, measurement techniques (freestream, lift and drag force), experimental set-up, data acquisition/reduction, corrections, calibration and uncertainty analyses (for complete details consult: “Summary of Low-Speed Airfoil Data, Volume-1”²). In addition, for validation purposes, experimental data is compared with data from other test facilities.

8.1 Experimental Data, Measurement Techniques

All of the experimental data used in this work comes from research conducted at the UIUC low-turbulence wind tunnel.² The wind tunnel used was an open-return type with a 7.5:1 contraction ratio. Test section was rectangular, 2.8 x 4.0 ft. in cross section and 8 ft. in length. To account for boundary layer growth along the wind tunnel side walls, the width of the cross-section was made to increase by approximately 0.5 in. Variable test section speeds up to 160 mph were made possible via 125 horsepower alternating current electric motor, connected to a five-bladed fan. For comparison purposes, the test section speed of 80 ft/sec (55 mph), corresponded to Reynolds number

of 500,000 based on the airfoil chord (see fig 8.1 for a schematic of the low-speed wind tunnel and overall dimensions).

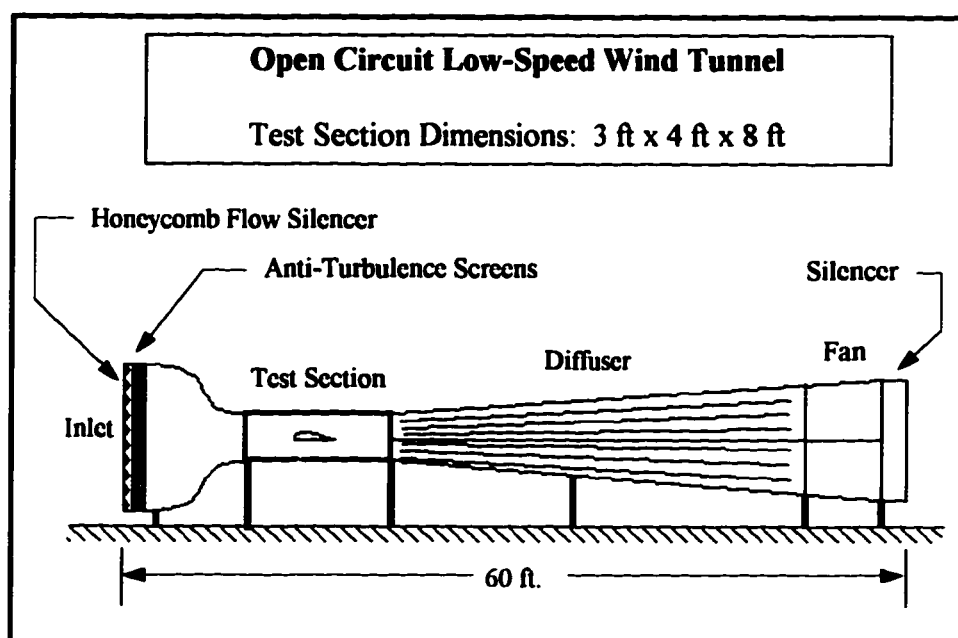


Figure 8.1. Schematic of the Low-Speed Wind Tunnel Used to Obtain Experimental Data

In retrospect, the low Reynolds number airfoil performance was found to be highly dependent on the laminar boundary layer.² In order to ensure good test section flow quality, low-turbulence levels and to avoid premature transition from laminar to turbulent flow over the airfoil surface, wind tunnel settling chamber contained a 4 in. thick honeycomb and four anti-turbulence screens. The resultant turbulence intensity has been measured to be less than 0.1%, which is said to be sufficient for low Reynolds number airfoil measurements.⁵² Mounted horizontally between two 3/8 in thick, 6 ft. long end-

plates (0.05 in gap between model), the model airfoil spanned the entire wind tunnel cross-section with nominal 12 in chord and 33 5/8 in span ($\pm 1/64$ in tolerances). Using a linear transformer on one side of the test section, the angle of attack was measured at the pivot point of the model. Other side of the airfoil model was connected to a lift carriage which was free to move vertically on a precision ground shaft (restricted from any rotation). Feedback-controlled force balance restricted the motion of the model. Velocity measurements were taken via two-axis traverser system, with two side-by-side pitot tubes, connected to a center post that extended vertically through the tunnel test section floor. The resolution and set-ability of the traverser were less than 0.001 and 0.005 in respectively in both spanwise and vertical directions. Readout accuracy in the vertical and spanwise directions were 0.002 and 0.020 in respectively.

Measurement techniques, consisted of recording analog data on an AT&T-386 computer having an analog-to-digital acquisition board. During the low speed (low Reynolds number) testing, small time-dependent fluctuations in tunnel speed existed (due to inertia of both the drive system and the air). Consequently, all of the measured quantities (total/dynamic pressure, lift, angle of attack, temperature and x-y position) were measured simultaneously by computer controlled (fully automated) acquisition system.

8.1.1 Lift & Drag Measurements

Measuring lift was accomplished with a lift balance (force transducer-servo) connected to the wind tunnel model. Similar to a standard beam balance, the weight of the airfoil and the support structure were counter-balanced with weights. The remaining forces (lift and residual imbalance) were then offset by torque, produced by a DC-torque motor mounted on the beam axis. Any angular displacement from the reference value of zero was sensed by a linear transformer. Error signal from the transformer was used to drive the torque motor until any error was removed.

Unlike the lift force, which is measured quite easily and accurately at low Reynolds numbers through a lift-balance, drag measurement is sometimes less accurate by as much as an order of magnitude.² To obtain profile drag experimentally, the momentum method of Schlichting⁶⁰ and the pitot-traverse method developed by Jones⁶¹ was used. Applying the two-dimensional momentum and continuity equations to a control volume having an upstream and downstream velocities, V_∞ and u_1 respectively, the drag force per unit span is calculated from

$$d = \int_{-\infty}^{\infty} u_1 (V_\infty - u_1) dy \quad (8.1)$$

Making the assumption that the location at which measurements are taken is located sufficiently far enough behind the airfoil, such that the static pressure has returned to upstream static pressure ($P_{s,1} = P_{s,\infty} = P_s$), with no losses associated with downstream

flow outside the airfoil wake, the total pressure can be calculated from the Bernoulli's equation

$$P_s + \frac{1}{2} \rho u_1^2 = P_{0,1} \quad (8.2)$$

$$P_s + \frac{1}{2} \rho V_\infty^2 = P_{0,\infty} \quad (8.3)$$

Applying the above two relations to eq. (8.1) and simplifying yields

$$d = \int_{-\infty}^{\infty} \left\{ \sqrt{P_{0,1} - P_s} \sqrt{q_\infty - P_s} - (P_{0,1} - P_s) \right\} dy \quad (8.4)$$

$$P_{0,1} - P_s = P_{0,1} - P_s - P_{0,\infty} + P_{0,\infty} = q_\infty - \Delta P_0 \quad (8.5)$$

The resultant drag is calculated from

$$d = \int_{-\infty}^{\infty} \sqrt{q_\infty - \Delta P_0} \left(\sqrt{q_\infty} - \sqrt{q_\infty - \Delta P_0} \right) dy \quad (8.6)$$

Wake measurements were taken 14.8 in (~1.25 chord lengths) downstream of the trailing edge of the airfoil, to ensure the wake had relaxed to tunnel static pressure. Each vertical traverse in the wake consisted of approximately 20 to 80 total head pressure measurements, with points nominally spaced 0.08 in apart. Measurements were made using a variable-capacitance differential pressure transducers (full scale range of 1 mm, resolution of 0.01% of full scale reading, and an accuracy of 0.15% of reading).

To obtain an accurate value of the drag coefficient (C_d), wake profile measurements were taken at four different spanwise locations. Detailed vertical (y-direction) surveys through the airfoil wake were nominally spaced 0.25 in apart at each spanwise location. The resulting four drag coefficients were then averaged to obtain the

C_d at a given angle of attack. Note, no measurements were taken during stall, due to the size and unsteadiness of the wake.

8.2 Experimental Data Corrections, Data Reduction

The presence of the wind-tunnel walls in a closed test section has the effect of restricting the flow producing additional forces which must be subtracted out. Extraneous aerodynamic forces occur mainly from the fact that the velocity of the air increases as it flows over the model, due to the restraining effect of the wind-tunnel boundaries combined with the presence of the model and wake.² The following presents an overview of the two-dimensional wind tunnel correction presented in Selig² (more detailed discussion can be found in Giguère⁶²).

8.2.1 Wind Tunnel Boundary Corrections

Presence of the tunnel walls cause an increase in the measured lift, drag and pitching moment due to an increase in velocity at the model. In a two-dimensional testing context, lateral boundaries are known to cause: 1) Buoyancy, 2) Solid Blockage, 3) Wake Blockage and 4) Streamline Curvature. Buoyancy 1), is an additional drag force that results from a decrease in the static pressure along the section due to the growth of the

boundary layer at the walls. Effect of buoyancy was taken into account directly in the corrections of the free stream velocity (this effect is usually insignificant for airfoils tested within test sections of constant area, consult Ref. 63). The physical presence of the model in the test-section is known as: 2) solid blockage, and has the effect of reducing the effective area. At a given angle of attack, velocity of the air must increase as it flows over the model, increasing all forces and moments (from Bernoulli's and continuity equations). Solid blockage is a function of the model size and dimensions of the test section and is given by the solid blockage correction factor

$$\varepsilon_{sb} = \frac{K_1 M_v}{A_a^{3/2}} \quad (8.7)$$

where K_1 is a constant, M_v the model volume and A_a is the test section area. Another type of blockage is known as: 3) wake blockage; and results from a lower velocity within the airfoil wake compared to velocity in the freestream. To satisfy the continuity equation in a closed test section, velocity at the model (outside of wake) must increase. The effect of wake blockage is proportional to the wake size and thus to the measured drag force on the model. The wake blockage correction factor is as follows,

$$\varepsilon_{wb} = \left(\frac{c}{2h_{ts}} \right) C_{du} \quad (8.8)$$

where the c is the airfoil chord, h_{ts} and C_{du} are the test section height and the uncorrected drag coefficient respectively. The last correction is: 4) streamline curvature and is due to the physical constraints of the tunnel boundaries. The normal curvature of the free air as it

passes over a lifting body is altered, increasing the airfoil effective camber as the streamlines are “squeezed” together. In a closed wind-tunnel sections, the increase in camber results in an increase in lift, the pitching moment (about the quarter-chord) and angle of attack, while the drag remains unaffected. Change in the lift coefficient due to streamline curvature is

$$\Delta C_{lsc} = \sigma C_l \quad (8.9)$$

where C_l is the airfoil lift coefficient and σ the wind tunnel correction parameter. Change in the angle of attack due to streamline curvature is given by the relation

$$\Delta \alpha_{sc} = \frac{57.3\sigma}{2\pi} (C_l + 4C_{m,c/4}) \quad (8.10)$$

where

$$\sigma = \frac{\pi^2}{48} \left(\frac{c}{h_{ts}} \right)^2 \quad (8.11)$$

8.2.2 Corrections to Measured Quantities

Corrections that must be applied to measured quantities can be subdivided into two categories, namely stream and model quantities. The most important stream quantity is the velocity at the model. Velocity at the model was attained from the freestream velocity measurements, by applying pertinent corrections to account for solid and wake

blockages as well as the boundary-layer growth. Combining velocity corrections into a single expression yields:

$$V_c = V_u K_{vel} (1 + \varepsilon_{sb} + \varepsilon_{wb}), \quad (8.12)$$

where, V_u is the uncorrected velocity and K_{vel} is a ratio of upstream to the model quarter chord velocities. Other stream quantities, such as the dynamic pressure and the Reynolds number were obtained using the value of the corrected velocity (V_c).

The model quantities of interest include lift, drag and angle of attack; they were corrected in their non-dimensional form to account for both solid and wake blockage as well as streamline curvature. Corrected expressions for the lift (C_l), drag (C_d) coefficients and the angle of attack (α) are as follows:

$$C_l = C_{lu} \frac{1 - \sigma}{(1 + \varepsilon_b)^2} \quad (8.13)$$

$$C_d = C_{du} \frac{1 - \varepsilon_{sb}}{(1 + \varepsilon_b)^2} \quad (8.14)$$

$$\alpha = \alpha_u - \frac{57.3\sigma}{2\pi} (C_l + 4C_{m,c/4}) \quad (8.15)$$

It is important to note, that the drag coefficient data was necessary to correct the model quantities, since the wake blockage is directly proportional to the measured drag coefficient. In the case of measuring lift however, drag was not measured, which had an effect on the lift data reduction. For the lift curves, the wake blockage correction factor (ε_{wb}) was computed using a constant value of the drag coefficient of 0.04, which was

representative for conditions of maximum lift. Although over-correcting the lift coefficient in the linear lift-curve region, this method ensured more accurate values for the maximum C_l . By comparing lift and drag data from separate lift and drag runs, this “over-correction” was found to be insignificant.

8.3 Calibrations & Uncertainty of Experimental Data

The uncertainty analysis in the current work was obtained using the method of Coleman & Steele⁶⁴ and presented by Selig.² Uncertainties in the velocity, lift and drag coefficients were found in a straight forward manner; further details can be found in Guglielmo.⁶⁵

In the case of measuring the upstream velocity, the highest uncertainty in the pressure reading was 1% and was due to fluctuations in flow angle; this resulted in a freestream-velocity uncertainty within 0.5%. Neglecting errors related to use of pressure probes, the uncertainty in the pressure readings and velocity measurements were reduced to less than 0.5% and 0.3% respectively. For lift measurements, the overall uncertainty in the lift coefficient is estimated to be 1.5%, with the inaccuracy of the lift-balance calibrations being the main contributor to this small error. Drag measurement error was found to come from three sources: i) accuracy of the data-acquisition instruments; ii) repeatability of the measurements; and iii) the selection of one of four drag profiles used to

determine the drag coefficient. Partially based on the error analysis of McGhee⁶⁶ and Coleman & Steele,⁶⁴ the uncertainty due to measurement repeatability and the instrument error were less than 1.5% and 1%, respectively. Based on statistical analysis (for a 95% confidence interval) of the spanwise drag results for the E374 airfoil at $\alpha = 4$ deg (representative of the middle range of drag polars), the uncertainties in the spanwise variations were estimated at 1.5%. Based on the calibration results of the angle of attack (taken at six different angles between 0 to 25 deg with a 5 deg increment), the overall uncertainty in the angle of attack is estimated to be 0.08 degrees.

8.3.1 Comparison to Other Test Facilities

For purposes of comparing the test facility at UIUC² and test data validation, drag results of the E387 airfoil were compared with test results performed at NASA-Langley LTPT,⁶⁶ Delft⁶⁶ and Stuttgart⁶⁷ at different Reynolds numbers. Although, the UIUC model airfoil was slightly warped/delaminated at the trailing edge, the agreement shown was quite good at Reynolds number of 2×10^5 . For the sake of completeness, wind tunnel tests on the same model were performed at Princeton,⁶⁸ again confirming good overall agreement and conforming validity of the test data.

9. DISCUSSION & COMPUTED RESULTS

This section describes and discusses the results of the current computations on the true and tested S1223 airfoils in free stream conditions at a Reynolds number of 2×10^5 . Calculated lift (C_l), drag (C_d) and moment (C_m) coefficients of the clean S1223 and 1% chord Gurney flapped airfoil are compared with the experimental data of Selig.² Pressure (C_p) and skin friction (C_f) plots, location of separation as a function of angle of attack and examples of calculated velocity profiles are presented. Results include comparison between: (a) fully turbulent and (b) laminar-to-turbulent boundary layer transition flow calculations. The turbulence models used include the one-equation *Baldwin and Barth*³ (BB), *Spalart-Allmaras*⁴ (SA) and the two-equation $k-\omega$ (SST) model.⁵ Detailed flow structures and changes in the flowfield due to the presence of the Gurney flap are presented. Numerical solution, convergence and history between turbulence models for fully-turbulent and transition flow are also included. Lastly, performance comparison is made between the “true” (having a cusp-like trailing edge, TE) and the “tested” (slightly altered finite width TE) S1223 airfoils.

9.1 Laminar to Turbulent Boundary-Layer Transition

In the present study two cases were examined: (a) flow is assumed to be fully turbulent or (b) transition from laminar to turbulent flow is assumed to occur somewhere on the airfoil top and bottom surface. For the latter to be implemented by the turbulence models (BB,SA and SST), transition points from laminar to turbulent flow had to be specified for both the upper and lower airfoil surfaces. Similar to the SA model, the BB model sets the production terms to zero upstream of the transition location. Transition usually occurs over a short, but finite distance in which the boundary layer changes intermittently from laminar to turbulent. According to Schlichting,⁶⁰ free transition occurs when a laminar boundary layer spontaneously becomes unstable, meaning that small disturbances in the flow are amplified. Once the boundary layer becomes unstable, transition to turbulence occurs some further distance downstream. As mentioned in Ref. 69, the point of instability and the following distance to the point of transition are highly dependent on the Reynolds number, the amount of turbulence in the freestream, and the external velocity distribution imposed on the boundary layer. Large Reynolds numbers, turbulence in the freestream and adverse pressure gradients all tend to hasten the transition, making the prediction of the transition difficult and inexact.⁶⁹ Schlichting states that the point of transition is generally near the point of minimum pressure (maximum edge of the boundary layer velocity V_e) for Reynolds numbers from 10^6 to 10^7 .⁶⁰

Although the exact region where transition takes place is uncertain, the assumption was made, that the minimum pressure occurs at a single point for simplicity.

A plot of the assumed location of the (minimum pressure) transition point on both the upper and lower airfoil surfaces is shown in figure 9.1. Note that the transition point location is plotted as a function of the distance (x/c) from the leading edge for the Baldwin and Barth (BB) and Spallart-Allmaras (SA) turbulence models. Transition point location is also plotted for the S1223 airfoil with a Gurney flap (GF). Transition on the upper surface shows movement toward the LE ($x/c=0$). Conversely, the minimum pressure point on the lower surface shows a trend of moving toward the TE ($x/c=1.0$), with addition of the Gurney flap causing the lower surface transition points to occur closer to the LE.

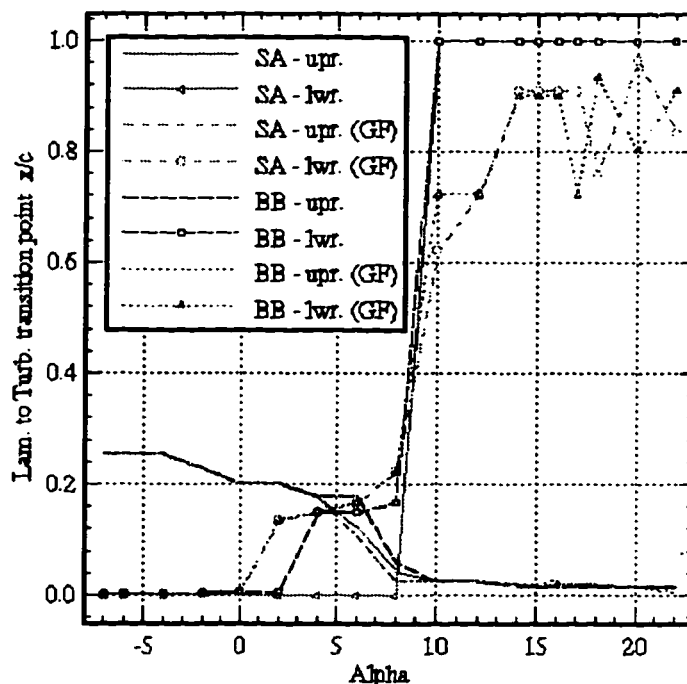


Figure 9.1. Plot of the Assumed Location of Laminar to Turbulent Transition Point.

9.2 Lift, Drag, and Moment of the S1223 Airfoil with and without a 1% Gurney Flap

Calculations were performed for the flow over the true and tested S1223 airfoils with a 1% of chord Gurney flap in free stream conditions of Reynolds number 2×10^5 . Four different C-grids having dimensions 248x61, 268x61, 301x61 and 317x61 were used respectively (for a summary see Section 6.2), with the initial spacing in the normal direction of 0.20×10^{-4} (0.002% of the chord). All of the grids were computed using a hyperbolic grid generator “HYPGEN” of Chan.⁹ In order to compute flow quantities on the computational boundary points in the “wake-cut” of the C-mesh, two lines of dummy

points were added to coincide with the points on the other side of the wake. The first line of dummy points is updated by injecting values from the coincident interior points on which they lie.⁷ Using this overlap procedure produced a smooth solution to the equations across the computational boundary in the wake of the airfoil. By the same token, dummy points are also added inside the airfoil itself, but are merely blanked out and never used in the solution procedure. Computational solution of the high lift, turbulent flow is only presented using two turbulence models, the one-equation Spalart-Allmaras (SA) and Baldwin and Barth (BB) models. The third turbulence model, the two-equation $k-\omega$ (SST) model of Menter,^{5,31,32} did not produce a satisfactory converged solution on the HP9000 computer platform (see Section 9.6 for details).

Computational results in this study are compared to experimental wind-tunnel data of Selig.² Plots of the lift (C_l), drag (C_d) and moment (C_m) coefficients, computed at angles of attack between -7 and 22 degrees are shown in figures 9.2 through 9.4. The plots show results of the SA and BB models for: (a) fully turbulent and (b) laminar and turbulent (transition) flows. Additionally, numerical solutions are presented for the S1223 airfoil having a 1% chord Gurney flap (GF). On the plot of lift coefficient versus angle of attack $C_l - \alpha$ (fig. 9.2), it is apparent that neither the BB or the SA model were able to match the experimental data exactly. Computational results seemed to agree with experimental data in only a limited range of angle of attack for both the plain and Gurney flapped airfoils.

For the plain airfoil (fully turbulent and transition cases), the BB and SA models give good results in the -1 to +1 deg. and -2 to +1 angle-of-attack range. Computational results showed the presence of a laminar separation bubble on the pressure side of the airfoil, occurring at the -2 deg for the BB and -2.78 deg. for the SA model, respectively. Attributed to a sudden drop in lift in this range, this explains the difference between the BB and SA models and the experimental data. It is not known whether a separation bubble was present in the experiments, but the wind-tunnel data seemed to indicate the bubble at -3.6 deg. Furthermore, none of the models was able to predict the zero-lift-angle-of-attack and instead showed a leveling-off trend, when approaching the zero-lift value. Outside the limited range of α where agreement is shown, both the BB and SA models over-predicted the lift coefficient considerably. Overall, the BB model was in closer agreement, with the SA model predicting even higher values of C_l . Although occurring at a lower value of α (14 deg.), both models show the dramatic loss of lift during stall, as the $C_{l_{max}}$ value is approached. For the BB and SA models (fully-turbulent/transition), a $C_{l_{max}}$ of 2.09/2.14 and 2.23/2.19 was calculated. For comparison, experiments recorded a $C_{l_{max}}$ of 2.118 occurring at 16.87 degrees angle of attack.

The only notable difference between the BB and SA models in the fully turbulent and laminar-to-turbulent transition (trx.) cases, is in the calculation of maximum lift. With virtually identical results to about $\alpha = 10$ deg (in BB and SA models), the BB model shows a higher value of maximum lift ($C_{l_{max}}$) for the transition case. Conversely, a lower value

of $C_{l_{max}}$ is shown by the SA model , with the fully turbulent boundary layer flow yielding a higher value of $C_{l_{max}}$.

Fig. 9.2 also shows how the lift coefficient increases with the addition of a 1% chord Gurney flap (GF). For the airfoil with a GF, both the BB and SA models initially agree with results for the tested GF airfoil (the difference in the BB model was again due to the occurrence of the separation bubble). The Gurney flap shifted the C_l - α curve by more than 4 or 5%, thereby increasing the $C_{l_{max}}$ (fully-turbulent/transition) from 2.09/2.14 to 2.21/2.28 (5.7/6.5 %) and 2.23/2.19 to 2.32/2.28 (4.0/4.1%) for the BB and SA models, respectively. Similar to computational results, experimental data show an increase in $C_{l_{max}}$ from 2.12 to 2.21 which amounts to 4.3 % increase in $C_{l_{max}}$. Also evident from the experimental data on the GF, the decrease in angle of attack for $C_{l_{max}}$ is shown best by the BB and SA (trx.) models. Although the numerical solutions for this low Reynolds number airfoil are not exact, they do capture significant lift benefits attributed to the Gurney flap. Overall, better initial agreement is seen for the BB model, with differences in the fully-turbulent/transition flows being very similar to airfoils without a GF.

The drag coefficient as a function of angle of attack (C_d - α) curve for the BB and SA models and with the Gurney flap is shown in fig. 9.3. Experimental data are also presented for the tested S1223 and 1% GF airfoils. Unlike the results for the lift

coefficient (C_l), closer agreement is seen for the drag coefficient (C_d). It appears that especially the BB (trx.) and BB models give the best results for the C_d , with the SA and SA (trx.) models yielding slightly lower values. Good agreement is seen up to 10 deg. especially for BB (trx.) model. Similar to the effect of the laminar-to-turbulent transition (vs. fully turbulent flow) in the C_l prediction, the BB (trx.) gives a lower value of C_d than the fully turbulent BB model case. Conversely, the SA (trx.) model predicts a slightly higher value than its fully turbulent (SA) counterpart. All of the models except the BB and BB (trx.) show an earlier (lower α) and substantial drag increase. This is mainly due to the presence of the separation bubble, which occurred further downstream for the BB and BB (trx.) models. Even though the increase in the drag coefficient with angle of attack is captured by all the models, it is evident from the experimental data that the drag is over-predicted at higher values of angle of attack.

In the drag estimation of the Gurney flap, a slight increase in the C_d is shown for both models and the experimental data. SA and SA (trx.) both predicted lower values of C_d . The BB and BB (trx.) models on the other hand, slightly overpredicted the C_d in comparison to experimental results. In distinguishing between the fully turbulent and transition cases, all model predictions seemed to agree initially with the largest discrepancies occurring at higher angle of attacks with an increase in drag due to the differences in lift. Plot of the calculated and experimental lift to drag ratio (L/D) with increasing C_l are shown in fig. 9.4, for both the plain and with a GF airfoils. In terms of

performance, the GF decreases the calculated L/D. The same kind of trend is apparent from the experimental data in the low angle of attack range. Further, experimental data show virtually no decrease in the L/D at higher values of the lift coefficient.

Figure 9.5 shows the computed moment coefficient (C_m) plotted as a function of angle of attack. No experimental results were available for this case, so comparison between the BB, BB (trx.), SA and SA (trx.) models is made solely between the calculated results. The effect of the separation bubble at lower angles of attack shows a considerable decrease in the pitching moment. Over the moderate α -range, the pitching moment gradually decreases, all the way to the point of maximum lift ($C_{l \max}$). In post-stall, the calculated rise in drag causes a subtle C_m increase. The addition of the Gurney flap increases (lowers C_m), shifting down the entire C_m - α curve.

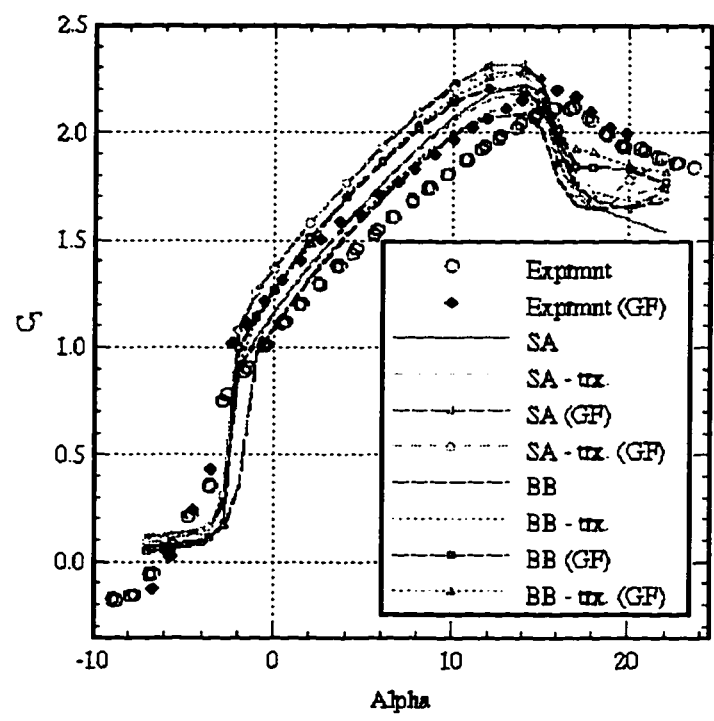


Figure 9.2. Lift Coefficient vs. Angle of Attack Plot

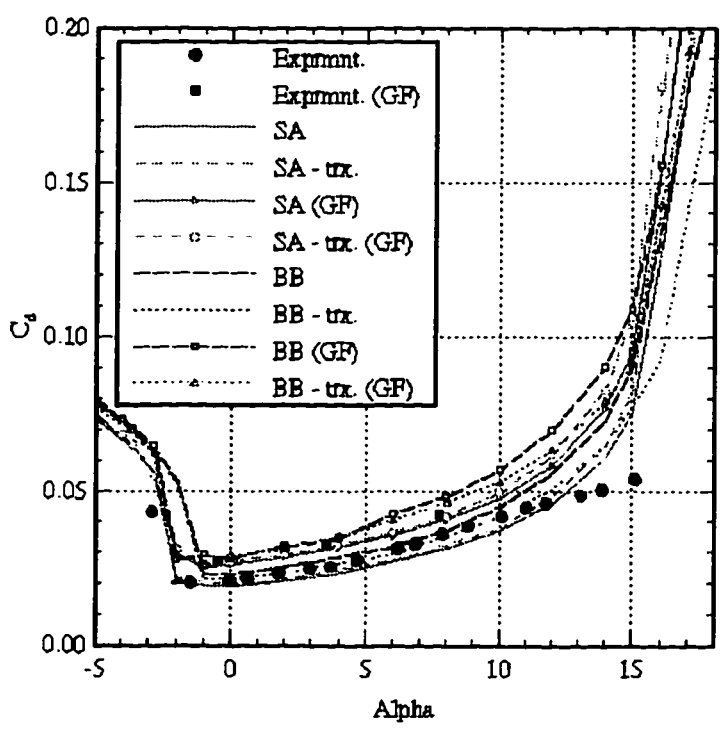


Figure 9.3. Drag Coefficient vs. Angle of Attack Plot

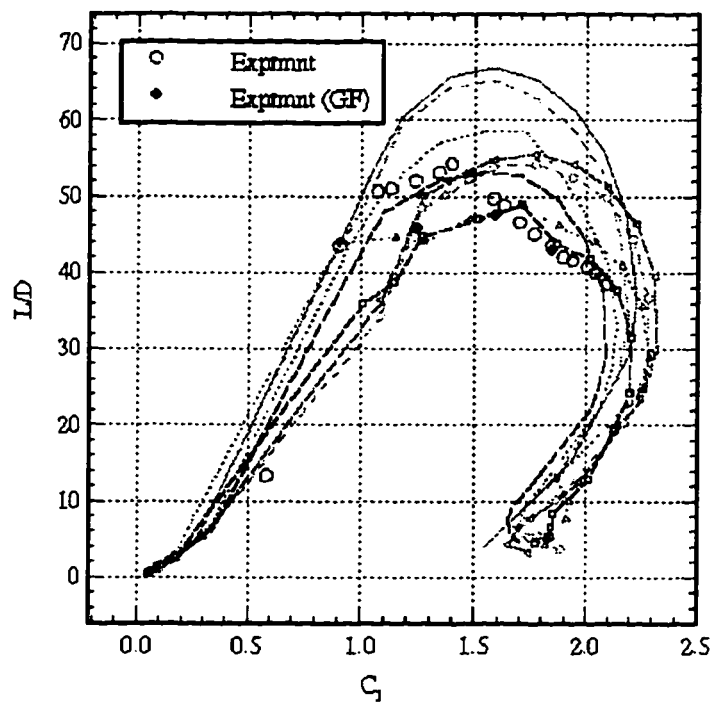


Figure 9.4 Computed L/D (Lift to Drag ratio) vs. C_l (note: legend same as in fig. 9.5)

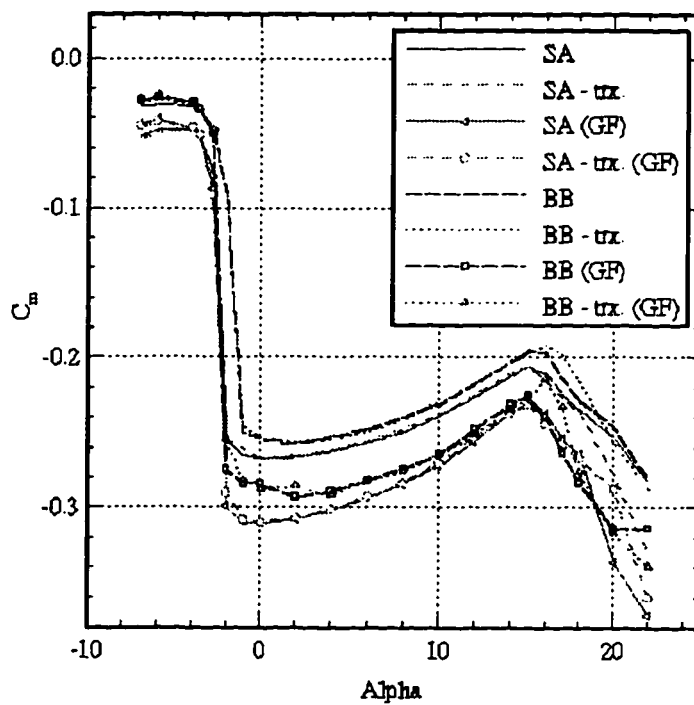


Figure 9.5 Moment Coefficient (C_m) vs. Angle of Attack Plot

9.3 Pressure, Skin-Friction, Velocity-Profiles, Separation Locations

Computational results for the pressure (C_p) and skin-friction (C_f) coefficients versus the chord-position (x/c) are plotted in figures 9.6 through 9.13, for all turbulence models (SA and BB), transition (trx.) flows and with a 1% chord Gurney flap (GF). The pressure and skin friction plots are shown for -2, 4, 8 and 14 degrees angle of attack, to cover the complete range of angles of attack of up to the maximum lift value ($C_{l_{max}}$).

As previously mentioned, computational results showed the presence of a laminar separation bubble on the pressure side of the airfoil, occurring at the -2 deg for the BB/BB (trx.) and -2.78 deg for the SA/SA(trx.) models. The effect of the bubble on the C_p and C_f at -2 deg for the BB model, can be seen in figures 9.6 and 9.10 respectively. It is evident, that the bubble increases the C_p on the suction side, but at the same time it decreases the C_p on the pressure side of the airfoil. Consequently, the decreased area between the suction and pressure side, leads to a substantial loss of lift. The concave, "Stratford-like" pressure recovery of this high lift airfoil can be observed, especially at higher values of α . The higher suction (decreased pressure) computed for the SA and SA (trx.) models in comparison to the BB and BB (trx.), provides a good explanation for the higher lift (C_l) values. At the higher angles of attack (8 and 14 deg) the effect of transition between the models can be observed. The transition SA (trx.) model shows a slightly higher C_p (more positive) than its fully turbulent SA counterpart. Conversely, the BB (trx.) exhibits a

lower (more negative) C_p than the BB model, accounting for the differences in the C_l at higher values of α .

On closer examination of the C_p versus x/c plots (figs. 9.6-9.10), the effect of adding a 1% chord GF, at the airfoil trailing edge can also be seen. For all the angles of attack shown (-2° , 4° , 8° , 14°), the presence of the GF considerably increases the aft loading on the pressure side of the airfoil. On the other hand, the C_p decreases (more negative C_p) over the entire upper surface, shifting-up the C_p - x/c curve. Compared to the plain S1223 airfoil, the pressure difference between the upper and lower airfoil surfaces is increased due to the GF, leading to increased lift and also increased pitching moment. Note that, although no experimental C_p data were available for the S1223 with a GF, increases in trailing edge loading was also observed experimentally by Jang and Bruce¹ (NACA 4412) and on an advanced airfoil by Neuhart and Pendergraft.⁵⁸ Computational results for the GF between the BB and SA models having a laminar-to-turbulent boundary layer transition, show similar trends (at higher α) as the base airfoil.

Plots of the skin friction coefficient (C_f) versus x/c (see figs. 9.11 through 9.13) show an increase in C_f for the airfoil with the GF. In addition to differences in the calculated pressure for this low Reynolds number airfoil, the C_f rise is most likely responsible for the drag increase. Note, the sudden decrease in C_f due to the GF geometry. The drag component due to friction is known to be a function of $\tau_w \sin \theta$ (where θ is measured counterclockwise for the freestream velocity vector), and is a maximum when the flow is aligned to the freestream and zero when it is perpendicular to

the free stream. The flow in the vicinity of the GF has to negotiate a sudden 90 degree turn, causing the C_f to decrease, with majority of the generated drag coming from the pressure difference ahead and behind the flap.

The effect of flow-separation on the upper surface of the airfoil is of particular interest. Figure 9.14 shows a plot of the separation location (x/c) on the suction side of the airfoil, as a function of angle-of-attack (α), for the SA/SA (trx.), BB/BB (trx.) and with a GF models. The separation location (point), was obtained by examining the calculated flowfield and checking surface-grid-point locations for signs of flow reversal. It is apparent, that the differences in lift/drag between the SA and BB models are due mainly to the separation location. For the SA/SA (trx.) models, the transition occurs considerably more aft, compared to the BB/BB (trx.) models at all values of Alpha. The delayed flow separation may help explain the differences in lift/drag between the two models. In the moderate α -range, the addition of the 1% chord GF appears to move the onset of separation slightly aft, compared to the clean airfoil case. Models having a laminar-to-turbulent boundary layer transition also show this trend.

The computed velocity profiles from the suction surface boundary layer are plotted in fig. 9.15. Velocity profiles at streamwise stations of: $x= 0.082, 0.228, 0.438, 0.613, 0.715, 0.878, 0.940$ and 0.981 are shown, using the streamwise component of velocity in boundary layer coordinates (i.e. component tangential to the local airfoil surface). Velocity profiles are plotted for the SA and BB models at the maximum lift angle of attack of 14 degrees. Even though, both the SA/SA(trx.) and BB/BB(trx.) models initially agree

(at first two stations), differences in computed u/U_{ref} velocity component is more apparent at the downstream x/c stations. As mentioned previously, the location of separation occurred farther aft ($x/c = 0.692, 0.668$) for the SA/SA (trx.) models compared to the BB/BB (trx.) models ($x/c = 0.319, 0.319$). Boundary layer growth as well as the difference in the location of separation (flow reversal) can clearly be seen on the velocity profiles.

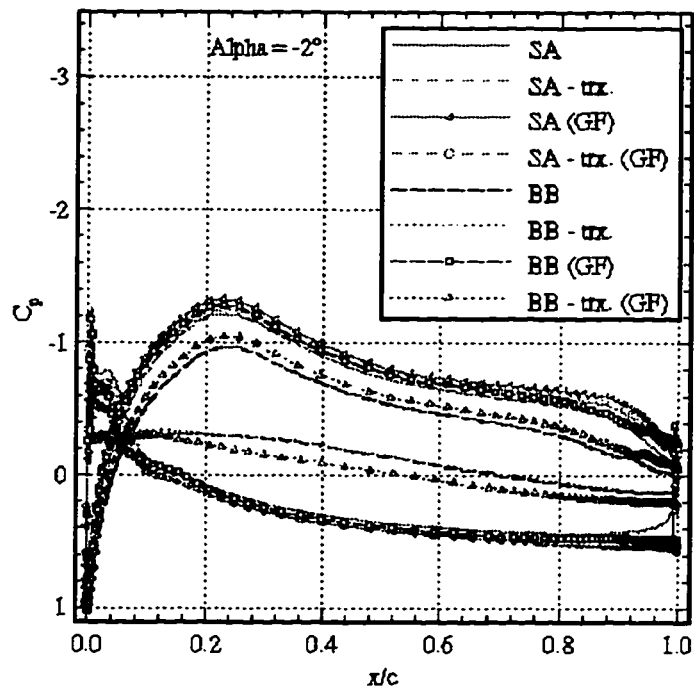


Figure 9.6. Pressure Coefficient (C_p) vs. x/c Plot ($\alpha = -2^\circ$)

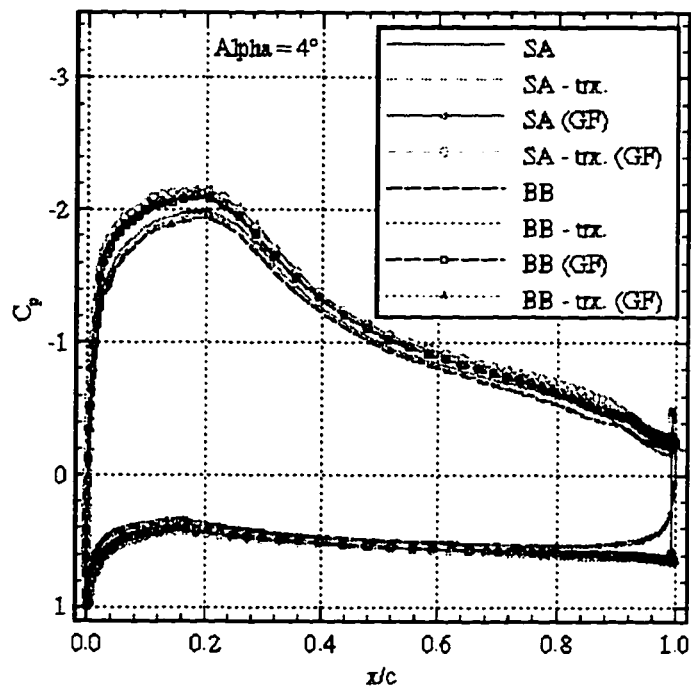


Figure 9.7. Pressure Coefficient (C_p) vs. x/c Plot ($\alpha = 4^\circ$)

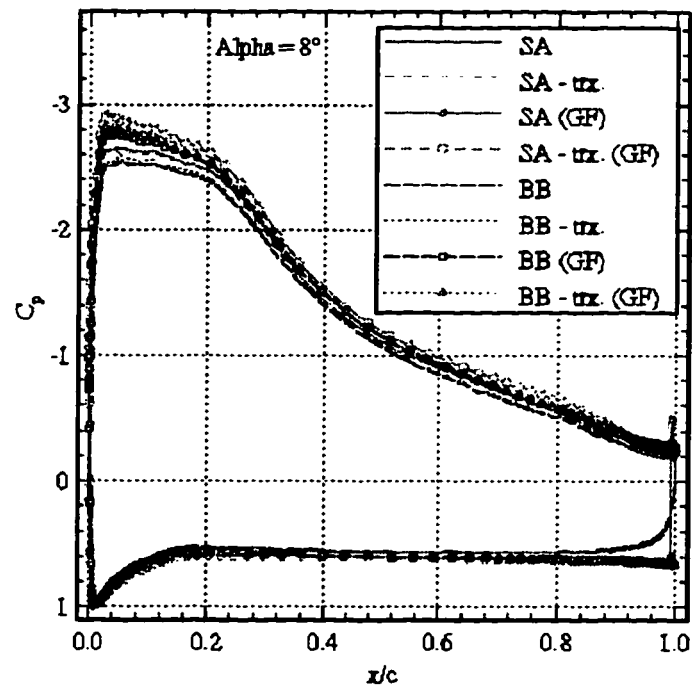


Figure 9.8. Pressure Coefficient (C_p) vs. x/c Plot ($\text{Alpha} = 8^\circ$)

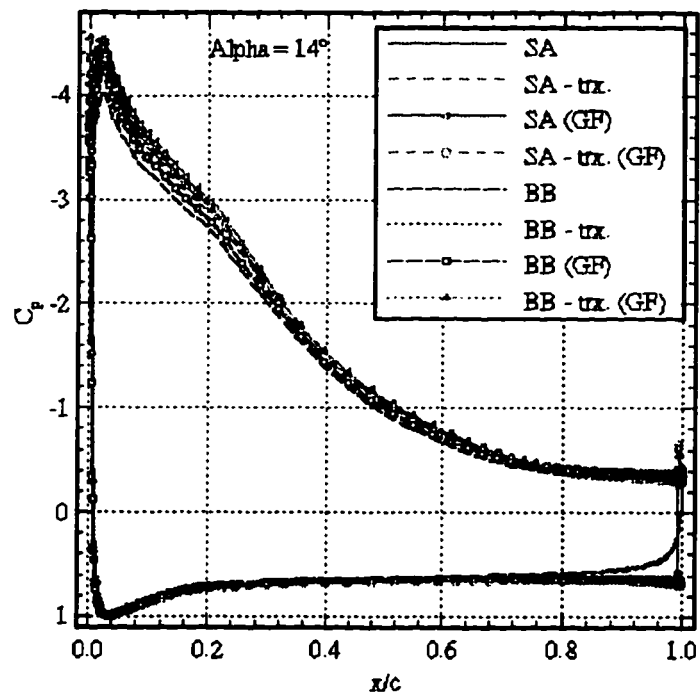


Figure 9.9. Pressure Coefficient (C_p) vs. x/c Plot ($\text{Alpha} = 14^\circ$)

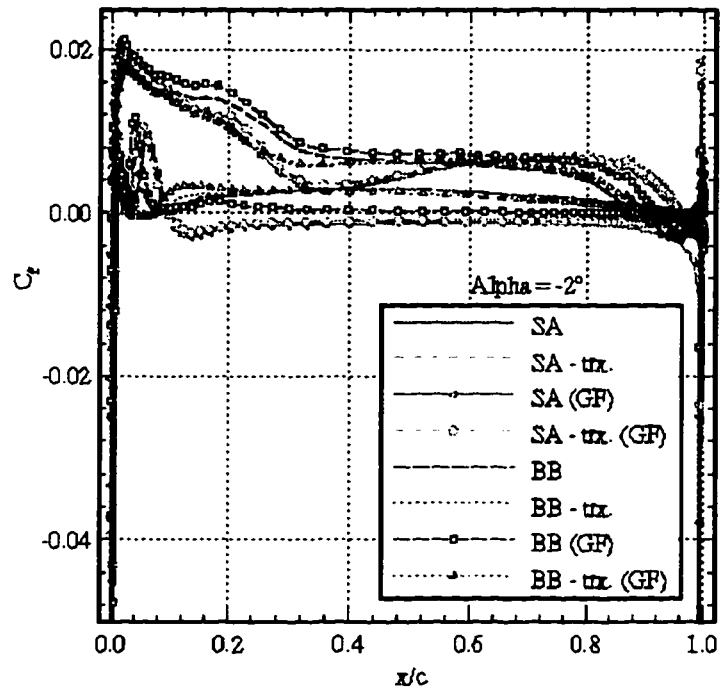


Figure 9.10. Skin-friction Coefficient (C_f) vs. x/c Plot ($\alpha = -2^\circ$)

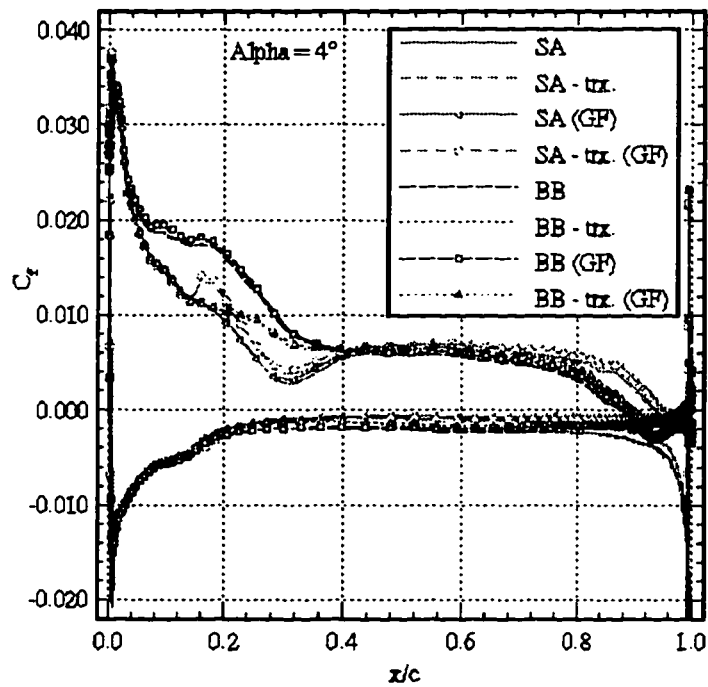


Figure 9.11. Skin-friction Coefficient (C_f) vs. x/c Plot ($\alpha = 4^\circ$)

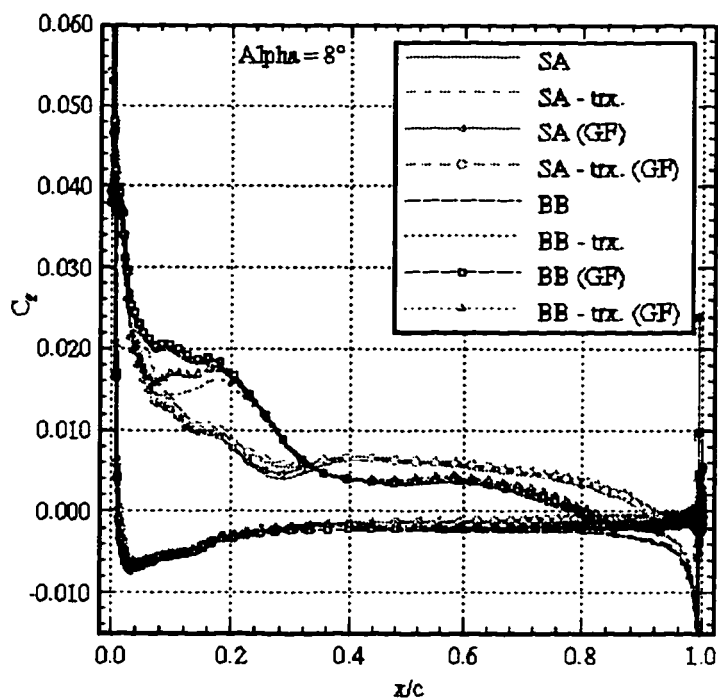


Figure 9.12. Skin-friction Coefficient (C_f) vs. x/c Plot ($\text{Alpha} = 8^\circ$)

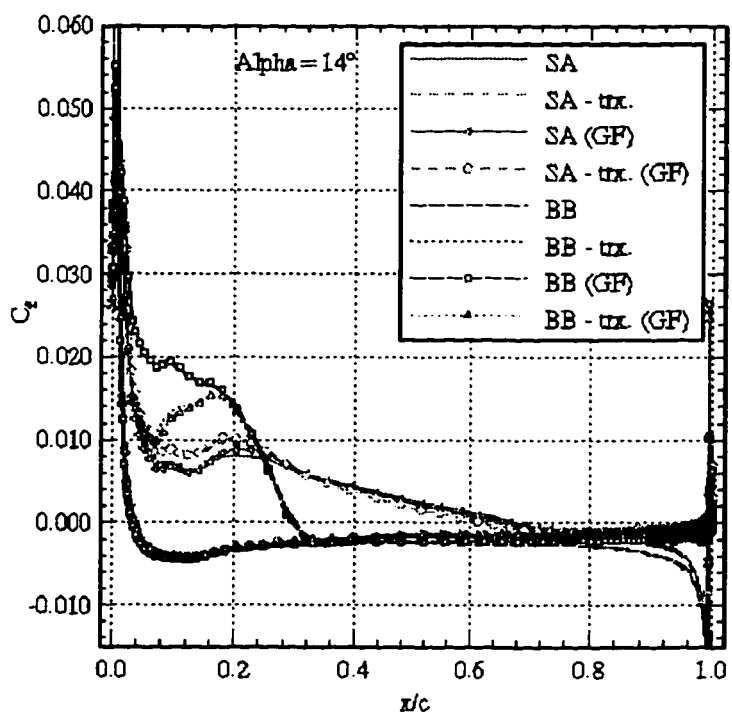


Figure 9.13. Skin-friction Coefficient (C_f) vs. x/c Plot ($\text{Alpha} = 14^\circ$)

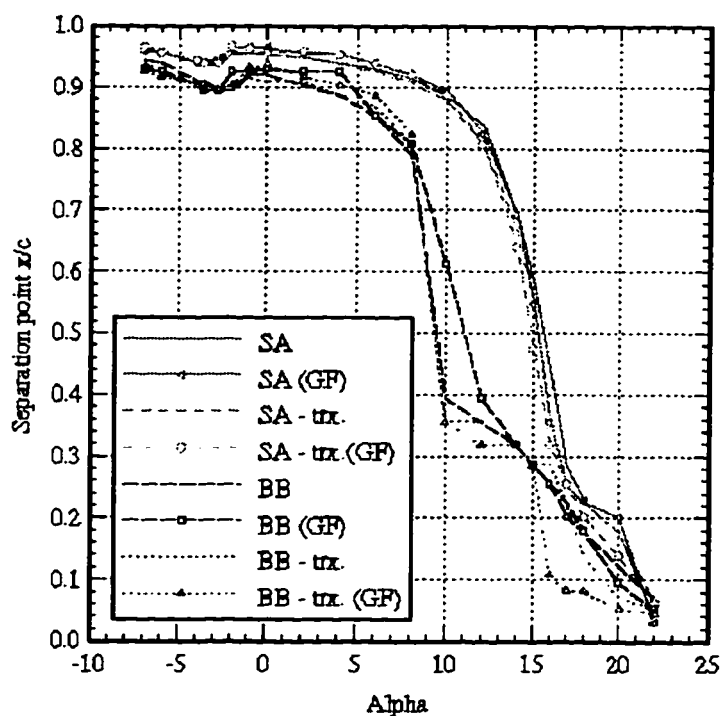


Figure 9.14. Separation Location (x/c) vs. Angle of Attack (α)

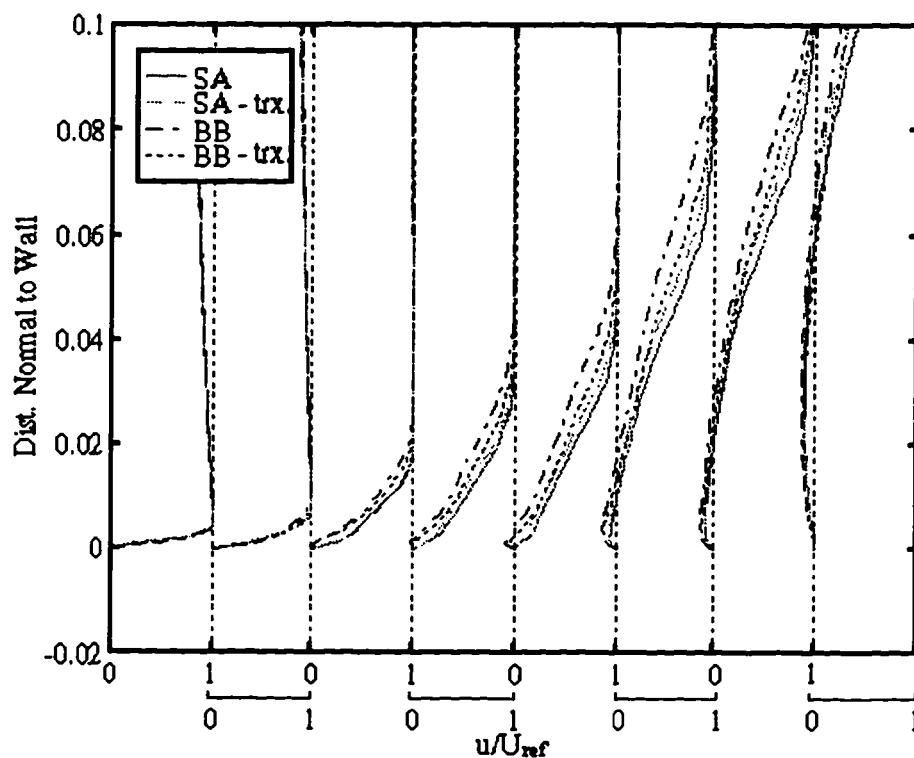


Figure 9.15. Velocity Profiles on Upper Surface of the S1223 Airfoil ($\alpha=14^\circ$) at Stations: $x/c = 0.082, 0.228, 0.438, 0.613, 0.715, 0.878, 0.940$ and 0.981 .

9.4 Detailed Flow-Structures

This section presents some detailed flow structures obtained from the computed flow field around the S1223 airfoil, using the Baldwin and Barth (BB) and Spalart-Allmaras (SA) turbulence models. Additionally, changes in the flow field due to the presence of the Gurney flap (GF) at the trailing edge are examined. Results presented include the leading edge laminar separation bubble, trailing edge flow field of the plain and with GF airfoils and flow structures at maximum lift.

As mentioned previously, calculation using both the BB and SA models have indicated flow separation at -2 and -2.78 deg. angle of attack respectively. The massive leading edge separation bubble on the pressure side of the airfoil from the BB model is shown in fig. 9.16. All plots presented include pressure contours with stream traces as well as the values of lift (C_l), drag (C_d) and pitching moment (C_m) at various angles of attack. From fig. 9.16, the leading edge laminar separation, stagnation point and the pressure distribution around the airfoil can clearly be seen. For the same conditions of $\alpha = -2$ deg., results from the SA model are shown in fig. 9.17. For this case, the flow stays attached, giving higher and lower pressures on the pressure and suction sides respectively, generating thus a much higher value of C_l (see C_p vs. x/c plot, fig. 9.6). As can be inferred from figs 9.16 and 9.17, the bubble has the effect of decreasing the pressure on the lower surface (hence the C_l), and at the same time it causes an increase in the C_d and C_m .

To closely examine changes in the flowfield due to the addition of 1% chord GF, figures 9.18 through 9.26 show results for the clean and with GF airfoils. Furthermore, to see changes in the trailing edge (TE) flowfield as a function of the angle of attack, velocity vector and stream trace (streamline) plots with pressure contours are presented for 2 and 10 deg. Examining the clean airfoil at 2 and 10 degrees angle of attack, flow separation (reversal) at the TE can be observed, with separation becoming more pronounced (moving toward the LE) with increasing α . For the airfoil with GF, two recirculation regions in front of the flap can be seen as well as the separation on the suction side of the airfoil (see close-up in fig. 9.26). Although the separation vortex at the TE for the GF flap is comparable in size, it stretches further downstream into the wake. The increase in pressure/loading at the TE due to the GF can be noticed from the pressure contours, especially for $\alpha=10$ deg. The general features of the GF flow structure illustrate only two definable regions: the counter-rotating vortex in front of the flap (not counting the small recirculation at the beginning of the flap) and the separation region on the suction side. The lack of two counter-rotating vortices on the back side of the flap contradicts the hypothesized trailing edge flow conditions of Liebeck⁵¹ (see sec. 7). The computed GF flowfield of this high-lift airfoil is considerably different than that of conventional airfoils (with the GF nearly perpendicular to free stream) reported by other authors. A computational study by Cummings⁸ on the NACA 4412 with 1.25% chord GF reported three clearly defined separation regions: i) on the suction side of the airfoil near the trailing

edge, ii) in front, and iii) behind the flap. In addition, the separation region on the suction side of the GF airfoil, was considerably smaller than on the clean airfoil.

The computed flowfield of the GF S1223 airfoil in the vicinity of the TE also shows considerable down-turning of the flow. This down-turning tendency is most likely due to a decreased pressure as the flow leaves the TE, accompanied by an increase in the downward momentum of the fluid above the TE. As a result, more of the fluid is able to overcome the adverse pressure gradient encountered at the TE.⁸ The flow turning tendency caused by the GF was also reported in water-tunnel experiments by Neuhart.⁵⁸ The separation region having approximately the same size, but moved slightly downstream, increases velocity, causing increased lift counteracting the drag produced by the GF. The positive pressure coefficient ahead of the flap and negative pressure behind it result in the net drag produced by the flap. Looking at the velocity vectors at 2 and 10 deg. angle of attack, differences in velocity profiles and deficit in the airfoil wake are clearly evident. Lastly, the airfoil at maximum lift conditions ($C_{l_{max}}=2.3$) at 14 deg. angle of attack is shown in fig 9.27. A separation region at the trailing edge can be seen, as is the flow reversal in the airfoil wake.

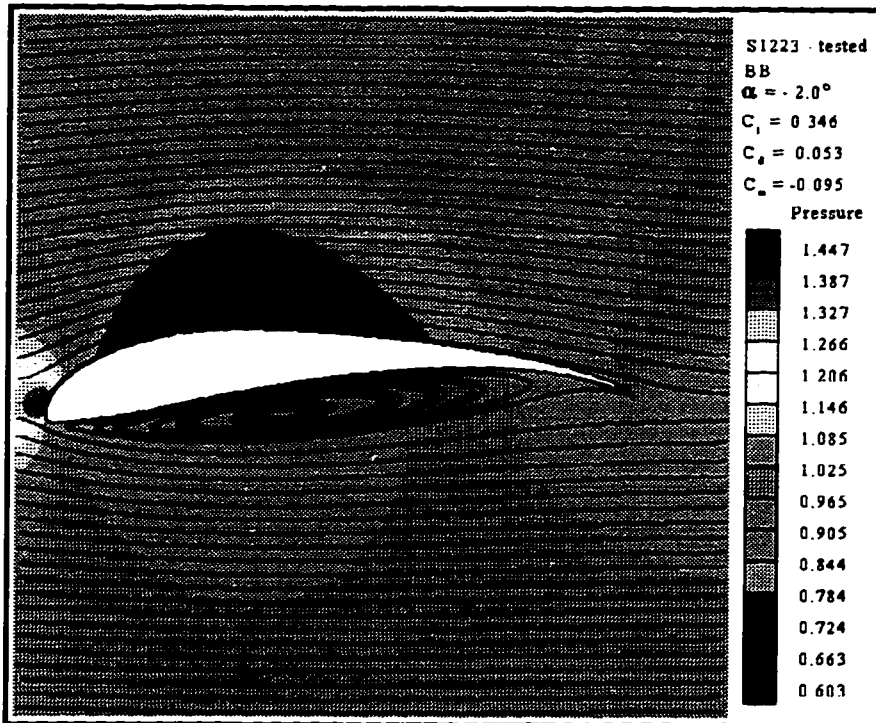


Figure 9.16. Leading Edge Separation Bubble Predicted by the BB Model ($\alpha = -2^\circ$)

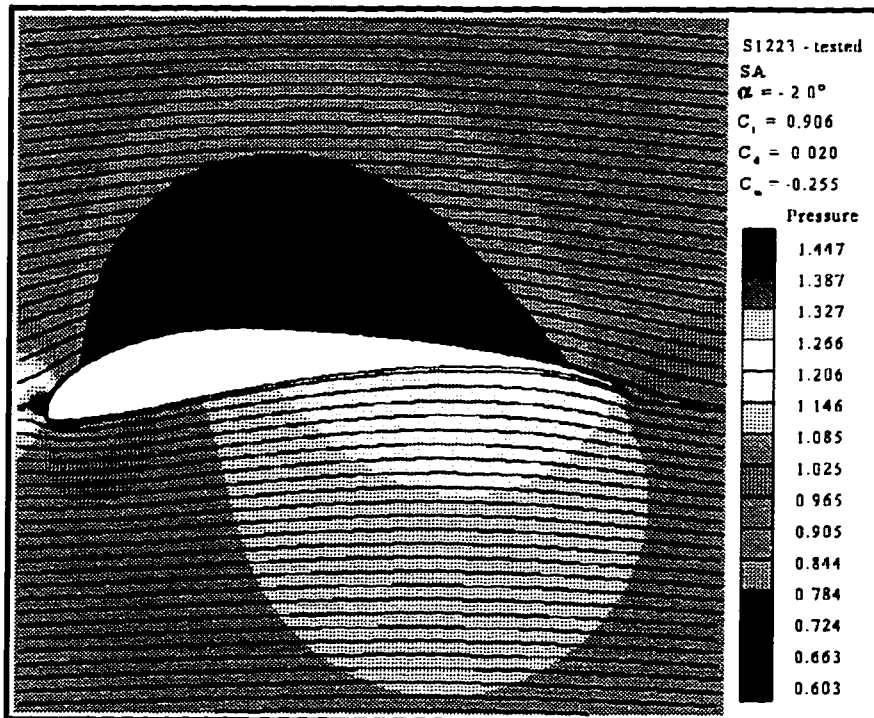


Figure 9.17. The Fully-attached Flow Predicted by the SA Model ($\alpha = -2^\circ$)

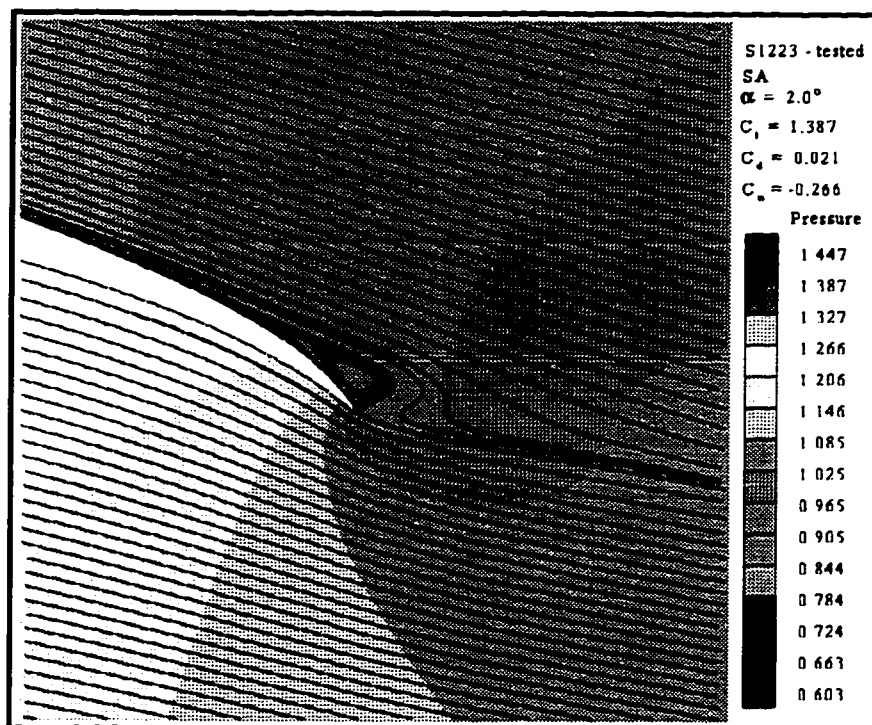


Figure 9.18. Plot of Stream Traces with Pressure Contours (plain S1223: Alpha=2°)

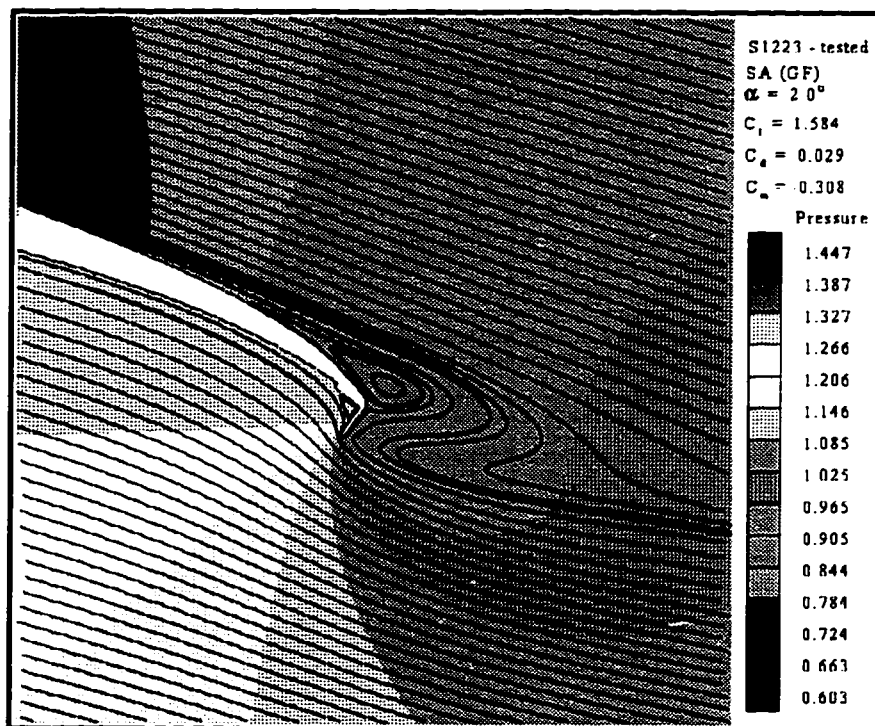


Figure 9.19. Plot of Stream Traces with Pressure Contours (S1223 w. GF: Alpha=2°)

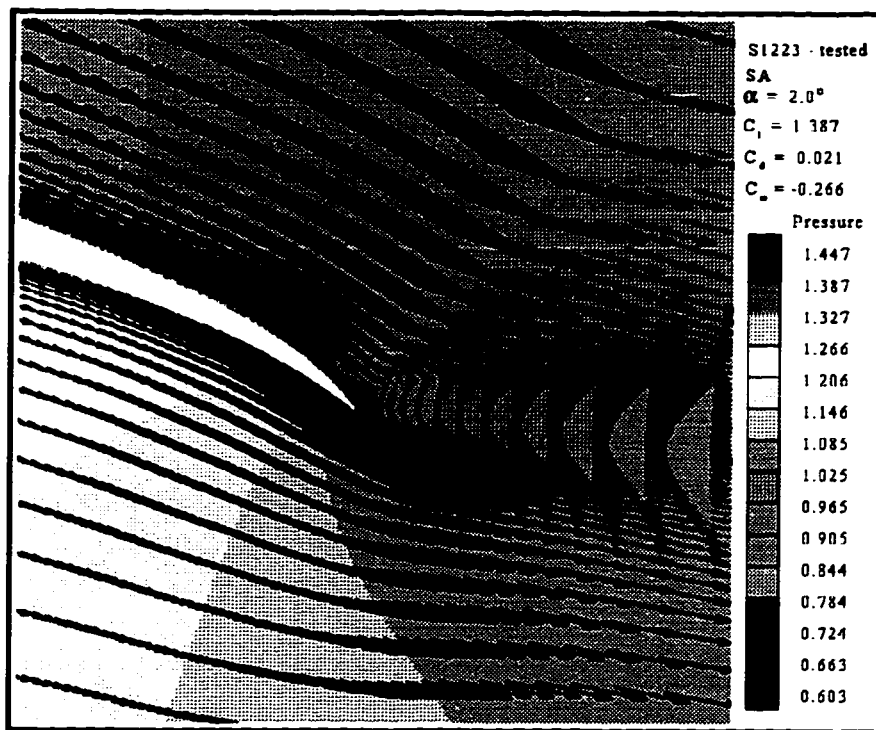


Figure 9.20. Plot of Velocity Vectors with Pressure Contours (plain S1223: Alpha=2°)

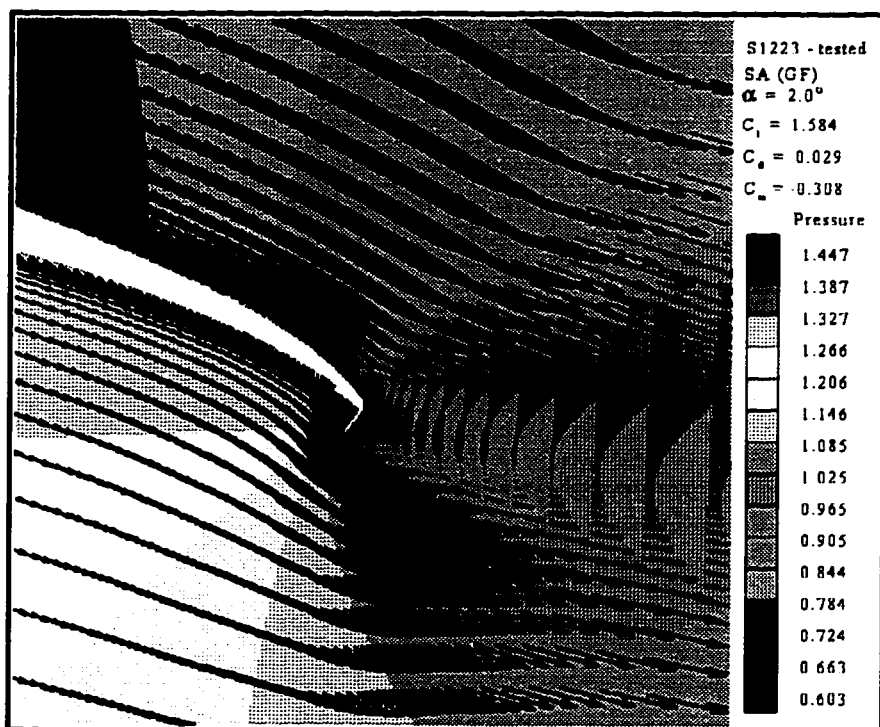


Figure 9.21. Plot of Velocity Vectors with Pressure Contours (S1223 w. GF: Alpha=2°)

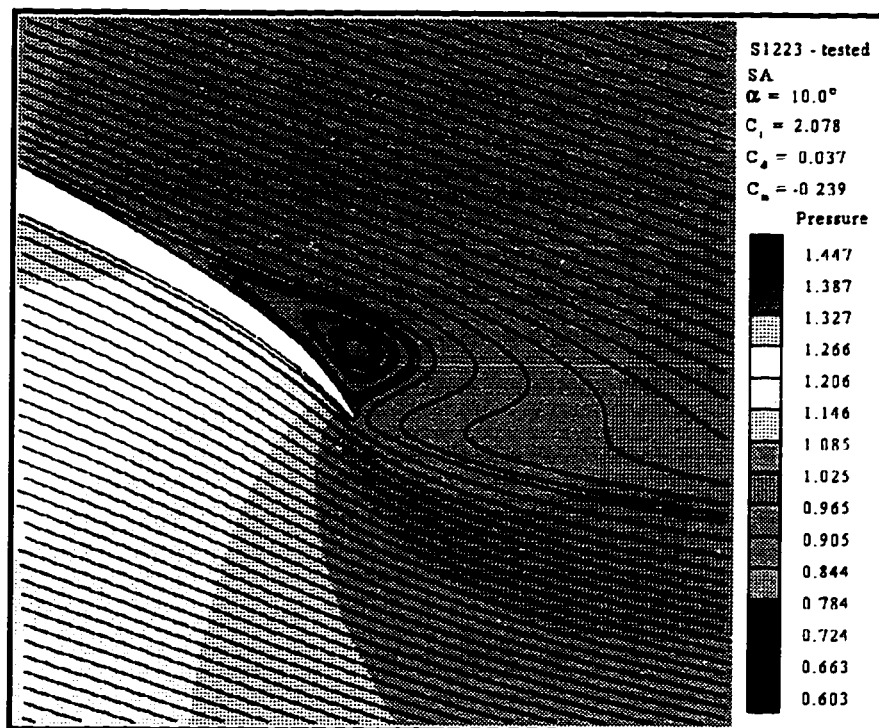


Figure 9.22. Plot of Stream Traces with Pressure Contours (plain S1223: Alpha=10°)

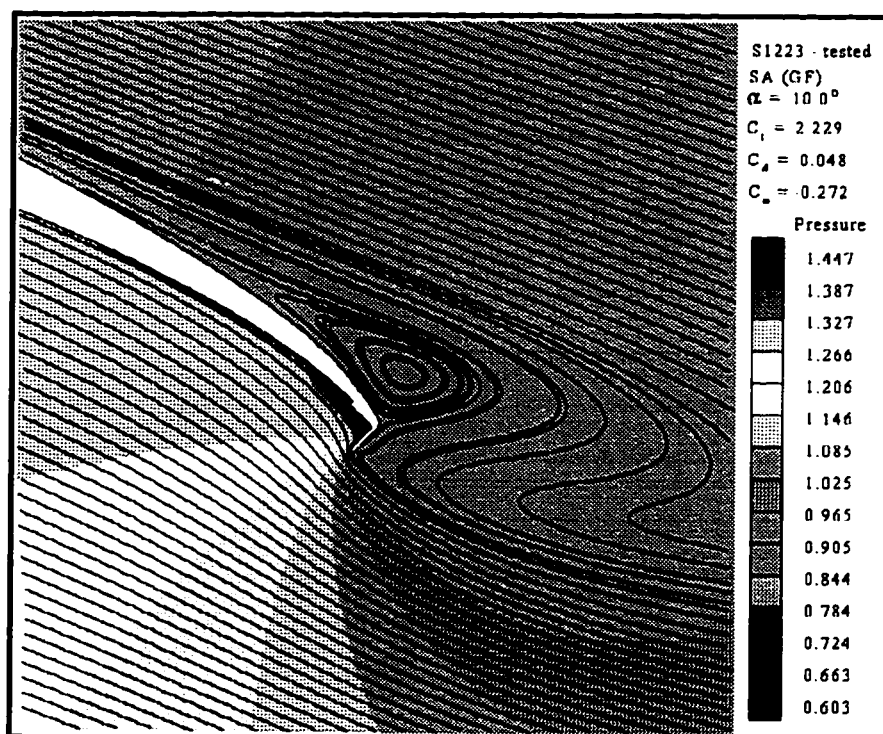


Figure 9.23. Plot of Stream Traces with Pressure Contours (S1223 w. GF: Alpha=10°)

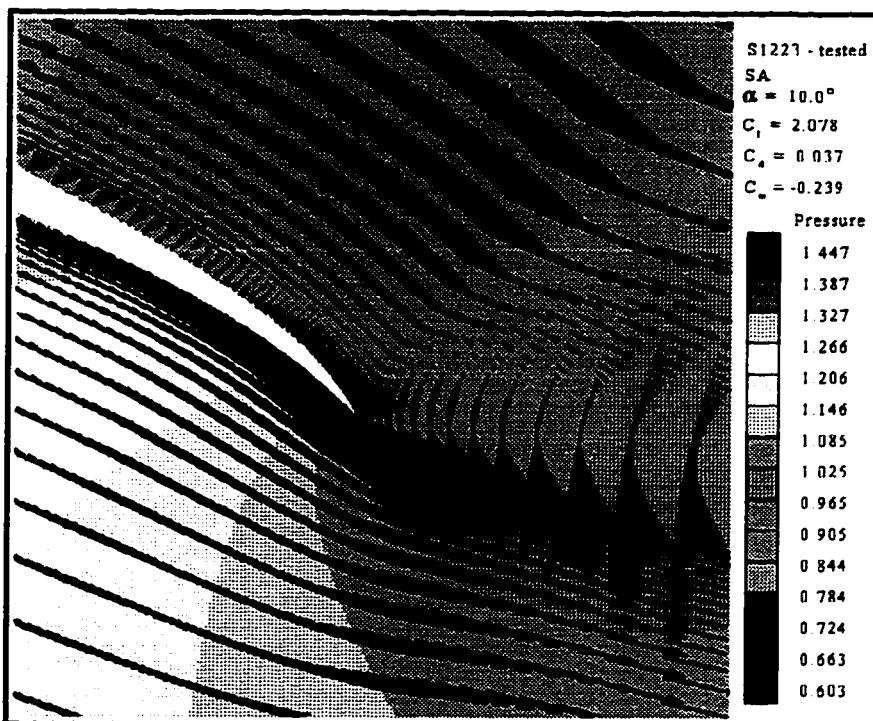


Figure 9.24. Plot of Velocity Vectors with Pressure Contours (plain S1223: Alpha=10°)

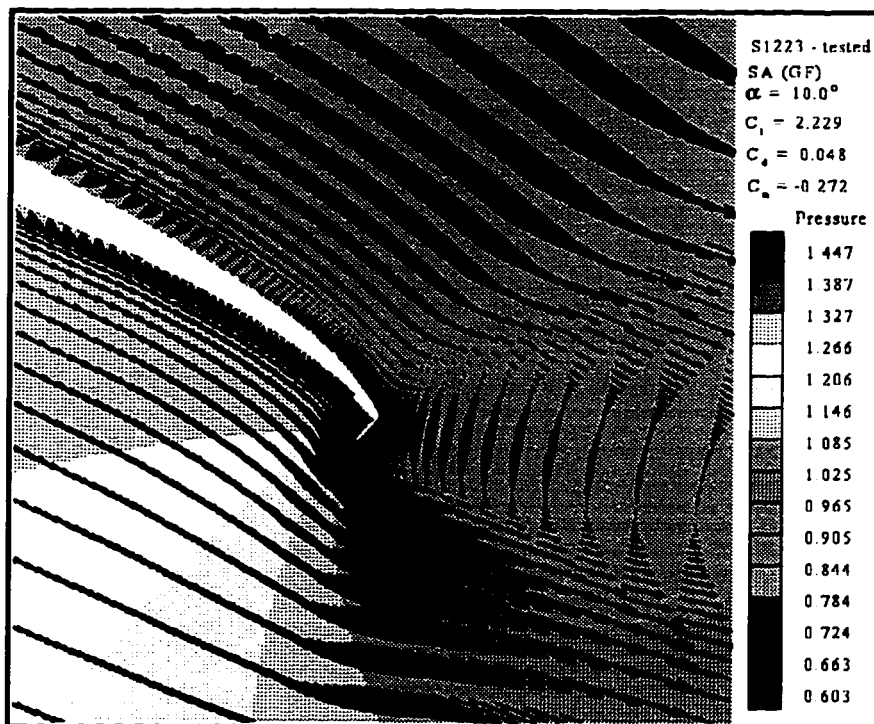


Figure 9.25. Plot of Velocity Vectors with Pres. Contours (S1223 w. GF: Alpha=10°)

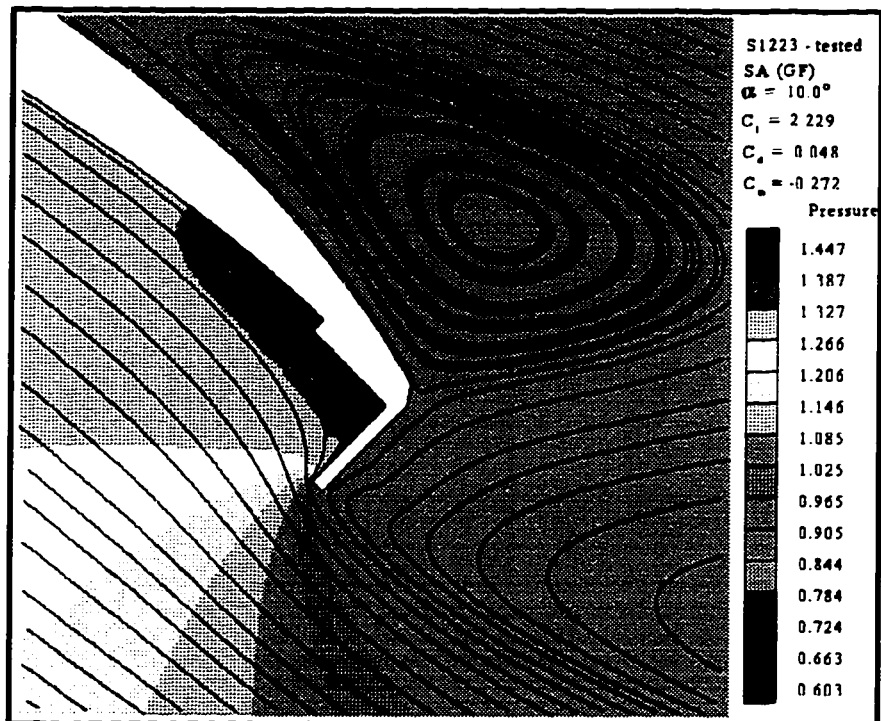


Figure 9.26. Close-up of Stream Traces with Pres. Contours (S1223 w. GF: Alpha=10°)

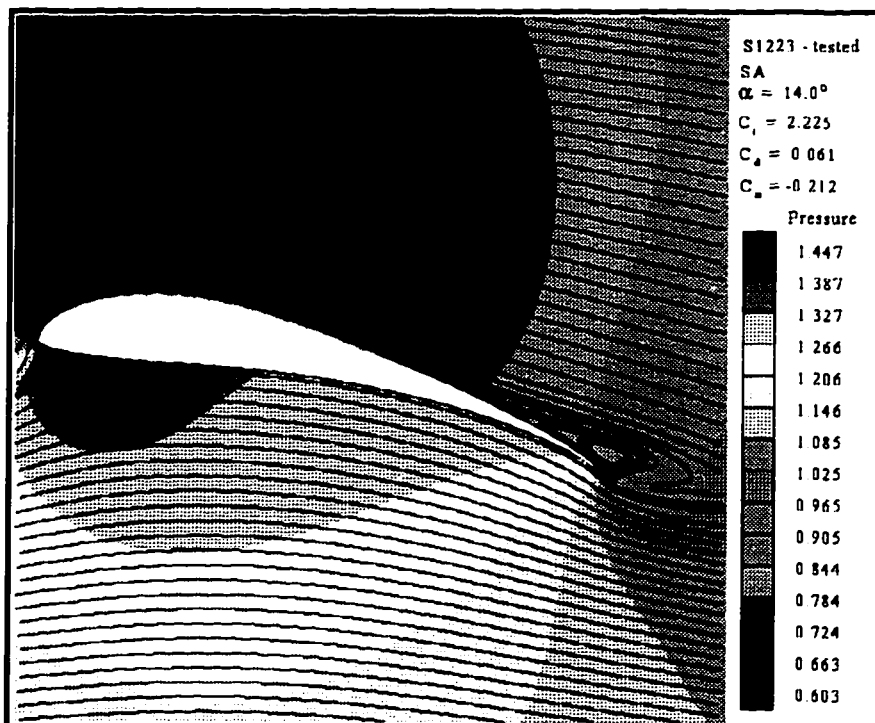


Figure 9.27. Plot of Stream Traces with Pressure Contours at Max. Lift Conditions ($C_{l_{max}}$, Alpha=14°)

9.5 Calculation Convergence History

The convergence and solution history using the incompressible Navier-Stokes equations with the pseudo-compressibility method are shown in figures 9.28 through 9.30. The results of the SA and BB models are presented for the tested clean and 1% Gurney flap (GF) S1223 airfoils at $\alpha=10^\circ$. In general, convergence was found to be highly dependent on the input parameters and choice of turbulence-model (SA or BB) as well as the computational C-grid.

As previously mentioned (Sec 6.2), elliptical smoothing was applied in the wake of the airfoil, leading to a considerable improvement in the convergence. The input parameters which had the most profound influence on convergence were: 1) β (the artificial compressibility parameter), 2) dt (time step in real-time) and 3) $d\tau$ (time step in pseudo-time). The time-step dt was in real-time during time-accurate calculations and corresponded to a time-step used by the turbulence models, during steady-state (SS) calculations. To ensure the best possible convergence, as many as twenty possible combinations of the β , dt and $d\tau$ parameters were examined. Dependent on the turbulence models and angle of attack (before or after stall), $\beta = 1, dt = d\tau = 0.1$ showed the best overall results, and were thus selected. In the case of the two-equation $k-\omega$ (SST) model, the solution diverged for all angles of attack, regardless of the choice of β , dt and $d\tau$.

This was found to be true only on the HP9000 computer platform (used in all calculations), while the SGI/CRAY computers showed excellent convergence.

Computing time and convergence varied somewhat from one turbulence model to another. Figure 9.28 shows the maximum residual of the mean flow equations, versus iteration number of the various turbulence models with and without transition. The SA/SA (trx.) showed best convergence than the BB/BB (trx.) models, with the maximum residual decreasing more quickly (even for the Gurney flap). In general, the solutions were considered converged, when the maximum residual dropped at least four-five orders of magnitude and the lift coefficient has converged to 3-4 significant digits. For steady-state calculations, good overall convergence in the lift coefficient is seen (see fig. 9.29). Conversely, the drag coefficient required as many as 1000 iterations to converge (fig. 9.30). The computing (CPU) time for the steady-state cases (single angle of attack, 301x61 C-mesh), on the HP9000 workstation was on the order of 136/137 and 132/132 minutes for the SA/SA (trx.) and BB/BB (trx.) models, respectively. For the S1223 airfoil having a 1% chord GF, the CPU time was longer, due to the flow physics and increased grid size (C-mesh size 317x61).

For all cases/models the flow tended toward unsteadiness, as the maximum lift value was approached and from the leading edge separation bubble in the low α -range. In other words for some cases, the steady state computations did not completely converge, which for the artificial compressibility formulation means that the results do not satisfy the continuity equation.⁷ In the majority of these cases, the INS2D code was then run in the

time-accurate (unsteady) mode. Especially in the post-stall angle-of-attack range, calculations showed a periodic behavior in the lift and drag. Subiterations in pseudo-time for the time-accurate calculations required many more iterations, and caused a substantial increase in CPU time.

9.6 True vs. Tested S1223 Performance Comparison

This section makes a performance comparison between the “true” S1223 (as originally designed) and the wind tunnel “tested” S1223 airfoils with and without a 1% chord Gurney flap (GF). Performance plots of the true and the tested, and the difference between the two airfoils are given in Section 6, figures 6.1 through 6.3. With an average geometry dissidence of approximately 0.0099 in. (or 0.083% for a 12 in. chord), the main difference between these two airfoils is at the trailing edge. Unlike the tested airfoil, the true S1223 has a sharp, cusp-like trailing edge. Whether or not this has any effect on the lift, drag and pitching moment is of particular interest.

The calculated lift (C_l), drag (C_d) and pitching moment (C_m) for the true, tested and with 1% GF airfoils, is shown in fig. 9.31 through 9.33 respectively. Results are again presented between -7 and 22 degrees angle of attack, for both the BB and SA models. Comparison is made between the BB and SA models, making the turbulent flow assumption throughout. From the C_l - α curve, relatively close agreement can be seen

between the airfoils, with the tested airfoil generating slightly more lift. The computed value of $C_{l_{max}}$ and angle for maximum lift ($\alpha_{l_{max}}$) are virtually identical. As can be seen for the plot at the low α -range, the laminar leading edge separation bubble was again present, accounting for the small-incremental lift with increasing α . From the plot of the drag coefficient (C_d) versus angle of attack shown in fig. 9.32, it is evident that the higher lift produced by the “tested” airfoil also produces higher drag. Differences in pitching moment about the quarter chord (C_m) between the two airfoils are shown in fig. 9.33. Both the SA and BB models predict a slightly lower nose-down pitching moment for the true airfoil. The addition of the GF on the true S1223 airfoil has almost identical effects, compared to the tested GF airfoil, in producing more lift at the expense of a moderate increase in drag. Evaluating the performance of the true and tested airfoils overall, there’s little or no benefit in having a sharp (cusp-like) trailing edge, although the lift-to-drag ratio is slightly higher for the true airfoil (fig. 9.34).

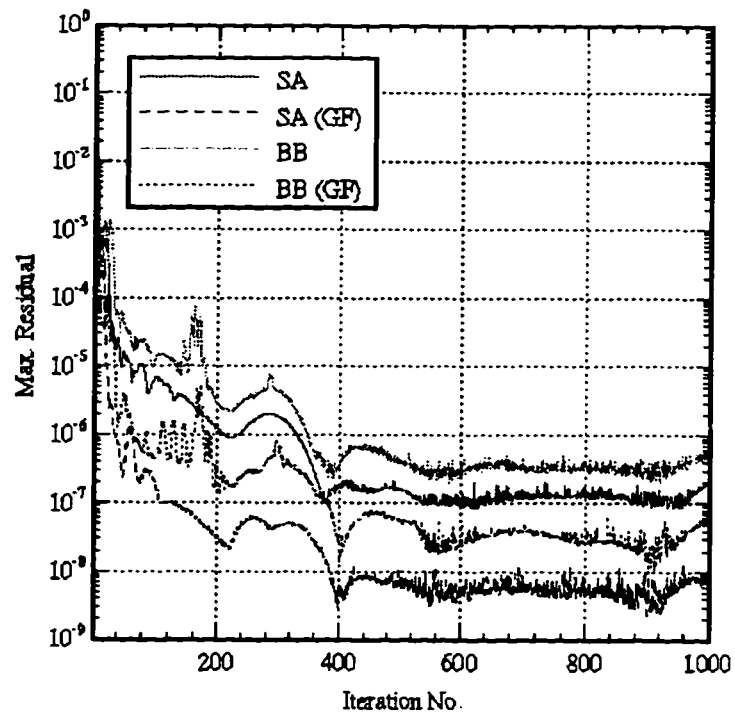


Figure 9.28. Convergence History (Alpha= 10°) Showing Maximum-Residual vs. Iteration Number

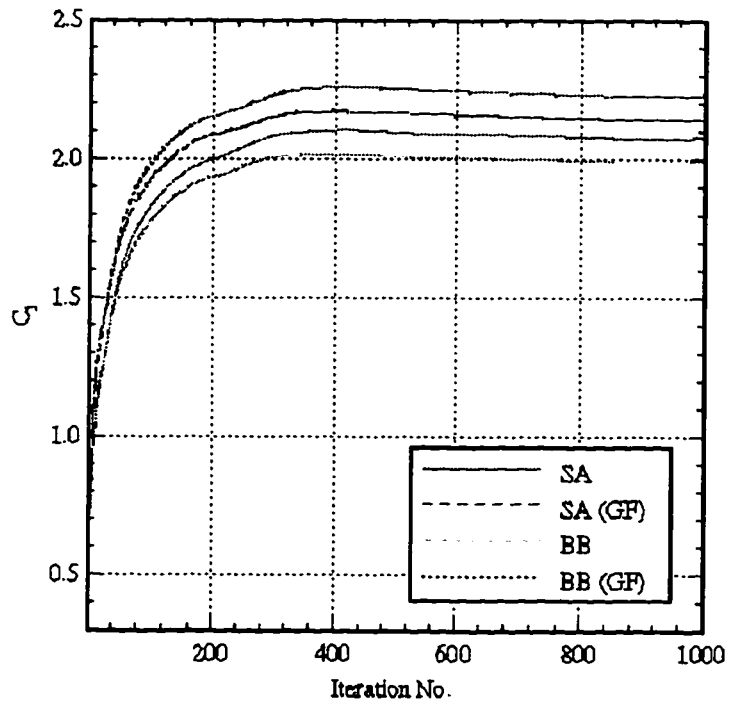


Figure 9.29. Convergence History of the C_1 vs. Iteration Number (Alpha= 10°)

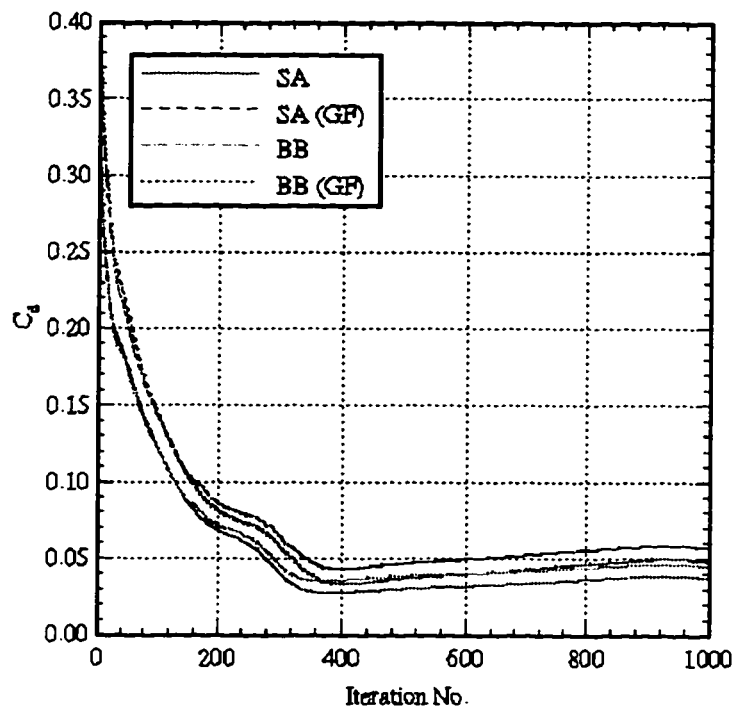


Figure 9.30. Convergence History of the C_d vs. Iteration Number ($\text{Alpha}=10^\circ$)

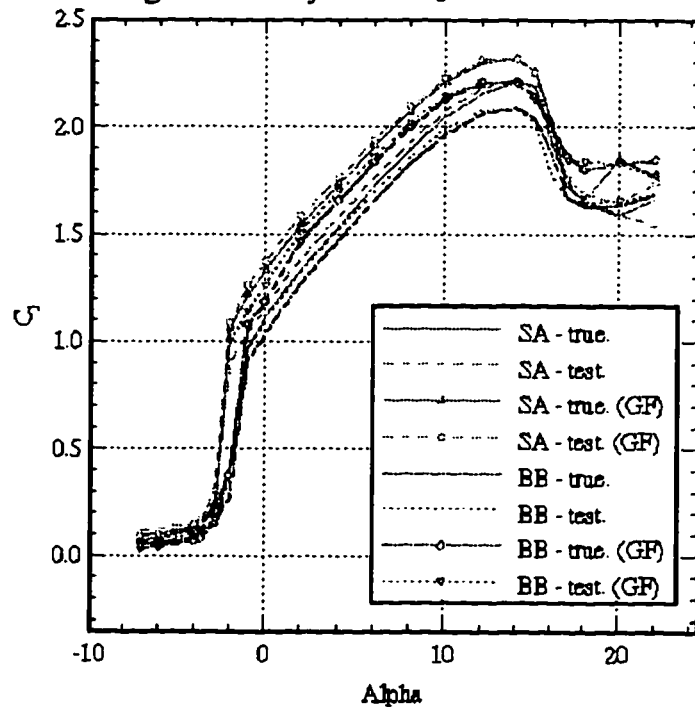


Figure 9.31. C_l - Comparison between the True and Tested S1223 Airfoils

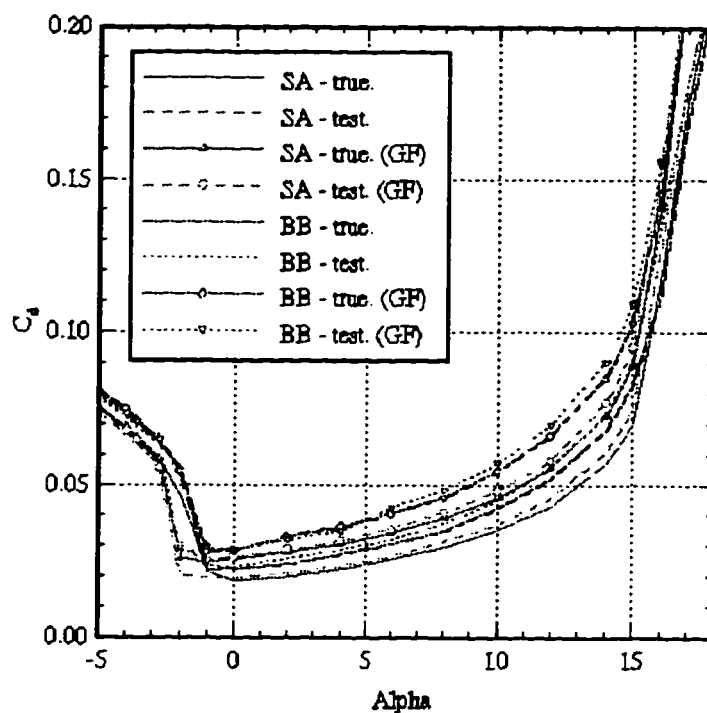


Figure 9.32. C_d - Comparison between the True and Tested S1223 Airfoils

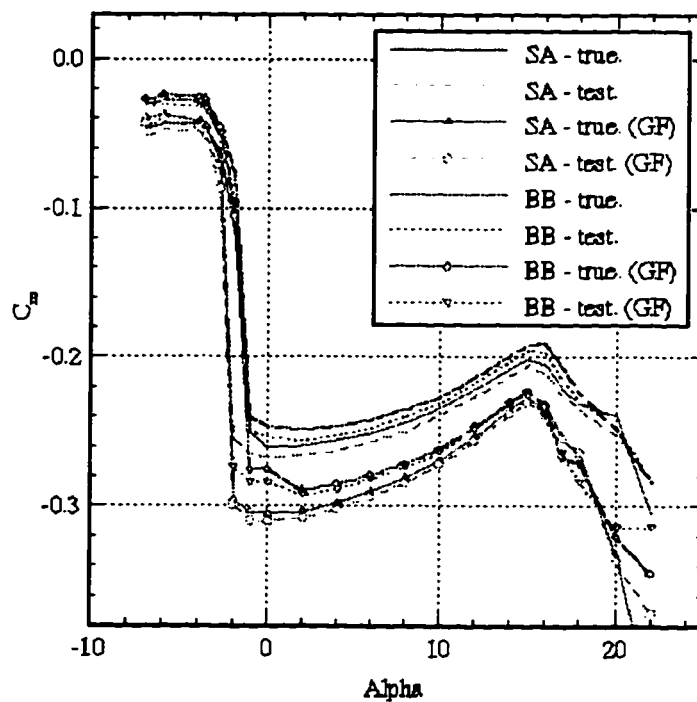


Figure 9.33. C_m - Comparison between the True and Tested S1223 Airfoils

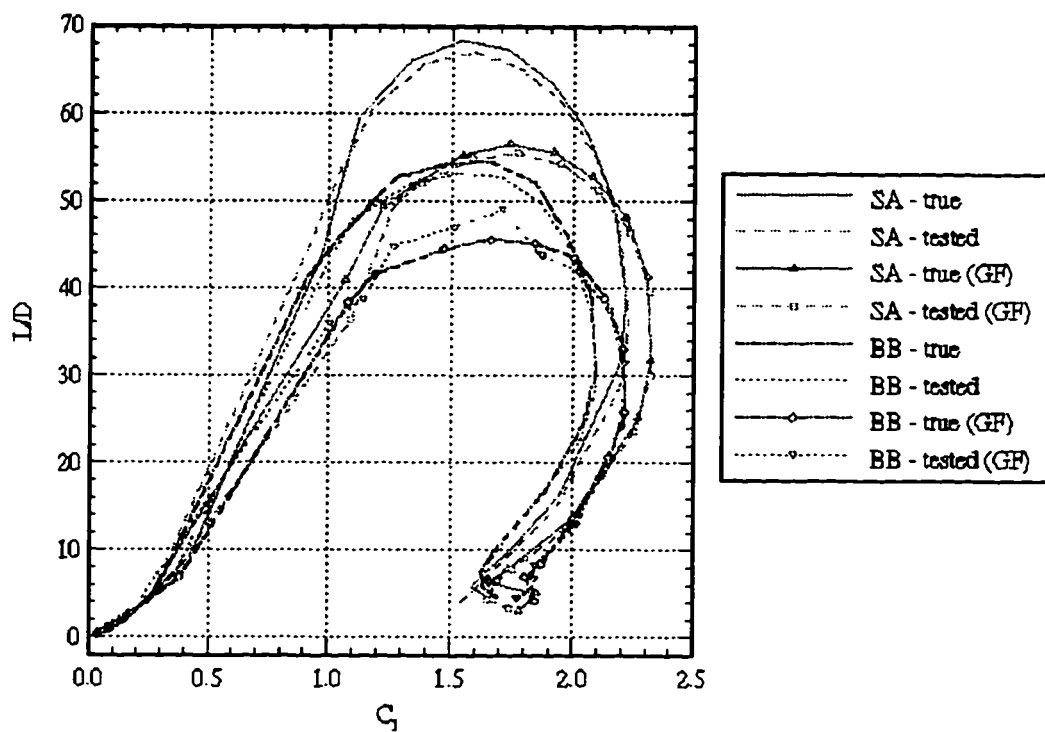


Figure 9.34. Comparison of L/D vs. C_l for the True and Tested S1223 Airfoils

9.7 Sources of Error in Computations

Based on the results obtained thus far, it is evident that none of the models provide exact agreement to experimental results. At negative angles of attack, discrepancy in the lift and drag is due to the leading edge separation bubble on the pressure side of the airfoil. Close agreement was observed only for a limited α -range (sec. 9.2) at higher angles of attack, largely due to fact that the flow is undergoing 3D effects. The 2D flow assumption no longer holds at high angles of attack and can not be considered valid. The experimental study of the airfoil with a Gurney flap measured the extent of two-dimensional flow by examining the span-variation in pressure with increasing angle of attack (Storms et al.⁵⁴). Results of this study have confirmed and the pressure distributions have indicated that the flow was essentially two-dimensional at lower angles of attack, while some three dimensionality was apparent near maximum lift. However, at angles of incidence beyond maximum lift, strong three dimensional effects were observed. By measuring chordwise (airfoil model) pressure distributions at different spanwise stations of the tunnel, three dimensional flow was indicated for the stalled condition.

Although high angle-of-attack cases include three-dimensional effects, much can be learned by studying a two-dimensional flow field, provided that the methods of solution are accurate. In the computations, the lift was computed from the calculated pressure distribution on the surface of the airfoil (area between the lower and upper C_p curves).

Similarly the drag is computed by integrating the pressure and skin friction forces on the surface. The latter method has been shown by van Dam⁷⁰ to be less accurate than other methods (such as wake integration), and may be attributed to errors in the drag. As van Dam mentions, the additional problem is the inherent numerical viscosity, which effects the surface pressure especially in the stagnation region near the leading edge and the recovery region near the trailing edge. Errors in the surface pressure calculations in these two regions, do not have much of an affect in the lift predictions, but significantly affect the drag prediction.

10. CONCLUSIONS

A numerical investigation has been completed for the low speed S1223, high lift (and with a 1% chord Gurney flap) airfoil. The two-dimensional flow was calculated by efficiently solving the incompressible Navier-Stokes (INS) equations with the INS2D code. After presenting the artificial compressibility method and the solution of the INS equations, results of the one-equation Baldwin and Barth (BB), Spalart-Allmaras (SA) and the two-equation $k-\omega$ (SST) turbulence models were compared. Results indicated good convergence for the BB and SA turbulence models. Two cases were examined: 1) flow is assumed fully turbulent and 2) transition from laminar to turbulent flow is assumed to occur on the upper and lower airfoil surfaces. The calculated velocity profiles, lift, drag, moment, pressure and skin friction coefficients were presented. Two-dimensional calculations were found to agree only in a limited range of angle of attack, when compared to experimental wind-tunnel data. The transition flow gave comparable results, to the fully turbulent case, with the main difference in the prediction of maximum lift. Both models were unable to predict the zero-lift-value and corresponding angle and overpredicted the lift with increasing angle of attack. Conversely, both models showed a precipitous decrease in lift and a large increase in drag in the stall region. Compared to experimental data, the calculated value of the maximum lift coefficient ($C_{l_{max}}$ of 2.2) was consistent, but occurred at a lower angle of attack. Differences between the BB and SA

models were found to be in the calculated location of separation, on the suction side boundary layer. Computations showed expected pitching moment trends, with increasing angle of attack. Overall, calculations of lift and drag using the one-equation BB model were in closer agreement with experimental data.

In comparison to the clean S1223 airfoil, the addition of a 1% chord Gurney flap increased the lift and pitching moment with only moderate increase in drag. The calculated pressure distribution showed a large increase in loading on the pressure side of the airfoil at the trailing edge. The increased loading (increased suction) over the entire upper surface shifted the entire C_l - α curve, and was responsible for generating the majority of the extra lift. Detailed flow structures presented changes in the flow field due to the GF. The computed GF flow field was found to be different from that of other computational studies. At moderate angles of attack, the separation point was found to move slightly farther aft over the clean airfoil case. Mechanically simple, with the potential to considerably boost the lift, and only slightly increase in drag, the Gurney flap was found to be a very intriguing device for high-lift, low-speed airfoils. Lastly, performance comparison made between the “true” (as originally designed - cusp-like trailing edge) and “tested” (slightly altered finite width trailing edge) S1223, yielded no significant differences.

REFERENCES

¹ Jang, S.C and Storms, L.B., "Lift Enhancements of an Airfoil Using a Gurney Flap and Vortex Generators," *Journal of Aircraft*, Vol. 31, No. 3, May-June 1994.

² Selig S.S, Guglielmo J.J, Broeren P.A., and Giguere P., "Summary of Low-Speed Airfoil Data, Volume-1," SoarTech Publications, Virginia, June 1995.

³ Baldwin, B. and Barth, T., "A One-Equation Turbulence Transport Model for High Reynolds Number Wall-bounded Flows," NASA TM-102847, Aug. 1990.

⁴ Spalart, P.R., and Allmaras, S.R., "A One-Equation Turbulence Model for Aerodynamic Flows," AIAA Paper 92-0439, Jan. 1992.

⁵ Menter, F. R., "Zonal Two Equations $k-\omega$ Turbulence Models for Aerodynamic Flows," AIAA Paper 93-2906, July 1993.

⁶ Rogers, S. E. , Menter, F. R., Mansour, N. N., and Durbin, P. A., "A Comparison of Turbulence Models in Computing Multi-Element Airfoil Flows", AIAA Paper 94-0291, Jan. 1994.

⁷ Rogers, S. E., Wiltberger, N. L., and Kwak, D., "Efficient Simulation of Incompressible Viscous Flow Over Single and Multi-Element Airfoils", AIAA Paper 92-0405, January 1992. Published in *AIAA Journal of Aircraft*, Vol. 30, No. 5, 1991, pp. 1385-1390.

⁸ Cummings, M.R.; Jang, S.C.; and Ross, C.J, "Computational Evaluation of an Airfoil with a Gurney Flap", AIAA Paper 92-2708-CP (92N29691), 1992.

⁹ Chan, M. W.; Chiu I-T.; Buning G. P., "User's Manual for the HYPGEN Hyperbolic Grid Generator and the HGUI Graphical User Interface," NASA TM-108791, Oct. 1993.

¹⁰ Rogers, S. E. and Kwak, D., "An Upwind Differencing Scheme for the Time Accurate Incompressible Navier-Stokes Equations", AIAA Paper 88-2583, June 1988. Published in *AIAA Journal*, Vol. 28, No. 2, Feb., 1990, pp. 253-262.

¹¹ Chorin, A. J., "Numerical Solution of the Navier-Stokes Equations," *Mathematics of Computation*, Vol. 22, No. 104, 1968, pp. 745-762.

¹² Rogers, S. E., Kwak, D., and Kiris, C., "Numerical Solution of the Incompressible Navier-Stokes Equations for Steady-State and Time-Dependent Problems", AIAA Paper 89-0463, January 1989. Also in *Proceedings of the Tenth Australasian Fluid Mechanics Conference, Melbourne, Australia, Dec. 1989*. Published in *AIAA Journal*, Vol. 29, No. 4, April 1991, pp. 603-610.

¹³ Rogers, S. E., "Numerical Solution of the Incompressible Navier-Stokes Equations", Ph.D. Thesis, Stanford University, March 1989. Also printed as NASA TM 102199, Nov. 1990. Synopsis appeared in NASA Tech. Briefs, Vol. 17, No. 6, June 1993, p. 70.

¹⁴ Anderson, A. D.; Tannehill C. J.; and Pletcher H. R.; "Computational Fluid Mechanics and Heat Transfer," Taylor & Francis, 1984, pp. 252-255.

¹⁵ Fasel, M., "Investigation of the Stability of Boundary Layers by a Finite-Difference Model of the Navier-Stokes Equations", *Journal of Fluid Mechanics*, Vol. 78, Pt.2, 1976, pp. 355-383.

¹⁶ Aziz K.; and Hellums, J. D., "Numerical Solution of the Three-Dimensional Equations of Motion of Laminar Natural Convection", *Physics of Fluids*, Vol. 10, No. 2, 1967, pp. 314-324.

¹⁷ Hafez, M.; Dacles, J.; and Soliman, M., "A Velocity/Vorticity Method for Viscous Incompressible Flow Calculations," *Proceedings of the 11th ICNMF*, Springer-Verlag, 1988.

¹⁸ Harlow, F.H.; and Welch, J.E., "Numerical Calculation of Time-Dependent Viscous Incompressible Flow of Fluid with Free Surface", *Physics of Fluids*, Vol. 8, 1965, pp. 2182-2189.

¹⁹ Kim, J.; and Moin, P., "Application of a Fractional-Step Method to Incompressible Navier-Stokes Equations", *Journal of Computational Physics*, Vol. 59, 1985, pp. 308-323.

²⁰ Rosenfeld, M.; Kwak, D.; and Vinokur, M., "A Solution Method for the Unsteady Incompressible Navier-Stokes Equations in Generalized Coordinate Systems," AIAA Paper 88-0718, 1988.

²¹ Chorin, A. J., "A Numerical Method for Solving Incompressible Viscous Flow Problems," *Journal of Computational Physics*, Vol. 2, 1967, pp. 12-26.

²² Kwak, K.; Chang, J. L. C.; Shanks, S. P.; and Chakravarthy, S. R., "A Three-Dimensional Incompressible Navier-Stokes Flow Solver Using Primitive Variables," *AIAA Journal*, Vol. 24, No. 3, 1986, pp. 390-396.

²³ Merkle, C. L.; and Athavale, M., "Time-Accurate Unsteady Incompressible Flow Algorithms Based on Artificial Compressibility," AIAA Paper 87-1137, 1987.

²⁴ Rogers, S. E., Chang, J. L. C., and Kwak, D., "A Diagonal Algorithm for the Method of Pseudocompressibility," AIAA Paper 86-1060, Atlanta, Georgia, 1986. Published in the *Journal of Computational Physics*, Vol. 73, No. 2, Dec. 1987, pp. 364-379.

²⁵ Hartwich, P. M. And Hsu, C. H., "High Resolution Upwind Schemes for the Three-Dimensional Incompressible Navier-Stokes Equations," AIAA Paper 87-0547, 1987.

²⁶ Ra, M., "Navier-Stokes Simulations of Blade-Vortex Interaction Using High-Order Accurate Upwind Schemes," AIAA Paper 87-0543, 1987.

²⁷ Barth, T. J., "Analysis of Implicit Local Linearization Techniques for Upwind and TVD Algorithms," AIAA Paper 87-0595, 1987.

²⁸ Yee, H. C., "Linearized Form of Implicit TVD Schemes For the Multidimensional Euler and Navier-Stokes Equations", *Comp. and Maths. with Appls.*, Vol. 12A, Nos. 4/5, 1986, pp. 413-432.

²⁹ Rogers, S. E., "A Comparison of Implicit Schemes for the Incompressible Navier-Stokes Equations and Artificial Compressibility", AIAA Paper 95-0567, Jan. 1995. Published in *AIAA Journal*, Vol. 33, No. 10, Oct. 1995.

³⁰ Barth, T. J., "Analysis of Implicit Local Linearization Techniques for Upwind and TVD Algorithms," AIAA Paper 87-0595, 1987.

³¹ Menter, F. R., "Performance of Popular Turbulence Models For Attached and Separated Adverse Pressure Gradient Flows," AIAA Paper 91-1784, June 1991. See also *AIAA J.*, Vol. 30, No.8, Aug. 1992, pp. 2066-2072.

³² Menter, F. R., "Influence of Freestream Values on $k-\omega$ Turbulence Model Predictions," *AIAA Journal*, Vol. 30, No. 6., June 1992, pp. 1657-1659.

³³ Meijerink, J. A. and van der Vorst., H. A., "Guidelines for the Usage of Incomplete Decompositions in Solving Sets of Linear Equations as They Occur in Practical Problems," *Journal of Computational Physics*, Vol. 44, No.1, Nov. 1981, pp. 134-155.

³⁴ Saad, Y., Schultz, M. H., "GMRES: A Generalized Minimal Residual Algorithm for Solving Nonsymmetric Linear Systems", *SIAM Journal of Scientific and Statistical Computing*, Vol. 7, No. 3, July 1995, pp. 856-869.

³⁵ Coles, D. and Wadcock, A. J., "Flying-Hot-Wire Study of Flow Past an NACA4412 Airfoil at Maximum Lift," *AIAA Journal*, Vol. 17, No. 4, Apr. 1979, pp. 321-329.

³⁶ Merkle, C. L. and Tsai, P. Y. L., "Application of Runge-Kutta Schemes to Incompressible Flow," AIAA Paper 86-0553, 1986.

³⁷ Wilcox, D. C., "Multiscale Model for Turbulent Flows," *AIAA Journal*, Vol. 26, No. 11, November 1988, pp. 1211-1320.

³⁸ Jones, W. P. and Launder, B.E., "The Calculation of Low Reynolds Number Phenomena with a Two-Equation Model of Turbulence," *Int. J. Heat Mass Transfer.*, Vol. 16, 1973, pp. 1119-1130.

³⁹ Folch, J.R. and Ailinger, K.G., "Low Reynolds Number, Long Endurance Aircraft," AIAA Paper 92-1263, Feb. 1992.

⁴⁰ Folch, J.R. and Toot, P.L., "Flight Testing Navy Low Reynolds Number (LRN) Unmanned Aircraft," *Lecture Notes in Engineering: Low Reynolds Number Aerodynamics*, T.J. Mueller (ed.), Vol. 54, Springer-Verlag, New York, June 1989.

⁴¹ Kuechmann, D., "Inviscid Shear Flow Near the Trailing Edge of an Airfoil," *Z. Flugwiss*, Vol. 15, 1967, pp.292-294.

⁴² Selig, M.S. and Maughmer, M.D., "Multipoint Inverse Airfoil Design Method Based on Conformal Mapping," *AIAA Journal*, Vol. 30, No. 5, May 1992, pp. 1162-1170.

⁴³ Selig, M.S. and Maughmer, M.D., "Generalized Multipoint Inverse Airfoil Design," *AIAA Journal*, Vol. 30, No. 11, November 1992, pp. 2618-2625.

⁴⁴ Selig, M.S., "Multipoint Inverse Design of an Infinite Cascade of Airfoils," *AIAA Journal*, Vol. 32, No. 4, April 1994, pp. 774-782.

⁴⁵ Eppler, R. and Somers, D.M., "A Computer Program for the Design and Analysis of Low-Speed Airfoils, Including Transition," NASA TM 80210, Aug. 1980.

⁴⁶ Eppler, R., *Airfoil Design and Data*, Springer-Verlag, New York, 1990.

⁴⁷ Drela , M. and Giles, M.B., "Two Dimensional Transonic Aerodynamic Design Method," AIAA Journal, Vol. 25, No. 9, Sept. 1987, pp. 1199-1206.

⁴⁸ Drela , M. and Giles, M.B., "ISES: A Two-Dimensional Viscous Aerodynamic Design and Analysis Code," AIAA Paper 870-0424, Jan. 1987.

⁴⁹ Drela M., "XFOIL: An Analysis and Design System for Low Reynolds Number Airfoils," *Lecture Notes in Engineering: Low Reynolds Number Aerodynamics*, T. J. Mueller (ed.), Vol. 54, Springer-Verlag, New York, June 1989.

⁵⁰ Chan, M. W.; Chiu I-T.; Buning G. P., "User's Manual for the HYPGEN Hyperbolic Grid Generator and the HGUI Graphical User Interface," NASA TM-108791, Oct. 1993.

⁵¹ Liebeck, R. H., "Design of Subsonic Airfoils for High Lift," *Journal of Aircraft*, Vol. 15, No. 9, Sept. 1978, pp. 547-561.

⁵² Khodadoust, A. "An Experimental Study of the Flowfield on a Semispan Rectangular Wing with a Simulated Glaze Ice Accretion," Ph.D. Thesis, University of Illinois at Urbana-Champaign, Dept. of Aeronautical and Astronautical Engineering, 1993.

⁵³ Duddy, R.R., "High Lift Devices and Their Uses", 778th Lecture to the Royal Aeronautical Society, April 1949.

⁵⁴ Jang, S.C and Storms, L.B., "Lift Enhancements of an Airfoil Using a Gurney Flap and Vortex Generators," *Journal of Aircraft*, Vol. 31, No. 3, May-June 1994.

⁵⁵ Katz, J., and Largman, R., "Effect of 90 Degree Flap on the Aerodynamics of a Two-Element Airfoil," *Journal of Fluids Engineering*, Vol 111, Mar. 1989, pp. 93-94.

⁵⁶ Katz, Joseph, and Dykstra, Lee, "Study of an Open-Wheel Racing Car's Rear-Wing Aerodynamics," SAE Paper 890600, SAE International Congress and Exposition, Detroit, MI, Feb. 27-Mar. 3, 1989.

⁵⁷ Roesch, P., and Vuillet, A., "New Designs for Improved Aerodynamic Stability on Recent Aerospatiale Helicopters", Vertica, Vol. 6, 1982, pp. 145-164.

⁵⁸ Neuhart, D.H., and Pendergraft, Jr., O.C., "A Water Tunnel Study of Gurney Flaps", NASA TM4071, 1988.

⁵⁹ Sewall, W.G., McGhee, R.J., and Ferris, J.C., "Wind-Tunnel Test Results of Airfoil Modifications for the EA-6B," AIAA Paper 87-2359, Aug. 1987.

⁶⁰ Schlichting, Hermann, "Boundary-Layer Theory," 7th Edition, McGraw-Hill, Inc., New York, 1987.

⁶¹ Jones, B.M., "The measurement of Profile Drag by the Pitot Traverse Method," Aeronautical Research Council, R&M 1688, 1936.

⁶² Giguère, P., "Two-Dimensional Wind Tunnel Boundary Layer Corrections for Low-Speed Testing in a Rectangular Test Section," University of Illinois, Report Number to be assigned, 1995.

⁶³ Rae, W.H., Jr. and Pope, A., *Low-speed Wind Tunnel Testing*, John Wiley and Sons, New York, 1984.

⁶⁴ Coleman, H.W. and Steele, W.G., Jr., *Experimentation and Uncertainty Analysis for Engineers*, John Wiley and Sons, New York, 1989.

⁶⁵ Guglielmo, J.J., "Spanwise Variations in Profile Drag for airfoils at Low Reynolds Numbers," AIAA Paper 95-1783, June 1995.

⁶⁶ McGhee, R.J., Walker, B.S. and Millard, B.F., "Experimental Results for the Eppler 387 Airfoil at Low Reynold Number in the Langley Low Turbulence Pressure Tunnel," NASA TM 4062, October 1988.

⁶⁷ Althaus, D., *Profilpolaren für den Modellflug*, Neckar-Verlag VS-Villingen, 1980.

⁶⁸ Selig, M.S., Donovan, J.F. and Fraser, D.B., *Airfoils at Low Speeds*, Soartech 8, SoarTech Publications, 1504 N. Hosreshoe Circle, Virginia Beach, VA, 23451, 1989.

⁶⁹ SoftwAeronautics, "Sub2D for Windows User's Guide, 2-D Subsonic Aerodynamic Software Ver. 1.0", Contractor/Manufacturer SoftwAeronautics, Inc., 4430 Wade Green Rd.,#9, Kennesaw, GA 30144.

⁷⁰ van Dam, C.P. and Nikfetrat, K., "Accurate Prediction of Drag Using Euler Methods," *Journal of Aircraft*, Vol. 29, No. 3, May-June 1992, pp. 516-519.

APPENDIX A. VISCOUS FLUXES

The differential formulas for the viscous fluxes in 2-D generalized coordinates are presented in this appendix (Rogers¹³). The viscous fluxes are characteristic of the following sets of conditions: nonconstant viscosity on a nonorthogonal mesh; nonconstant viscosity on an orthogonal mesh; constant viscosity on a nonorthogonal mesh and constant viscosity on an orthogonal mesh. In the equation given, the velocity gradients in the viscous fluxes are written as:

$$\frac{\partial u}{\partial \xi} = u_{\xi}, \text{ etc.}$$

and the metrics of the generalized transformation were presented with

$$\frac{\partial \xi}{\partial x} = \xi_x, \text{ etc.}$$

Nonconstant Viscosity, Nonorthogonal Mesh

$$\hat{e}_v = \frac{\nu}{J} \left[\begin{array}{l} (2\xi_x^2 + \xi_y^2)u_{\xi} + (2\xi_x \eta_x + \xi_y \eta_y)u_{\eta} + \xi_x \xi_y v_{\xi} + \xi_y \eta_x v_{\eta} \\ (\xi_x^2 + 2\xi_y^2)v_{\xi} + (\xi_x \eta_x + 2\xi_y \eta_y)v_{\eta} + \xi_x \xi_y u_{\xi} + \xi_x \eta_y u_{\eta} \end{array} \right] \quad (\text{A.1a})$$

$$\hat{f}_v = \frac{\nu}{J} \left[\begin{array}{l} (2\eta_x^2 + \eta_y^2)u_{\xi} + (2\xi_x \eta_x + \xi_y \eta_y)u_{\xi} + \xi_x \eta_y v_{\xi} + \eta_x \eta_y v_{\eta} \\ (\eta_x^2 + 2\eta_y^2)v_{\eta} + (\xi_x \eta_x + 2\xi_y \eta_y)v_{\xi} + \xi_y \eta_x u_{\xi} + \eta_x \eta_y u_{\eta} \end{array} \right] \quad (\text{A.1b})$$

Nonconstant Viscosity, Orthogonal Mesh

$$\hat{e}_v = \frac{\nu}{J} \begin{bmatrix} (2\xi_x^2 + \xi_y^2)u_\xi + \xi_x \eta_x u_\eta + \xi_x \xi_y v_\xi + \xi_y \eta_x v_\eta \\ (\xi_x^2 + 2\xi_y^2)v_\xi + \xi_y \eta_y v_\eta + \xi_x \xi_y u_\xi + \xi_x \eta_y u_\eta \end{bmatrix} \quad (\text{A.2a})$$

$$\hat{f}_v = \frac{\nu}{J} \begin{bmatrix} (2\eta_x^2 + \eta_y^2)u_\eta + \xi_x \eta_x u_\xi + \xi_x \eta_y v_\xi + \eta_x \eta_y v_\eta \\ (\eta_x^2 + 2\eta_y^2)v_\eta + \xi_y \eta_y v_\xi + \xi_y \eta_x u_\xi + \eta_x \eta_y u_\eta \end{bmatrix} \quad (\text{A.2b})$$

Constant Viscosity, Nonorthogonal Mesh

$$\hat{e}_v = \frac{\nu}{J} \begin{bmatrix} (\xi_x^2 + \xi_y^2)u_\xi + (\xi_x \eta_x + \xi_y \eta_y)u_\eta \\ (\xi_x^2 + \xi_y^2)v_\xi + (\xi_x \eta_x + \xi_y \eta_y)v_\eta \end{bmatrix} \quad (\text{A3.a})$$

$$\hat{f}_v = \frac{\nu}{J} \begin{bmatrix} (\eta_x^2 + \eta_y^2)u_\eta + (\xi_x \eta_x + \xi_y \eta_y)u_\xi \\ (\eta_x^2 + \eta_y^2)v_\eta + (\xi_x \eta_x + \xi_y \eta_y)v_\xi \end{bmatrix} \quad (\text{A3.b})$$

Constant Viscosity, Orthogonal Mesh

$$\hat{e}_v = \frac{\nu}{J} \begin{bmatrix} (\xi_x^2 + \xi_y^2)u_\xi \\ (\xi_x^2 + \xi_y^2)v_\xi \end{bmatrix} \quad (\text{A4.a})$$

$$\hat{f}_v = \frac{\nu}{J} \begin{bmatrix} (\eta_x^2 + \eta_y^2)u_\eta \\ (\eta_x^2 + \eta_y^2)v_\eta \end{bmatrix} \quad (\text{A4.b})$$

APPENDIX B. TRUE AND TESTED S1223 AIRFOIL COORDINATES

This appendix includes the true (as originally designed) and tested S1223, high lift airfoil coordinates used in the calculations (for detailed discussion consult Selig²).

| <i>Tested - S1223</i> | | | | <i>True - S1223</i> | | | |
|-----------------------|------------|------------|------------|---------------------|------------|------------|------------|
| <i>x/c</i> | <i>y/c</i> | <i>x/c</i> | <i>y/c</i> | <i>x/c</i> | <i>y/c</i> | <i>x/c</i> | <i>y/c</i> |
| 1.00000 | -0.00178 | 0.01989 | 0.04487 | 1.00000 | 0.00000 | 0.01718 | -0.01550 |
| 1.00000 | 0.00000 | 0.01503 | 0.03884 | 0.99838 | 0.00126 | 0.03006 | -0.01584 |
| 1.00000 | 0.00013 | 0.01082 | 0.03257 | 0.99417 | 0.00494 | 0.04627 | -0.01532 |
| 0.99720 | 0.00333 | 0.00706 | 0.02587 | 0.98825 | 0.01037 | 0.06561 | -0.01404 |
| 0.99187 | 0.00839 | 0.00482 | 0.02100 | 0.98075 | 0.01646 | 0.08787 | -0.01202 |
| 0.98689 | 0.01260 | 0.00221 | 0.01365 | 0.97111 | 0.02250 | 0.11282 | -0.00925 |
| 0.98075 | 0.01692 | 0.00080 | 0.00745 | 0.95884 | 0.02853 | 0.14020 | -0.00563 |
| 0.97339 | 0.02127 | 0.00019 | 0.00286 | 0.94389 | 0.03476 | 0.17006 | -0.00075 |
| 0.96293 | 0.02660 | 0.00005 | -0.00138 | 0.92639 | 0.04116 | 0.20278 | 0.00535 |
| 0.95370 | 0.03080 | 0.00083 | -0.00593 | 0.90641 | 0.04768 | 0.23840 | 0.01213 |
| 0.94176 | 0.03581 | 0.00139 | -0.00690 | 0.88406 | 0.05427 | 0.27673 | 0.01928 |
| 0.92548 | 0.04204 | 0.00312 | -0.00872 | 0.85947 | 0.06089 | 0.31750 | 0.02652 |
| 0.91053 | 0.04728 | 0.00790 | -0.01068 | 0.83277 | 0.06749 | 0.36044 | 0.03358 |
| 0.88969 | 0.05399 | 0.01449 | -0.01150 | 0.80412 | 0.07402 | 0.40519 | 0.04021 |
| 0.87178 | 0.05924 | 0.02138 | -0.01185 | 0.77369 | 0.08044 | 0.45139 | 0.04618 |
| 0.84496 | 0.06638 | 0.03330 | -0.01196 | 0.74166 | 0.08671 | 0.49860 | 0.05129 |
| 0.81744 | 0.07305 | 0.04627 | -0.01153 | 0.70823 | 0.09277 | 0.54639 | 0.05534 |
| 0.78334 | 0.08061 | 0.06389 | -0.01040 | 0.67360 | 0.09859 | 0.59428 | 0.05820 |
| 0.74802 | 0.08779 | 0.08117 | -0.00888 | 0.63798 | 0.10412 | 0.64176 | 0.05976 |
| 0.71868 | 0.09328 | 0.10354 | -0.00663 | 0.60158 | 0.10935 | 0.68832 | 0.05994 |
| 0.68153 | 0.09976 | 0.12948 | -0.00369 | 0.56465 | 0.11425 | 0.73344 | 0.05872 |
| 0.65038 | 0.10483 | 0.16404 | 0.00134 | 0.52744 | 0.11881 | 0.77660 | 0.05612 |
| 0.61072 | 0.11087 | 0.20100 | 0.00781 | 0.49025 | 0.12303 | 0.81729 | 0.05219 |
| 0.59071 | 0.11368 | 0.25115 | 0.01690 | 0.45340 | 0.12683 | 0.85500 | 0.04706 |
| 0.56407 | 0.11720 | 0.29610 | 0.02479 | 0.41721 | 0.13011 | 0.88928 | 0.04088 |
| 0.53542 | 0.12074 | 0.33392 | 0.03100 | 0.38193 | 0.13271 | 0.91966 | 0.03387 |
| 0.50578 | 0.12419 | 0.38160 | 0.03816 | 0.34777 | 0.13447 | 0.94573 | 0.02624 |
| 0.47863 | 0.12718 | 0.43006 | 0.04455 | 0.31488 | 0.13526 | 0.96693 | 0.01822 |
| 0.44641 | 0.13039 | 0.47940 | 0.05004 | 0.28347 | 0.13505 | 0.98255 | 0.01060 |
| 0.41610 | 0.13304 | 0.52654 | 0.05432 | 0.25370 | 0.13346 | 0.99268 | 0.00468 |
| 0.38752 | 0.13509 | 0.57684 | 0.05747 | 0.22541 | 0.13037 | 0.99825 | 0.00115 |
| 0.35962 | 0.13665 | 0.63172 | 0.05939 | 0.19846 | 0.12594 | 1.00000 | 0.00000 |
| 0.32854 | 0.13771 | 0.67649 | 0.05980 | 0.17286 | 0.12026 | | |

| | | | | | | |
|---------|---------|---------|----------|---------|----------|--|
| 0.29648 | 0.13794 | 0.71559 | 0.05921 | 0.14863 | 0.11355 | |
| 0.26356 | 0.13679 | 0.73675 | 0.05844 | 0.12591 | 0.10598 | |
| 0.23263 | 0.13393 | 0.76333 | 0.05703 | 0.10482 | 0.09770 | |
| 0.21283 | 0.13114 | 0.78942 | 0.05506 | 0.08545 | 0.08879 | |
| 0.19561 | 0.12802 | 0.80947 | 0.05310 | 0.06789 | 0.07940 | |
| 0.17473 | 0.12336 | 0.83028 | 0.05062 | 0.05223 | 0.06965 | |
| 0.15733 | 0.11868 | 0.86994 | 0.04446 | 0.03855 | 0.05968 | |
| 0.14032 | 0.11348 | 0.89924 | 0.03838 | 0.02694 | 0.04966 | |
| 0.12497 | 0.10819 | 0.92149 | 0.03274 | 0.01755 | 0.03961 | |
| 0.11009 | 0.10247 | 0.94479 | 0.02561 | 0.01028 | 0.02954 | |
| 0.09550 | 0.09613 | 0.95707 | 0.02117 | 0.00495 | 0.01969 | |
| 0.08018 | 0.08863 | 0.97177 | 0.01493 | 0.00155 | 0.01033 | |
| 0.06800 | 0.08199 | 0.98900 | 0.00570 | 0.00005 | 0.00178 | |
| 0.04897 | 0.07000 | 0.99231 | 0.00363 | 0.00044 | -0.00561 | |
| 0.03568 | 0.05999 | 0.99800 | -0.00013 | 0.00264 | -0.01120 | |
| 0.02846 | 0.05369 | 1.00000 | -0.00178 | 0.00789 | -0.01427 | |